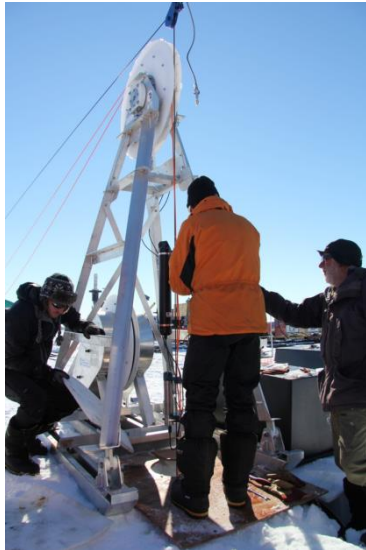


IUP Bremen Research Highlights 2017/2018



Institute of Environmental Physics (IUP)
Institute of Remote Sensing (IFE)
University of Bremen
Otto-Hahn-Allee 1, 28359 Bremen, Germany



Table of Contents

INTRODUCTION	4
REMOTE SENSING OF THE EARTH SYSTEM (PROF. DR. JUSTUS NOTHOLT)	7
GROUND-BASED REMOTE SENSING OF GREENHOUSE GASES USING THE SUN AND THE MOON AS LIGHT SOURCES	7
METHANE MEASUREMENTS IN THE AMAZONIAN RAIN FOREST	8
ATMOSPHERIC MEASUREMENTS DURING THE POLARSTERN CRUISE 2017	9
MEASUREMENTS OF MESOSPHERIC CO IN THE ARCTIC	10
IMPROVING SEA ICE CONCENTRATION RETRIEVAL FROM MICROWAVE SATELLITE OBSERVATIONS	11
SEA ICE THICKNESS RETRIEVAL USING MICROWAVE SATELLITE OBSERVATIONS	14
SNOW DEPTH ON ARCTIC SEA ICE	16
SEA-ICE LEADS AREA FRACTION FROM SENTINEL-1 SYNTHETIC APERTURE RADAR (SAR) IMAGES	18
PHYSICS AND CHEMISTRY OF THE ATMOSPHERE (PROF. DR. JOHN P. BURROWS)	20
SYNERGISTIC EXPLOITATION OF HYPER-AND MULTISPECTRAL SATELLITE DATA FOR QUANTITATIVE ESTIMATES OF DIFFERENT MARINE PHYTOPLANKTON TYPES	20
CARBON DIOXIDE AND METHANE FROM SATELLITES	22
FIRST HIGH RESOLUTION BrO COLUMN RETRIEVALS FROM TROPOMI	24
LONG-TERM CHANGES IN STRATOSPHERIC OZONE FROM SATELLITE OBSERVATIONS	26
SOLAR VARIABILITY	29
TROPOSPHERIC OZONE TRENDS	31
ANALYSIS OF STRATOSPHERIC WATER VAPOUR AND METHANE PROFILES FROM SCIAMACHY SOLAR OCCULTATION	33
TOP-OF-ATMOSPHERE STUDIES OVER A CHANGING ARCTIC	35
RETRIEVAL OF CLOUD OPTICAL PROPERTIES IN PRESENCE OF INCREASED AEROSOLS LOADING	36
COVARIATIONS OF AEROSOL PROPERTIES AND CLOUD BOTTOM ALTITUDE FROM MULTI-SENSOR SPACEBORNE MEASUREMENTS	37
GREENHOUSE GAS OBSERVATIONS FROM AIRCRAFT: METHANE AIRBORNE MAPPER (MAMAP)	38
AIRBORNE OBSERVATIONS IN SELECTED OUTFLOWS FROM EUROPEAN AND ASIAN MEGACITIES	40
IMAGING DOAS NO ₂ MEASUREMENTS DURING THE AQABA SHIP CAMPAIGN	42
MOLECULAR SPECTROSCOPY LABORATORY	43
LABORATORY FOR MODELING AND OBSERVATION OF THE EARTH SYSTEM (PROF. DR. MIHALIS VREKOUSSIS)	45
OUTFLOW OF FORMALDEHYDE AND GLYOXAL FROM THE AFRICAN CONTINENT TO THE ATLANTIC OCEAN	45
MODELING METHANE EMISSIONS FROM COAL MINES AT HIGH RESOLUTION	47
AIR QUALITY SIMULATION OVER THE NETHERLANDS AT HIGH SPATIAL RESOLUTION	48
CONTRIBUTION OF BIOMASS BURNING TO THE ATMOSPHERIC COMPOSITION OF THE REMOTE PACIFIC AS REGISTERED IN EASTER ISLAND	49
TRANSPORT CLIMATOLOGY OF BLACK CARBON EMISSIONS FROM EUROPEAN MEGACITIES	51
CLIMATE MODELLING (PROF. DR. VERONIKA EYRING)	52

INTRODUCTION TO NEW IUP DEPARTMENT ON CLIMATE MODELLING	52
OCEANOGRAPHY (PROF. DR. MONIKA RHEIN)	55
HOW WELL IS THE NORTH ATLANTIC CIRCULATION SIMULATED IN MODELS?	55
WHERE IS THE GREENLAND MELT WATER?	56
INTERNAL WAVES GENERATED BY REMOTE TROPICAL CYCLONES	57
BASAL MELT AND FREEZING RATES FROM FIRST NOBLE GAS SAMPLES BENEATH AN ICE SHELF.....	59
TEMPERATURE FLUX CARRIED BY INDIVIDUAL EDDIES ACROSS 47°N IN THE ATLANTIC OCEAN.....	61
TERRESTRIAL ENVIRONMENTAL PHYSICS (DR. HELMUT FISCHER).....	63
SOURCES AND FATE OF MAN-MADE RADIONUCLIDES IN THE TROPICAL WESTERN PACIFIC OCEAN.....	63
SEARCH FOR THE ORIGIN OF ATMOSPHERIC RADIOACTIVE IODINE IN 2017	65
TEACHING ACTIVITIES	67

Introduction

The IUP comprises six departments: Remote Sensing, Physics and Chemistry of the Atmosphere, Oceanography, Terrestrial Environmental Physics, Modelling and Observation of the Earth System and Climate Modelling.

The **Department of Remote Sensing** employs passive remote sensing instrumentation such as Fourier transform interferometers and microwave radiometers taking measurements in the spectral region from the infrared to the microwave. The instruments are located at various ground based sites ranging from the high Arctic (Svalbard) to the tropics (Suriname), as well as aboard research vessels (R.V. Polarstern) and aircraft. Furthermore, operational satellite instruments are used to monitor atmospheric and earth surface properties. Among them are sea ice coverage, water vapour and clouds. A further research focus is the investigation of stratospheric and mesospheric processes including solar effects on the terrestrial atmosphere. These activities are supported by atmospheric modelling.

The research activities carried out in the **Department of Physics and Chemistry of the Atmosphere** aim at improving the understanding of the complex physical chemical processes in the atmosphere and its interfaces to land, ocean, ice, and deep space. Emphasis is placed on the impact of anthropogenic and natural changes on the composition of the troposphere, stratosphere, and mesosphere, including greenhouse gases, pollutants and reactive gases. A particular focus has been the scientific development and support of satellite sensors to characterise the chemical composition of the atmosphere remotely by means of spectroscopy in the ultraviolet, visible and near-infrared spectral regions using grating spectrometers. The department pioneered this re-

search area with the GOME and SCIAMACHY sensors, as well as with the development of future satellite sensor concepts for geostationary air pollution observations (GeoSCIA, now Sentinel-4) and dedicated greenhouse gas sensors (CarbonSat, potentially becoming a COPERNICUS Sentinel mission). Similar instruments are operated from the ground (NDACC stations, BREDOM network), on ships (R.V. Polarstern), aircrafts and balloons. Remote sensing is complemented by in-situ experiments, laboratory work on spectroscopy and reaction kinetics, as well as modelling of physical and photochemical processes in the lower, middle and upper atmosphere.

The main research topics of the **Department of Oceanography** are the climate relevant processes in the Atlantic Ocean. The global meridional overturning circulation (MOC) plays an important role in the distribution of the heat received from the sun and thus for climate and climate change. Whether and how global warming will affect the circulation and how this will feed back on the climate is one of the central issues of marine research. The department studies – mainly with experimental methods – circulation, formation, and transformation changes in key regions of the Atlantic MOC, develops methods to infer the strength of the MOC, and improves and expands the tracer analysis techniques. Other interdisciplinary research themes are the role of vertical mixing in water mass transformation and at hydrothermal vents, the calculation of upwelling velocities at the equator and at the coast, as well as the dating of groundwa-

IUP Mission Statement

The overarching objective of the Institute of Environmental Physics is to understand the mechanisms controlling the Earth System and its response to change. This is achieved by using physical methods and research focuses on the sub systems atmosphere, ocean, cryosphere, and their interfaces. This requires the development and use of remote sensing techniques from the ground, from ships, aircraft and satellite platforms and in-situ measurements for process studies. The data are coupled with models to interpret the observations and improve the prediction of change.

ter. The research is part of national and international programmes such as CLIVAR (Climate Variability and Predictability) and CARBOOCEAN (EU Integrated Project).

The **Department of Terrestrial Environmental Physics** investigates transport processes in porous systems and soils and conducts research in the fields of radioecology and sediment chronology. It takes advantage of the excellent equipment available in the Bremen State Radioactivity Measurements Lab (which forms part of the state and federal nuclear emergency management networks) and of a unique Earth Field NMR apparatus.

Since 2016, the newly established **Department of Inverse Modelling of the Earth System** led by Prof. Vrekoussis hosts the joint IUP-MARUM working group called LAMOS (Laboratory for Modelling and Observation of the Earth System). LAMOS aims at improving our understanding of the complex mechanisms controlling the emission, transport, transformation and deposition of atmospheric pollutants with the use of state-of-the-art numerical models and novel instrumentation. Special focus is given on the quantification of sources and sinks of long-lived and short-lived species using satellite observations as proxies.

In July 2017, a new IUP department on **Climate Modelling** was established under the lead of Prof. Veronika Eyring. In collaboration with the department on *Earth System Model Evaluation and Analysis* of the German Aerospace Centre's Institute of Atmospheric Physics (DLR-IPA), the new department focuses on analysing Earth system model (ESM) simulations in combination with observations to better understand and project the climate system and anthropogenic climate change. The department provides major contributions to the Coupled Model Intercomparison Project (CMIP), currently in its 6th phase (CMIP6), by contributing to the

development of the Earth System Model Evaluation Tool (ESMValTool) and by running the tool on model output submitted to the CMIP archive.

The IUP is internationally well known for its initiation and participation in a number of advanced space-borne missions, in particular GOME and SCIAMACHY. Both sensors were proposed by the IUP, and the IUP acts as Principal Investigator. The Global Ozone Monitoring Experiment, GOME, which was the first satellite sensor to measure tropospheric trace constituents from space and has operated aboard ERS-2 for over 10 years. GOME is a smaller version of SCIAMACHY, which was launched successfully in 2002 and also has provided almost a decade of successful data. The GOME and SCIAMACHY data records are now continued by GOME-2, OMI, and Sentinel-5P/TROPOMI, as well as in the future by Sentinel-4 and Sentinel-5. IUP scientists are contributing actively to all those missions. The IUP is also involved in many international projects with space-borne instruments for remotely measuring greenhouse gases and surface parameter, such as sea ice, the Wadden Sea and land use. In addition, the IUP runs instrumentation at research measurement stations worldwide. It has participated in many national and international research campaigns using ships, aircrafts and ground-based instruments. Members of the IUP are actively involved in international scientific organisations like COSPAR, IGBP-IGAC, WCRP-SPARC, CACGP and WMO-IGACO.

The complexity of the environmental system on Earth requires a coordinated approach of various scientific disciplines. Based on successful collaborations in the past, the initiative **Advancing Earth Observation Science (AEOS)** has been established in 2017 to assess the relevant physical, chemical, and biological processes by joining the expertise of different partners from the University of Bremen and

worldwide. Special focus is placed on investigations to quantify the impact of human activity on the Earth system and to separate it from natural effects.

More than 100 Ph.D. students and postdocs work at the IUP. Students in general physics have the option to specialize in environmental physics. A variety of courses, conducted in cooperation with colleagues from the Alfred-Wegener-Institute Helmholtz Centre for Polar and Maritime Research (AWI) in Bremerhaven is offered at the IUP. The aim of the environmental physics course is to provide a basic education in the areas of the ocean, the atmosphere and the solid Earth. Whereas other German universities cover parts of environmental physics, for example physical oceanography or meteorology, as independent subjects, Bremen addresses all of them within the physics course fully integrated into the general physics. The students even have the opportunity to participate in exciting expeditions worldwide. To strengthen environmental physics as a course of study in its own right and also to motivate students from abroad to study in Bremen, a four-semester international course leading to a Master of Science (M.Sc.) in Environmental Physics and a two-semester postgraduate course for the Certificate in Environmental Physics have been offered since autumn 2000. The IUP educational activities were further developed towards space applications with the new international and application oriented Masters Programme **Space Sciences and Technologies**. It covers the three basic technologies Remote Sensing, Processing and Communication. The Programme provides theoretical knowledge in the fields of Remote Sensing, Earth Observation, Retrieval Theory, Electronics and Communications a solid hands-on training.

This document provides an overview of selected research highlights achieved by the members of the five IUP departments during the period 2017/2018.

Department contacts



Physics and Chemistry of the Atmosphere
Prof. Dr. John P. Burrows FRS
+49-421-218 62100
burrows@iup.physik.uni-bremen.de



Remote Sensing
Prof. Dr. Justus Notholt
+49-421-218 62190
jnotholt@iup.physik.uni-bremen.de



Oceanography
Prof. Dr. Monika Rhein
+49-421 218 62160
mrhein@physik.uni-bremen.de



Terrestrial Environmental Physics
Dr. Helmut Fischer
+49-421-218 62761
hfischer@physik.uni-bremen.de



Laboratory for Modelling and Observation
of the Earth System
Prof. Dr. Mihalís Vrekoussis
49 (0)421 218 – 62140
vrekoussis@iup.physik.uni-bremen.de



Climate Modelling
Prof. Dr. Veronika Eyring
+49-421-218-62733
Email: veronika.eyring@uni-bremen.de

Ground-based remote sensing of greenhouse gases using the sun and the moon as light sources

Matthias Buschmann, Thorsten Warneke, Christof Petri and Justus Notholt

Atmospheric greenhouse gases have a strong impact on the surface temperatures on Earth. Anthropogenic activities have resulted in an increase of the atmospheric greenhouse gases carbon dioxide (CO₂) and methane (CH₄) and the consequences of the associated temperature increase are already visible. Each year several gigatons of CO₂ are emitted into the atmosphere by human activities. Fortunately, only about 50% of the emitted CO₂ remains in the atmosphere and thus contributes to global warming. The other 50% are taken up by natural sinks - the terrestrial biosphere and the ocean. Methane (CH₄), the second most important anthropogenic greenhouse gas after CO₂, is emitted from highly variable and not well understood sources such as wetlands, rice fields, landfills, oil- and gas-exploration and ruminants.

atmospheric greenhouse gas budgets are precise measurements of atmospheric CO₂ and CH₄ amounts. The global atmospheric observing system for greenhouse gases consists of in situ measurements as well as ground-based and space-born remote sensing measurements. While high quality in situ measurements are available since 60 years, the technically challenging remote sensing measurements of CO₂ and CH₄ became available only about 15 years ago. In contrast to the in situ measurements, remote sensing measurements measure through the whole atmosphere and satellites provide global coverage.



Figure 1: Lunar absorption measurements in the Arctic at the AWIPEV research base in Ny-Ålesund, Spitzbergen. The solar tracker in the picture directs the lunar light into the building where a Fourier Transform InfraRed (FTIR) spectrometer is used to determine the concentrations of CO₂ and CH₄ in the atmosphere from characteristic absorptions in the lunar light.

In order to reliably predict the future climate of our planet a good understanding of the sources and sinks of CO₂ and CH₄ is mandatory. Unfortunately, there are large gaps in our understanding of the natural sources and sinks of these gases. The basis for understanding the

The current ground based remote-sensing network in the global atmospheric observing system for greenhouse gases consists of about 25 globally distributed sites. The Institute of Environmental Physics at the University of Bremen was the first European group starting these measurements, and 4 sites are currently operated by the University of Bremen. The measurements in the network are performed during daytime only since the sun is used as the light source. We recently developed a technique to also use the moon as the light source, which enables measurements during the night. This is especially important for high latitude sites, where the sun is not visible for several months during the winter. An example of the data derived from these lunar measurements is shown in Figure 2.

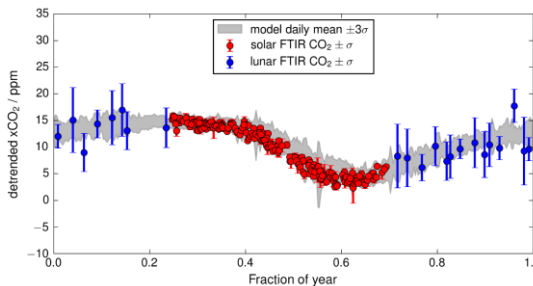


Figure 2: Ground based remote sensing measurements of CO₂ at the AWIPEV research base in Ny-Ålesund, Spitzbergen. The CO₂ data derived from solar absorption measurements are indicated in red and the lunar absorption measurements in blue.

Methane measurements in the Amazonian rain forest

Hella van Asperen, Thorsten Warneke, Justus Notholt

The Amazon basin in South America is largely covered by wetlands and wetlands are the largest source of methane (CH_4) to the atmosphere: it has been estimated that this region is responsible for about one tenth of the annual CH_4 emissions to the atmosphere globally. However, the tropical CH_4 budget is still not well quantified and the Amazon basin's 'top-down' (inverted) emission estimate, which is based on vertical CH_4 concentration profiles, differs by a factor of two

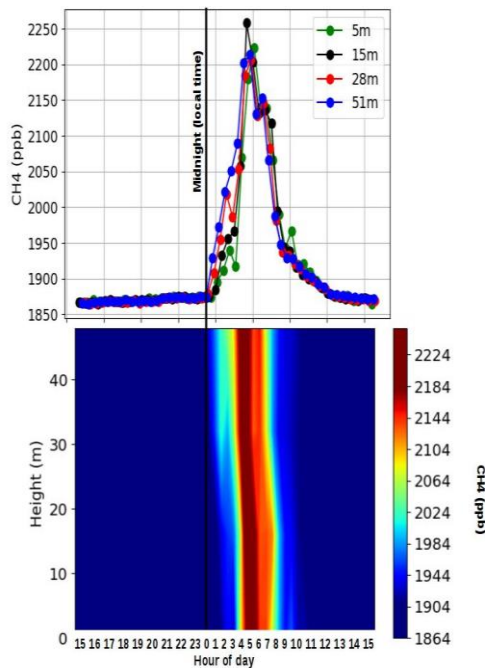


Figure 4: Diel variation of the CH_4 concentration profiles.

from the 'bottom-up' estimate, originating from the upscaling of individual sources. It has been suggested that CH_4 emission sources inside the Amazonian wetlands, such as the (seasonally) flooded forests, are underestimated.

A collaboration between IUP and INPA (the National Institute for Amazonian Research, Manaus, Brazil) was recently founded, which resulted in the successful installation of an in-situ FTIR spectrometer at the ZF2

field site, a long term ecological and (micro) meteorological field station in the middle of the pristine rain-forest. The FTIR-analyser, capable of measuring CH_4 , CO_2 , N_2O , CO and $\delta^{13}\text{CO}_2$ simultaneously, has been set up to measure above canopy fluxes, by use of the Relaxed Eddy Accumulation (REA) technique, as well as to measure concentration profiles within the canopy. CH_4 flux measurements of this spatial scale and duration do currently not exist in the Amazon. Furthermore, individual CH_4 source emissions, such as from forest soil, water surfaces and tree stems, will be measured in the future. The combination of measurements with different spatial scale and focus will allow us to investigate the contribution of the different CH_4 sources in the footprint of the REA measurements.

First results (see Figure 4) show the appearance of high CH_4 concentrations during some nights, which have to be further analysed with regard to wind directions and meteorological conditions.

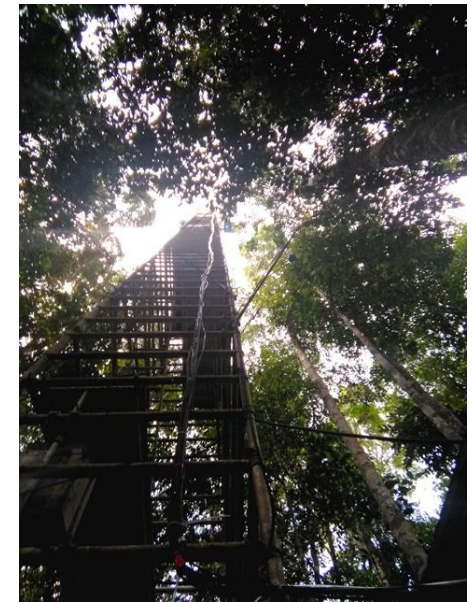


Figure 3: The measurement tower at the ZF2 field site close to Manaus (Brazil).

Atmospheric measurements during the Polarstern cruise 2017

Mathias Palm, Philipp Richter, Matthias Buschmann, Christine Weinzierl und Justus Notholt

During the Polarstern cruises PS 106 (Bremerhaven -> Longyearbyen -> Tromsø) and PS 107 (Tromsø -> Longyearbyen) from May to August 2017, a mobile Fourier Transform instrument setup (IUP004) was deployed to measure atmospheric trace gases in emission and absorption mode. The measurement campaign was part of the DFG Transregio TR172 (Arctic Amplification -- Climate relevant Atmospheric and Surface Processes and Feedback mechanisms (AC3), www.ac3-tr.de). The cruise started in Bremerhaven on the 24th of Mai and ended in Tromsø on the 17th of August 2017. The cruise track in the Arctic is shown in Figure 5.

During PS 106, the AG Notholt was part of the PASCAL campaign, which was an expedition with main focus on atmospheric trace gases, pollution and clouds. During PS106/2 and PS 107 the main focus of the expedition was biological and oceanographic research, but we operated our mobile instrument on the ship. In Figure 6, the mobile facility IUP004 is shown during operation.

Figure 7 shows an example of emission measurements during clear

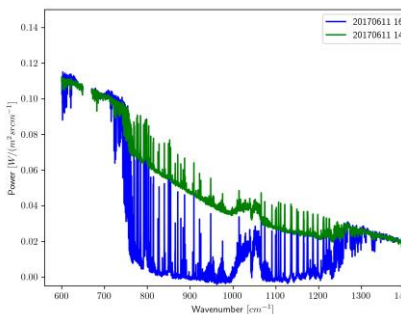


Figure 7: Atmospheric spectra emitted from the atmosphere during clear sky (blue) and a thin cloud (green).



Figure 6: The IUP004 container on the Polarstern in operation.

sky conditions (blue) and in the presence of a thin cloud (green). Thin cloud means, the cloud is partly transparent, but the cloud itself adds a radiative offset. The height of the offset and its structure can be used to measure certain cloud parameters, i.e. the cloud liquid water and ice content as well as the mean radius of the liquid and solid particles contained in the cloud. The derived results for 11th of June 2017 are shown in Figure 8. These parameters determine the radiative properties of the cloud and influence the micro-climate below the cloud.

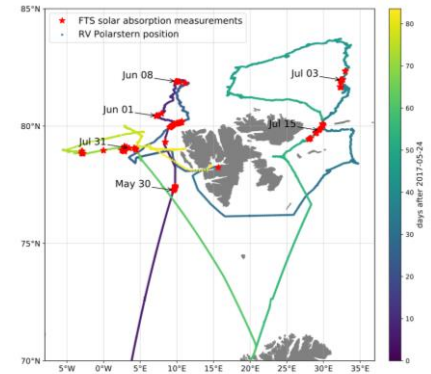


Figure 5: Cruise track of the Polarstern cruises PS 106 and PS 107. Emission measurements were performed continuously whenever conditions allowed.

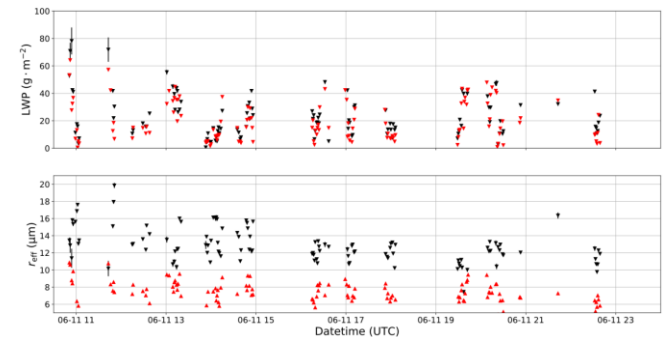


Figure 8: Liquid water (LWP) and the effective radius of the droplets as retrieved from FTIR (black) and measured by cloudnet (red) on the 11th of June 2017.

Measurements of mesospheric CO in the Arctic

Mathias Palm, Justus Notholt

In 2017 a new instrument measuring CO started to operate in the Arctic at the AWIPEV research base in Ny-Ålesund, Spitzbergen. It is a complimentary instrument to an instrument in Kiruna, Sweden.

Measurements of mesospheric CO have been used in the past to obtain descent rates of air in Polar winter (Allen, 1981, de Zafra, 2004). In order to do so, the profile of CO is monitored. Because it is produced in the thermosphere and swiftly depleted in sunlit conditions in the mesosphere and stratosphere, it was assumed that the decent of the profile (Figure 10) can be used to calculate the descent of air. Ryan (2018) investigated this claim and found that other processes, chemistry and transport are non-negligible (Figure 9). Therefore, the interpretation of such measurements is more complicated than though before. Ryan (2018) suggested to use the term

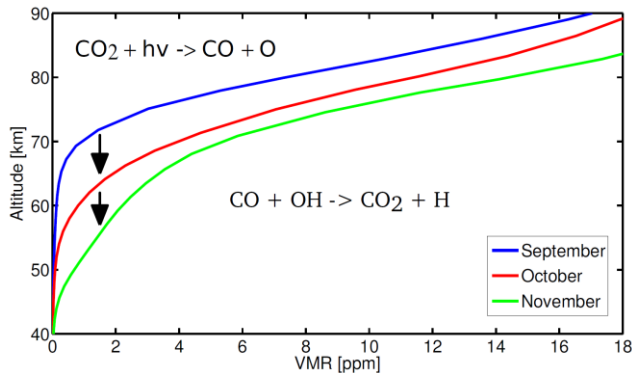


Figure 10: Sinking of the CO profile over the winter pole.

"effective descent" of the trace gas instead, including all effects which lead to a change in the VMR (volume mixing ratio) in a given time.

References

Allen, M.; Yung, Y., Waters, J. Vertical Transport and Photochemistry in the Terrestrial Mesosphere and Lower Thermosphere (50-120 KM), *J. Geophys. Res.*, 86, 3617 – 3627, 1981

de Zafra, R. L., Muscari, G.: CO as an important high-altitude tracer of dynamics in the polar stratosphere and mesosphere, *J. Geophys. Res.*, 109, D06105, 2004.

Ryan, N. J., Kinnison, D. E., Garcia, R. R., Hoffmann, C. G., Palm, M., Raffalski, U. and Notholt, J.: Assessing the ability to derive rates of polar middle-atmospheric descent using trace gas measurements from remote sensors *Atmos. Chem. Phys.*, 18(3), 1457-1474, 2018.

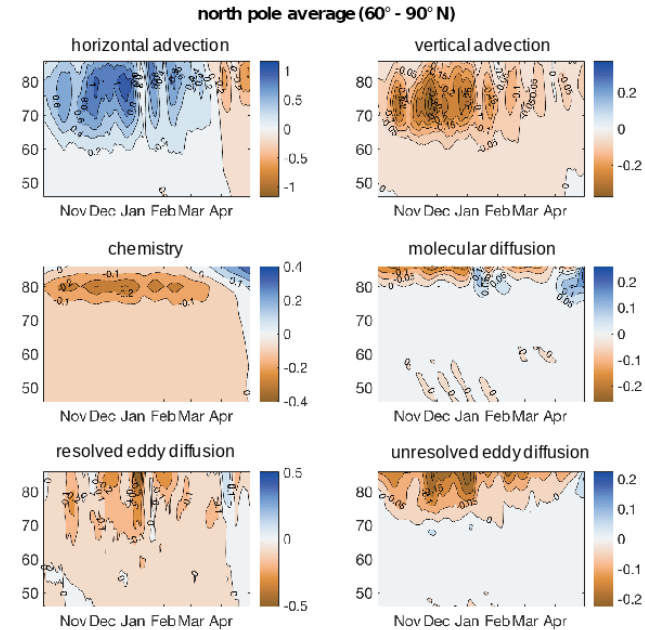


Figure 9: Contribution of different mechanisms to the variation of the CO profiles in ppmv/day

Improving sea ice concentration retrieval from microwave satellite observations

Junshen Lu, Georg Heygster, Gunnar Spreen

Sea ice is an important component of the global climate system and indicator of its recent changes. It affects the heat balance, ocean circulation and salt transfer through various mechanisms. Due to the high albedo of sea ice compared to water, the reduction of the sea ice cover during summer reduces the albedo and increases the heat input to the ocean, which in turn reduces the sea ice cover even further and thus exhibits a positive feedback loop. The melt of sea ice can increase ocean stratification while the production of sea ice and the according brine release increases mixing. These processes are linked to the deep water formation, e.g., in the Greenland Sea and Weddell Sea. An accurate knowledge of the spatial and temporal distribution of sea ice is thus essential to understand and predict weather and climate. Passive microwave satellite observations have been widely used to deliver such information, because they are independent of the light condition, and are relatively insensitive to clouds and weather influences.

A number of empirical algorithms have been developed to retrieve sea ice concentration from satellite microwave brightness temperatures, thanks to the distinct radiometric signatures of ice and open ocean. Many of these algorithms, such as NASA Team and Bootstrap, are based on measurements at 19, 23 and 37 GHz, which restricts the spatial resolution of the retrieval to the coarse spatial resolution of these frequency channels (approximately 25 km). Since the launch of the AMSR series satellites in 2002, brightness temperatures

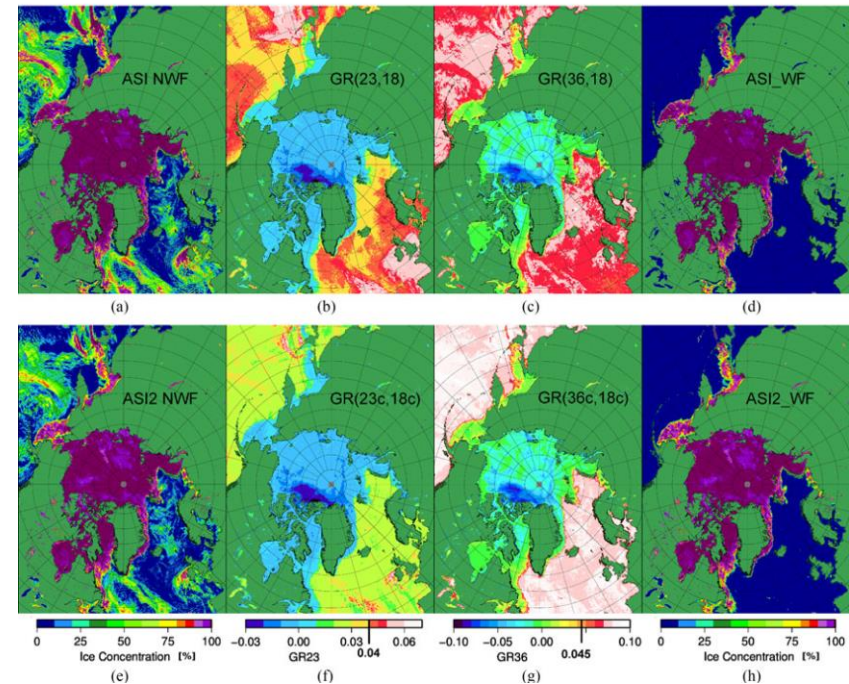


Figure 11: Ice concentration retrievals of ASI and ASI2 and weather filters from Mar. 15, 2008. The top row is based on the original AMSR-E TBs (ASI), the bottom row is based on the atmospherically corrected TBs (ASI2). From left to right column: Sea ice concentration without any weather filter, gradient ratio GR(23, 18), gradient ratio GR(36, 18), and sea ice concentration with weather filters GR(23, 18) and GR(36, 18) applied. The thresholds for the weather filters are marked on the color bars. ASI2 GR(36,18) threshold is 0.07.

are observed at 89 GHz with a much improved spatial resolution of about 5 km. The ARTIST sea ice (ASI) algorithm utilizes the polarization difference of brightness temperatures at 89 GHz and thus provides global daily sea ice concentration at unprecedented spatial resolution (Spreen et al., 2008). Granted by the improved resolution, the ASI ice concentration can reveal fine structures of ice and more detailed ice conditions near the ice edge. However, brightness temperatures at 89 GHz are more prone to weather contamination compared

to the lower frequencies. Influences from the atmospheric water absorption/emission and wind roughened ocean surface scattering in general increase the ASI retrieved ice concentration, and often lead to erroneous ice detection over open ocean (Figure 11a). A common approach is to apply threshold based weather filters that eliminate erroneous ice concentration on a statistical basis (Figure 11d). The disadvantage of this approach is evident in the marginal ice zone, where either weather induced spurious ice is left uncorrected, or sea ice is falsely removed (Figure 12a). Another approach is to correct the atmospheric influences on the observed brightness temperatures explicitly. This method requires knowledge of the atmospheric condition, and a radiative forward model.

The improved sea ice concentration retrieval algorithm named ASI2 developed at the University of Bremen uses atmospheric corrected AMSR-E brightness temperatures at 89 GHz (Lu et al., 2018). The correction is carried out by simulating changes in brightness temperatures caused by weather contaminations using a microwave emission forward model of the atmosphere. New tie points are derived based on the corrected brightness temperatures. Wind speed, total water vapour, liquid water path and surface temperature are dominant geophysical quantities that cause weather contamination. In theory, influences from all mentioned parameters can be corrected if the exact atmospheric condition of the satellite overflight is known. However, observation data is sparse in the Polar Regions. Numerical weather prediction data on the other hand has a better coverage and is reliable for most of the parameters except for liquid water path which is connected to clouds and thus highly variant in space and time. We therefore use ERA-Interim forecast data for the correction scheme of ASI2, and exclude liquid water path to avoid introducing uncertainty from the atmospheric data.

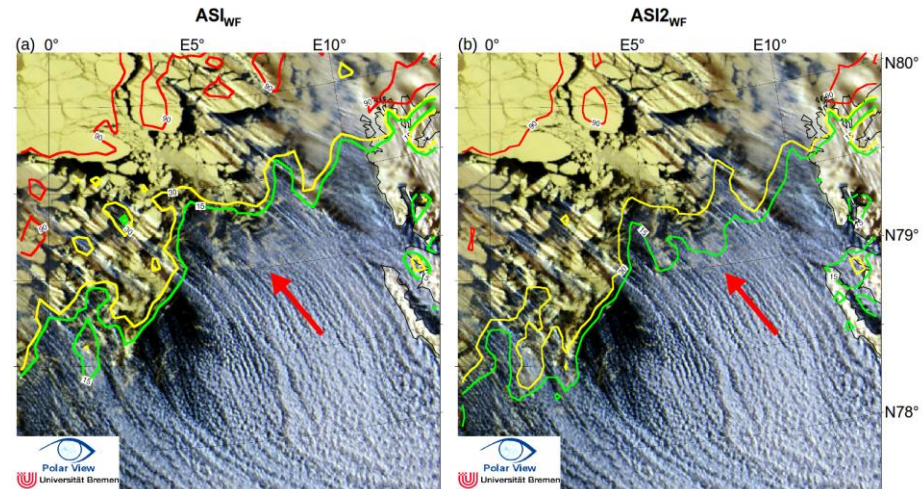


Figure 12: Ice concentration retrieved by ASI (left) and ASI2 (right) overlaid on MODIS image of Fram Strait from Apr. 22, 2008. Sea ice areas appear yellow or brown, clouds are white or gray, and open water appears dark blue/black. SIC of 15%, 30%, and 90% are marked by green, yellow, and red isolines, respectively. The actual ice edge is denoted by the red arrows. Ice concentration of 15% is a common threshold to determine ice edge. The ASI2 detected ice edge (green contour on the right) is much closer to the actual ice edge than the ASI one.

With the atmospheric correction, typical radiometric signatures of water and ice can be better distinguished. The ASI2 ice concentration is much improved in regions of low ice concentration and the ice edge is represented more accurately (Figure 12b). Also “weather patterns”, i.e. false fluctuations of the ice concentration, over the ice pack are less pronounced on the ASI2 daily ice concentration maps than ASI. Spurious ice is significantly reduced, but not completely eliminated due to influences from the uncorrected liquid water path (Figure 11e). A relaxed weather filter sensitive to liquid water path, the gradient ratio (GR) of the corrected 36V and 18V brightness temperatures (Figure 11g), is applied to clear the remaining spurious ice. The improved weather filter better outlines

ice edge and compromises much less low ice concentration compared to the weather filters used by ASI. Comparison of ASI2 daily ice extent/area from 2008 to a number of ice concentration algorithms confirms that ASI2 outperforms ASI in regions of low ice concentration, and agrees better with other algorithms (Figure 13). The remaining challenge of the ASI2 algorithm is the uncompensated influences of liquid clouds. This can in principal be improved with better liquid water path data retrieved at the exact satellite foot print. Such a data set is now available (Scarlat et al., 2017), and a variation of the ASI2 algorithm including liquid cloud correction is under development.

References:

Lu, J., Heygster, G., and Spreen, G.: Atmospheric Correction of Sea Ice Concentration Retrieval for 89 GHz AMSR-E Observations, IEEE Journal of Selected Topics in Applied Earth Observations and Remote Sensing, vol. 11, no. 5, pp. 1442-1457. doi: 10.1109/JSTARS.2018.2805193, 2018.

Scarlat, F., Heygster, G., and Pedersen, L.T.: Experiences with an Optimal estimation algorithm for surface and atmospheric parameter retrieval from passive microwave data in the arctic, IEEE Journal of Selected Topics in Applied Earth Observations and Remote Sensing, vol. 10, no. 9, pp. 3934-3947, 2017.

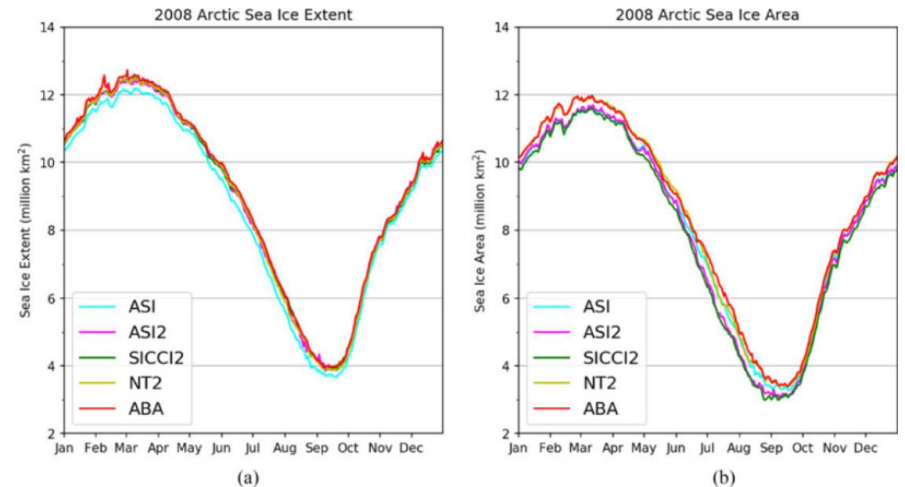


Figure 13: Ice extent, i.e. the area covered by sea ice of at least 15% concentration (a) and ice area (b) in the Arctic for the year 2008 retrieved from AMSR-E data by five different algo-

Spreen, G., Kaleschke, L. and Heygster, G.: Sea ice remote sensing using AMSR-E 89-GHz channels, Journal of Geophysical Research – Oceans, vol. 113, C02S03. doi: 10.1029/2005JC003384, 2008.

Sea ice thickness retrieval using microwave satellite observations

Cătălin Pașilea, Georg Heygster, Marcus Huntemann, and Gunnar Spreen

Sea Ice plays a central role in the Earth's climate system and thus, knowledge about its properties and extent is important for climate modelling and prediction as well as for planning shipping routes in the polar regions. The thickness of sea ice determines the heat exchange between the ocean and the atmosphere as well as the resistance against the deforming forces of wind and ocean currents. Already a thin layer of sea ice provides a surface for snow to deposit. Snow accumulation even further reduces the heat exchange and increases the albedo. The amount of thicker multiyear ice has been strongly decreasing during the last decades, but the winter sea ice maximum only little. Thus, today the area of thinner first-year ice makes up a considerably larger part of the sea ice covered region. Daily observations of the ice cover and its thickness are important to track these rapid changes and improve our understanding of the Arctic climate system.

One way of measuring sea ice thickness is using passive microwave satellite observations. More specifically, in the L-band (1.4 GHz) part of the electromagnetic sea ice emissions do not come only from the surface, but also from deeper layers underneath. For ice thinner than about 50 cm, therefore, a relation of emitted radiation to ice thickness can be exploited. Another advantage of L-band radiometry is that the atmosphere (clouds, precipitation, etc.) has small influence on the surface emission when traveling through the atmosphere towards the sensor and, as at all microwave frequencies, observations at L-band can be used during the long polar night when no light is available. With the launch

of the new Soil Moisture Active Passive (SMAP) L-band radiometer in 2015, a previously developed retrieval algorithm for thin sea ice thickness (Huntemann et al., 2014) which uses data from the Soil Moisture Ocean Salinity (SMOS) sensor has been adapted to use brightness temperature (TB) data from the new sensor (Patilea et al., 2017). Figure 14 represents an example of one day of data from both sensors used for ice thickness retrieval. At that time of year, sea ice freeze-up has started and large parts of the marginal seas (e.g. Laptev and Kara Seas) of the Arctic Ocean are covered with thin sea ice. We can also observe that in some regions like the Laptev Sea, the sea ice along the shores already got thicker than 50 cm while in the central Laptev Sea still areas of thin sea ice prevail. There is an area around the North Pole, where there is no usable satellite data available. That area, however, is covered by thicker sea ice almost year-round. Thus, the complete L-band data time series allows monitoring the development of thin ice areas in the Arctic Ocean since the start of SMOS in 2010. Figure 15 shows an example of a time series of L-band retrieved data in the Laptev Sea. The start of each year is taken as 15th of September which is approx-

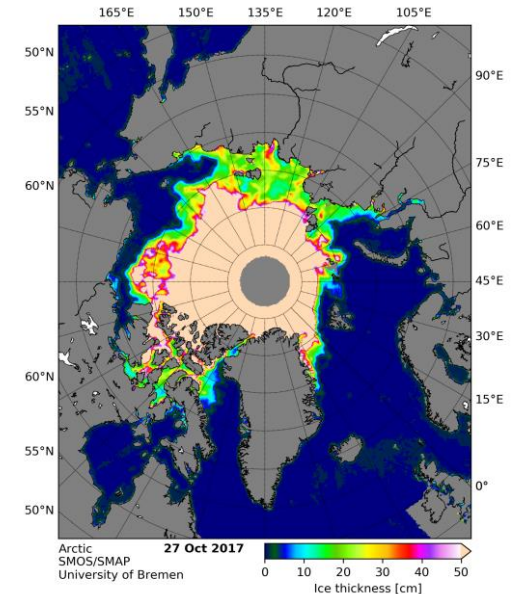


Figure 14: Map of sea ice thickness from the 27th of October 2017 retrieved using SMOS and SMAP data over the Arctic. Ice thicknesses up to 50 cm can be retrieved and are shown here.

imately around the Arctic sea ice minimum. We can see that by 15th to 20th of October most of the Laptev Sea is covered in sea ice (Figure 15 middle plot) by that time also the mean ice thickness increases and reaches the maximum ice thickness of 50 cm that can be retrieved only about one month later by 15 November (Figure 15 bottom plot). In the top plot we can also observe that there is variability between the years, with 2011 having a late freeze-up and containing dominantly thin sea ice until the start of December, while in 2016, thick sea ice becomes dominant approximately three weeks earlier.

A method to quantify the uncertainty of the new data set has been developed based on the sensitivity of the retrieval to changes in brightness temperature and is shown in Figure 16. The uncertainty increases with ice thickness. For ice thickness of about 50 cm the average uncertainty reaches 30 cm due to high sensitivity to the change in brightness temperatures combined with uncertainty of the sea ice concentration that will impact it. Thus, here we only present ice thickness up to 50 cm. The sea ice concentration's impact at higher uncertainties is due to brightness temperature saturation over 50 cm. An ice thickness much higher than 50 cm com-

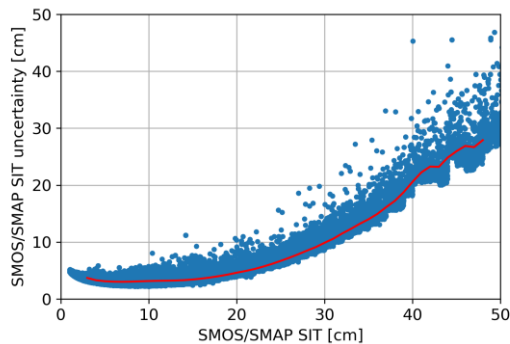


Figure 16: Sea ice thickness (x axis) versus uncertainty (y axis) using SMOS and SMAP data for the 27th of October 2017 (see map in Figure 14); the red curve represents the mean.

pared with only slightly lower than 100% sea ice concentration can decrease the

retrieved sea ice thicknesses below 50 cm. Since this sea ice thickness data set represents a daily thickness at low thicknesses and temperatures, the physical variability of thickness within one day is much higher compared to higher thickness which increases the uncertainty for thinner sea ice.

References

- Huntemann, M., Heygster, G., Kaleschke, L., Krumpen, T., Mäkynen, M., and Drusch, M.: Empirical sea ice thickness retrieval during the freeze-up period from SMOS high incident angle observations, *The Cryosphere*, 8, 439-451, <https://doi.org/10.5194/tc-8-439-2014>, 2014.
- Pațilea, C., Heygster, G., Huntemann, M., and Spreen, G.: Combined SMAP/SMOS Thin Sea Ice Thickness Retrieval, *The Cryosphere Discuss.*, <https://doi.org/10.5194/tc-2017-168>, in review, 2017.

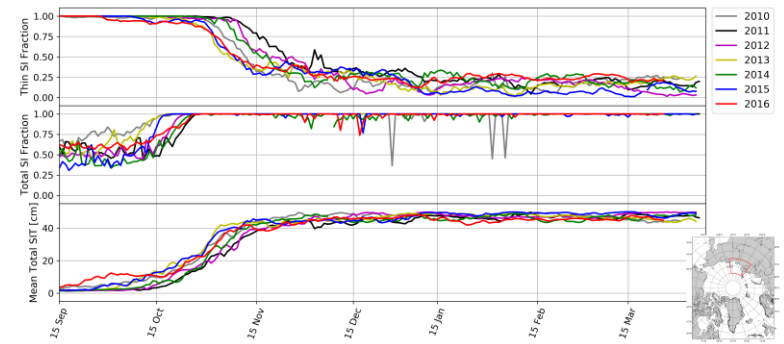


Figure 15: Time series of sea ice thickness (SIT) in the Laptev Sea (see red outline in lower-right map) from 15 September to 31 March for each of the seven years 2010 to 2016. The top plot shows the fraction of the complete Laptev Sea area covered by thin sea ice, i.e., sea ice below 51 cm. The middle plot shows the fraction of the Laptev Sea area covered by sea ice independent of its thickness, i.e., the ice concentration. The mean sea ice thickness for the Laptev Sea is shown in the (bottom) plot. Note the maximum ice thickness retrieved is 50 cm and for dates when that thickness is reached the actual mean thickness is likely to be higher.

Snow depth on Arctic sea ice

Philip Rostosky, Georg Heygster, Christian Melsheimer, Gunnar Spreen

Snow on Arctic sea ice plays an important role in the Arctic climate system. It reflects the majority of the incoming solar radiation and insulates the sea ice from warm air in summer and therefore slows down its melting. In addition, information about snow depth is needed for sea ice thickness retrievals based on satellite altimetry.

However, the vast area and the extreme weather conditions make it difficult to monitor the snow during Arctic winter. In situ measurements of snow depth on sea ice are rare and mostly obtained in spring because they require daylight conditions. Drifting buoys may cover a whole winter season

but their measurements are only representative for a small area around the buoy. Satellites provide the only tool to observe the whole Arctic on a daily basis.

Here we present a new snow depth retrieval based on passive microwave satellite observations (Rostosky et al., 2018).

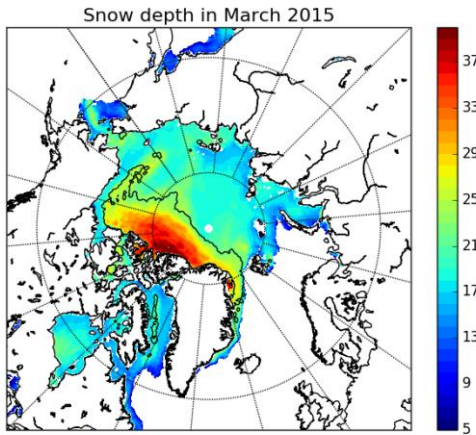


Figure 18: Monthly averaged snow depth for March 2015. The black contour line is the monthly averaged border between multiyear ice and first-year ice.

Passive microwave satellites are independent of sunlight and clouds and provide daily, Arctic-wide observations, with, however, coarse spatial resolution (e.g. 25 km²). The retrieval of snow depth from microwave radiometer observations is based on the different scattering properties of snow grains at different microwave frequencies. Methods to derive snow depth from microwave radiometers are already known since the 1990s. The new retrieval developed here, however, uses a different set of microwave frequencies (6.9 GHz and 18.7 GHz) and is extended to Arctic multiyear ice (ice that has survived at least on summer melt) while previous retrievals only work over first-year ice (ice that has formed since the beginning of the freezing season). The method uses an empirical linear relation between the gradient ratio GR(v1,v2) of satellite observed brightness temperatures at two different frequencies (v1 and v2) and snow depth ($GR(v1,v2) = (tbv1 - tbv2) / (tbv1 + tbv2)$). The retrieval has the form $Sd = a + b * GR(v1,v2)$, where Sd is the snow depth and a and b are empirical regression coefficients.

In order to derive the regression coefficients, satellite observations are compared to airborne snow depth measurements (obtained in each spring from 2009 to 2016) from the NASA Operation IceBridge campaign (OIB). Figure 17 shows the scatter plot of the satellite observations (GR(19/7)) and

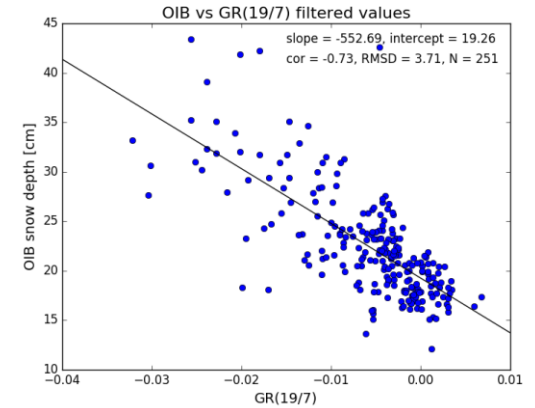


Figure 17: Scatter plot between OIB snow depth and GR(19/7) over first year ice. In addition, the regression line (black line) and the regression coefficients, the correlation (cor) and the RMSD and number of points (N) are shown

OIB snow depth over Arctic first-year ice. We find good correspondence between the satellite and airborne datasets. The correlation (cor) between both datasets is -0.73 and the root mean square error (RMSD) is 3.71 cm. Over Arctic multiyear ice, we find a reasonable relation (not shown here) but with higher errors (RMSD = 6.63 cm). Figure 18 shows the monthly averaged snow depth in March 2015 derived with the new retrieval. The black contour marks the border between multiyear ice and first-year ice. The deepest snow is retrieved north of the Canadian Archipelago and is between 35 cm and 45 cm deep. In the central Arctic, the snow depth is around 20 cm. The lowest values are found in the Kara and Laptev Seas where the snow depth is between 10 cm and 15 cm. The current retrieval is only evaluated for spring snow since the OIB snow depth measurements are limited to March and April. In spring we find a very good performance of the retrieval over first-year ice and a reasonable performance over multiyear ice. For first-year ice regions we can look into the temporal development of the snow depth. Figure 19 shows the snow depth time series from 2005 to 2016 for the Beaufort Sea. We find significant variability in snow depth for all winter months. For example, winter 2014/2015 starts with a high snow depth of more than 25 cm already in October which increases to 32 cm in January. Thereafter it strongly decreases again while in most other years the snow depth increases more monotonously from October to April.

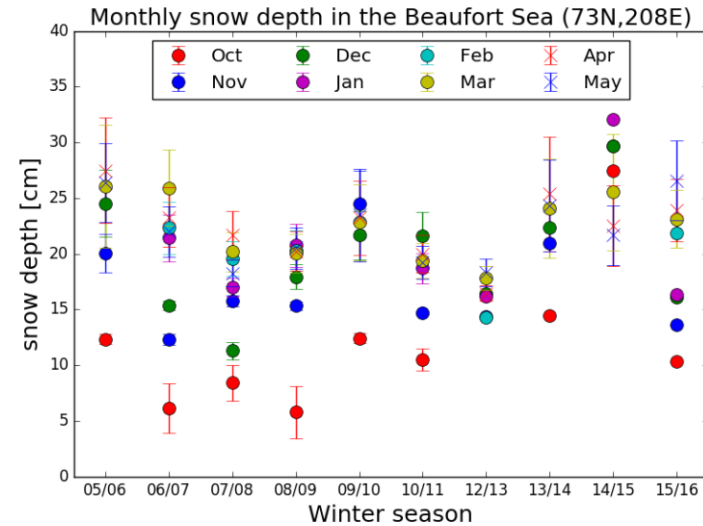


Figure 19: Monthly averaged snow depth in the Beaufort Sea from winter 2005/2006 to winter 2015/2016.

References:

Rostosky, P., Spreen, G., Farrell, S.L., Frost, T., Heygster, G., and Melsheimer, C.: Snow Depth Retrieval on Arctic Sea Ice From Passive Microwave Radiometers – Improvements and Extensions to Multiyear Ice Using Lower Frequencies, *Journal of Geophysical Research: Oceans*, 123, doi.org/10.1029/2018JC014028 x, 2018

Sea-ice leads area fraction from Sentinel-1 Synthetic Aperture Radar (SAR) images

Dmitrii Murashkin, Gunnar Spreen, Marcus Huntemann

Sea ice covers a significant part of the Arctic Ocean. In winter it works as an insulator between the relatively warm ocean and the cold atmosphere. One of the important features of the ice cover is the presence of sea-ice leads. Leads are larger cracks in the sea ice covered by open water or thin ice surrounded by a thicker sea ice. They form in the process of ice fracturing due to shear and divergence stresses in the sea ice cover. These stresses are often forced by ocean currents, tides, and by winds in the atmosphere. Leads regulate the heat, gas and moisture fluxes between the ocean and the atmosphere. Intense heat exchange at the water-air boundary during winter leads to an increased sea ice production in areas of open water. Therefore, spatial and temporal distributions of leads are of interest for climate studies. Also leads are areas of increased biological activity in the Arctic Ocean (phytoplankton

blooms). Life of Arctic animals (e.g. walruses, polar bears, birds) is often tied to leads. And finally, leads are important for shipping as vessels can travel much faster and fuel-economic through leads than through the surrounding sea ice.

Field measurements in the Arctic are hard and expensive to perform. Remote-sensing methods provide measurements covering large areas in the Arctic. Synthetic Aperture Radar (SAR) sensors are able to provide high resolution data (~50 m) with good spatial (~400 km for a single scene) and temporal coverage. The Copernicus Sentinel-1 mission currently comprises two satellites with a SAR as primary instrument. In the Extra Wide swath mode, SAR images are acquired at both HH and HV polarizations. In this mode, the backscatter of the electromagnetic wave transmitted at 5.4 GHz frequency at horizontal polarization is received and decomposed

into horizontal (HH) and vertical (HV) polarization components. Sentinel-1 SAR provides images with 40 meters pixel size over oceans including areas covered with sea ice.

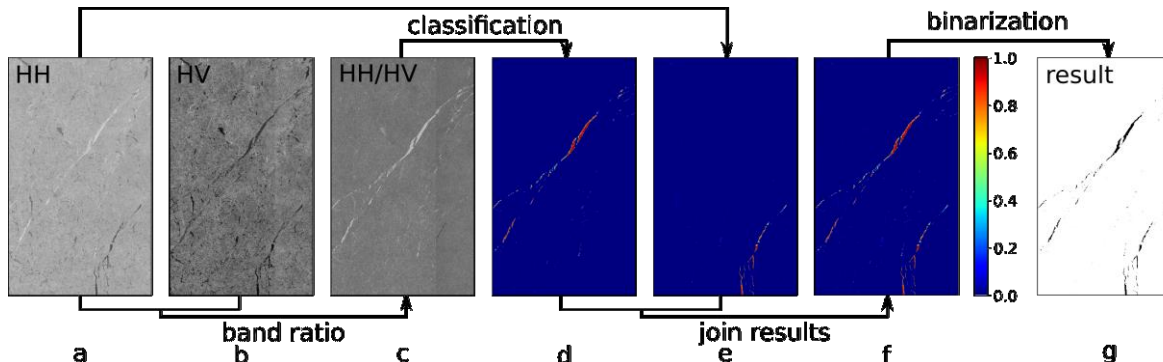


Figure 20: Lead detection algorithm. (a) and (b) are the original SAR data (3 Feb 2016, 22:29, Canadian Arctic; size of the area shown is about 150km by 80km), HH and HV respectively. (c) is the band ratio HH/HV. (d) and (e) are probabilistic classification results of (a) and (c). (f) is the sum of (d) and (e). (g) is the binary classification derived from (f) by applying a threshold of 50%.

We analyse dual-band images taken by Sentinel-1 to map sea ice leads. The HH band is used for detection of leads that have a smooth surface, i.e., open water without significant swell and thin sea ice formed under calm conditions. In case of a wind-roughened ocean surface, backscatter in the HH band shows strong dependence on incidence angle. This might affect sea ice – water discrimination. Therefore the band ratio (HH / HV) is used in addition to HH backscatter values. Backscatter values are extended with several textural features for both the HH band and the band ratio. These in total 25 features are used in a supervised classification employing a random forest classifier to distinguish the leads from sea ice (Murashkin et al, 2018). The trained classifier is then applied to all Sentinel-1 images acquired during one day. An illustration for the classification process is shown in Figure 20. The HH band and the band ratio are classified independently. Results of the two classifications are probabilities for each pixel to be a lead. Both results are summed up and then a threshold of 50% is applied to produce the final binary lead map.

Finally, scenes produced within one day are combined into a binary lead map of the Arctic with a spatial resolution of 80 meters. A sea ice mask based on 15% sea ice concentration from the AMSR2 passive microwave satellite radiometer is applied (Sprenn et al., 2008). To obtain statistical information of the distribution of leads and to visualize the leads in the Fram Strait region we calculate the lead area fraction on a 800 meters grid (shown in Figure 21a). The Fram Strait is the major route for sea ice exported from the central Arctic. Due to high deformation rates in the region, many leads are formed as it can be seen in Figure 21a.

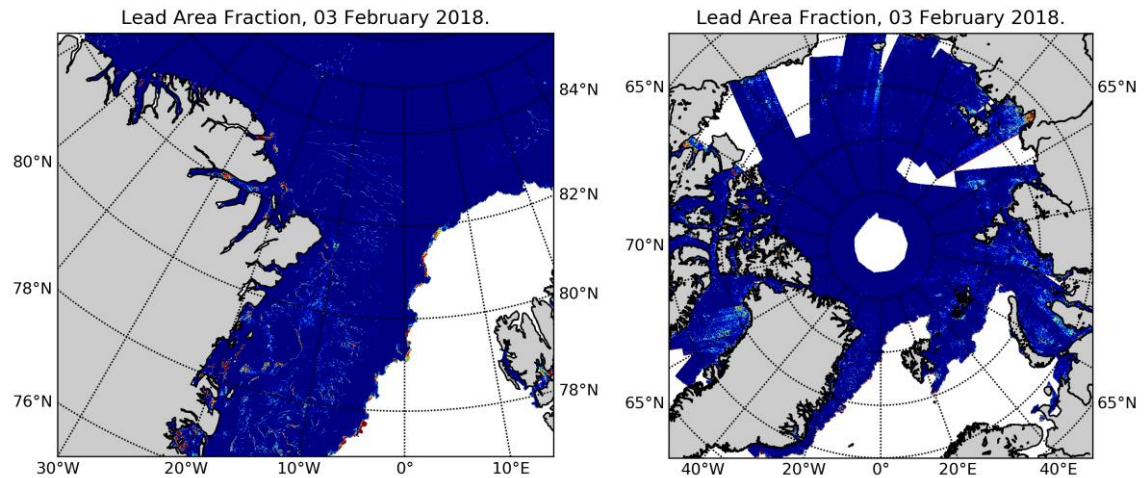


Figure 21: Lead Area Fraction in the Fram Strait region (left) and the Arctic Ocean (right), both on February 3, 2018

Arctic-wide lead area fraction on a 4 km grid is presented in Figure 21b. Higher lead area fraction values are observed in the areas of thin sea ice (Kara Sea, Laptev Sea, Baffin Bay), in the areas of high sea ice deformation rates (Fram Strait), and along the sea ice edge (white areas are either not covered by sea ice or by SAR data).

Maps of leads with 80 meter resolution provide the opportunity to analyse the distribution of leads and their temporal evolution. A better understanding of lead variability can lead to a better representation of them in climate and regional forecast models. Which in turn can help to, e.g., understand the biological activity in the Arctic better and provide additional information for navigation in Polar Regions.

References

Murashkin, D., Sprenn, G., Huntemann M., & Dierking, W.: Method for detection of leads from Sentinel-1 SAR images. *Ann. Glaciol.*, 59(76pt2), 124–136. doi:10.1017/aog.2018.6, 2018.

Sprenn, G., Kaleschke, L. & Heygster, G.: Sea ice remote sensing using AMSR-E 89-GHz channels. *J. Geophys. Res.*, 113. doi:10.1029/2005JC003384, 2008.

Synergistic exploitation of hyper- and multispectral satellite data for quantitative estimates of different marine phytoplankton types

Svetlana Losa, Mariana Soppa, Tilman Dinter, Aleksandra Wolanin, Robert Brewin, Annick Bricaud, Julia Oelker, Ilka Peeken, Bernard Gentili, Vladimir Rozanov and Astrid Bracher

To assess the feedback of climate change on the marine system, information on the distribution of major phytoplankton functional types (PFTs) is essential since they take different roles in the global marine ecosystem and biogeochemical cycles. The phytoplankton diversity retrievals conducted over the last years were based on applying various algorithms mostly to multispectral satellite data. The relatively high spatial and temporal resolution of the multispectral ocean colour data make them attractive for exploiting in phytoplankton dynamics and phenology studies. However the ocean colour sensors provide information on water leaving radiance at rather limited number of spectral bands (up to 5) with the band widths varying from 7.5 nm to 20 nm. This spectral resolution is accurate enough to retrieve the concentration of total chlorophyll “a” (Chla, a pigment produced by all phytoplankton species), but products are limited to either only indicating size fractions or the dominance of phytoplankton groups by applying empirical relationships between total Chla (TChla) and *in situ* marker pigments determined using high precision liquid chromatography (HPLC). The empirical nature of these relationships (usually estimated in a global context) leads to limitations of the so-called abundance-

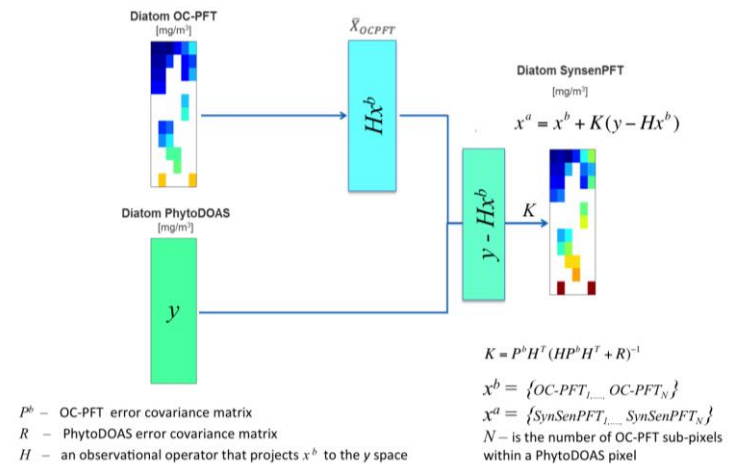


Figure 22: Diagram exemplifying the SynSenPFT algorithm that updates the PFT information from each OC-PFT sub-pixel (x^b) within a PhytoDOAS pixel given the PhytoDOAS Chla (y) and a priori error statistics introduced in the Kalman gain K , which results in SynSenPFT Chla (x^a) at each OC-PFT sub-pixel.

based approaches: they cannot predict atypical associations, the relationships derived may differ regionally.

Former and current satellite instruments with a very high spectral resolution (<1 nm) provide the opportunity for distinguishing more accurately multiple PFTs by relying explicitly on spectral signatures of specific PFT retrieved directly from the input information (spectral approaches). The capability to retrieve quantitatively major PFTs based on their absorption properties has been demonstrated with the Phytoplankton Differential Optical Absorption Spectroscopy (PhytoDOAS) method (developed by the AWI-IUP PHYTOOPTICS group) in the open ocean using hyper-spectral satellite data from the sensor “Scanning Imaging Absorption Spectrometer for Atmospheric CHartography” (SCIAMACHY). However, the global exploitation of hyper-spectral satellite data for ocean colour applications has been very limited, since the pixel size of these data is very large

(30 km by 60 km) and global coverage by these measurements is reached only within six days.

A recent study led by the AWI-IUP PHYTOOPTICS group in collaboration with the Laboratoire d'Océanographie de Villefranche (LOV), Villefranche, France, and the Plymouth Marine Laboratory (PML), Plymouth, United Kingdom, suggests how to overcome the aforementioned shortcomings (see details in Bracher et al. 2017), of current multispectral PFT products (supplying either dominant groups only, or data products with strong linkage to a priori information) and of current PhytoDOAS-data products (low temporal and spatial coverage). The authors developed the SynSenPFT algorithm (Figure 22) by the synergistic use of low spatial resolution hyperspectral data with higher spatial and temporal resolution multispectral satellite data: They improved/revised the existing PFT algorithms PhytoDOAS (based on hyperspectral data, current version at <https://doi.pangaea.de/10.1594/PANGAEA.870486>) and OC-PFT (based on multispectral data, current version in supplement of Losa et al. 2017), and, by combining those retrieved products via optimal interpolation, derived PFT products with temporal and spatial resolution as high as multispectral ocean colour data but using the spectral information from the hyper-spectral data. The algorithm principles, sensitivity studies and its thorough validation against a large global in-situ phytoplankton group data set (<https://doi.org/10.1594/PANGAEA.875879>) have been published in Losa et al. (2017).

The SynSenPFT data product provided as chlorophyll "a" concentrations of three major phytoplankton groups, namely diatoms, coccolithophores and prokaryotic phytoplankton (also called cyanobacteria) at a 4km x 4km resolution grid covering the global ocean on a daily basis

over the entire ENIVSAT mission time is publicly available at

<https://doi.pangaea.de/10.1594/PANGAEA.875873>. Figure 23 shows the SynSenPFT products for the global ocean in September 2006. The SynSenPFT algorithm can later be applied to hyperspectral sensors such as Sentinel-5-Precursor, Sentinel-4 and Sentinel-5 in combination with the multispectral sensor OLCI on Sentinel-3 to ensure a further improved spatial resolution of the retrieved PFT Chla product and the prolongation of the time series over the next decades.

References

Bracher, A., Bouman, H., Brewin, R., Bricaud, A., Brotas, V., Ciotti, A., et al.: Obtaining phytoplankton diversity from ocean color: A scientific roadmap for future development. *Frontiers in Marine Science* 4, 55. doi:10.3389/fmars.2017.00055, 2017.

Losa, S. N., Soppa, M. A., Dinter, T., Wolanin, A., Brewin, R. J. W., Bricaud A., Oelker, J., Peeken, I., Gentili, B., Rozanov, V., Bracher, A.: Synergistic exploitation of hyper- and multispectral precursor Sentinel measurements to determine Phytoplankton Functional Types at high spatial and temporal resolution (SynSenPFT), *Frontiers in Marine Science*, 4, 203, doi: 10.3389/fmars.2017.00203, 2017.

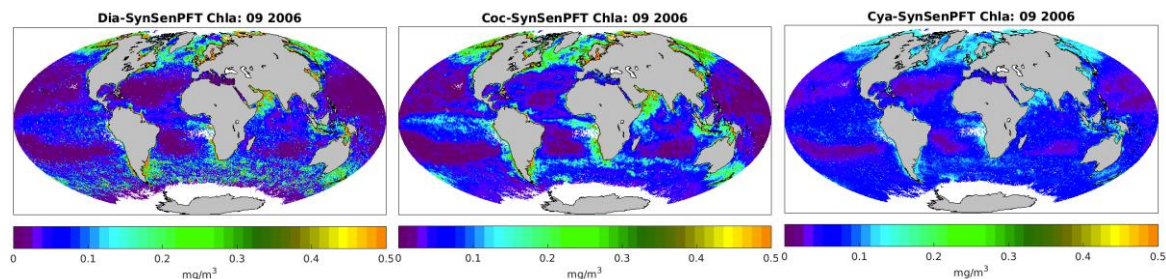


Figure 23: Monthly mean SynSenPFT Chla product of diatoms (Dia), coccolithophores (Coc) and cyanobacteria (Cya) for September 2006.

Carbon dioxide and methane from satellites

Michael Buchwitz, Maximilian Reuter, Oliver Schneising, Stefan Noël, Jens Heymann, Vladimir Rozanov, Heinrich Bovensmann, and John P. Burrows

Carbon dioxide (CO₂) and methane (CH₄) are the two most important anthropogenic (“man-made”) greenhouse gases (GHG) contributing to global warming. Carbon monoxide (CO) is an important air pollutant affecting human health. Despite their importance, our understanding of their variable atmospheric concentrations and related natural and anthropogenic sources and sinks has significant gaps. We derive information about these gases from radiance spectra measured by satellites, generate and deliver corresponding scientific and operational atmospheric concentration data products (“vertical columns”) of these gases and use these measurements to improve our knowledge about these important atmospheric constituents.

Of particular relevance are satellite observations with high measurement sensitivity to CO₂, CH₄ and/or CO concentration changes close to the Earth’s surface, where the source/sink signals are largest. Currently, we are using primarily the following satellite instruments: SCIAMACHY on ENVISAT (2002-2012), TANSO-FTS/GOSAT (since 2009), OCO-2 (since 2014) and Sentinel-5-Precursor (S5P, since 2017). In addition, we are working on the specification of new satellites, in particular for better CO₂ observations in the future.

For example, we used satellite data to obtain information on the CO₂ emissions of the Indonesian fires in 2017. To address this, we used data from NASA’s OCO-2 satellite in combination with inverse modelling schemes to quantify the CO₂ emissions from Indonesian biomass burning. The key results are shown in

Estimated CO₂ emission for the 2015 Indonesian fires (July - November)

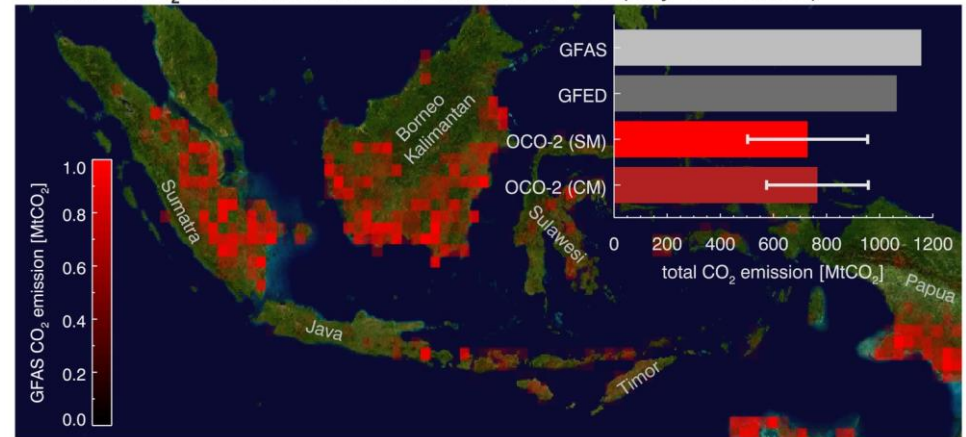


Figure 24: Estimated CO₂ emissions from the 2015 Indonesian fires as obtained from OCO-2 satellite data using 2 different methods (red bars) compared to independent emission data bases (grey bars) (from: Heymann et al., 2017).

Figure 24. As can be seen, the estimated emissions are nearly 750 Megatons of CO₂ (MtCO₂) in the time period between July and November 2015.

In October 2017 the Sentinel-5-Precursor (S5P) satellite has been successfully launched. At IUP the retrieval algorithm WFM-DOAS (or WFMD), which has been initially developed for SCIAMACHY/ENVISAT, has been adjusted and optimized for the retrieval of methane (CH₄) and carbon monoxide (CO) vertical columns. First results are shown in Figure 25. The new S5P CO data show much more detail in terms of spatial and temporal resolution compared to SCIAMACHY on ENVISAT. The IUP CO data product obtained from S5P has been compared with ground-based data and good agreement has been found. It is planned to use the atmospheric CO concentration data product to obtain information on the emissions of localized CO Sources (“CO hotspots”) in the future.

TROPOMI/WFMD CO Nov-Dec 2017

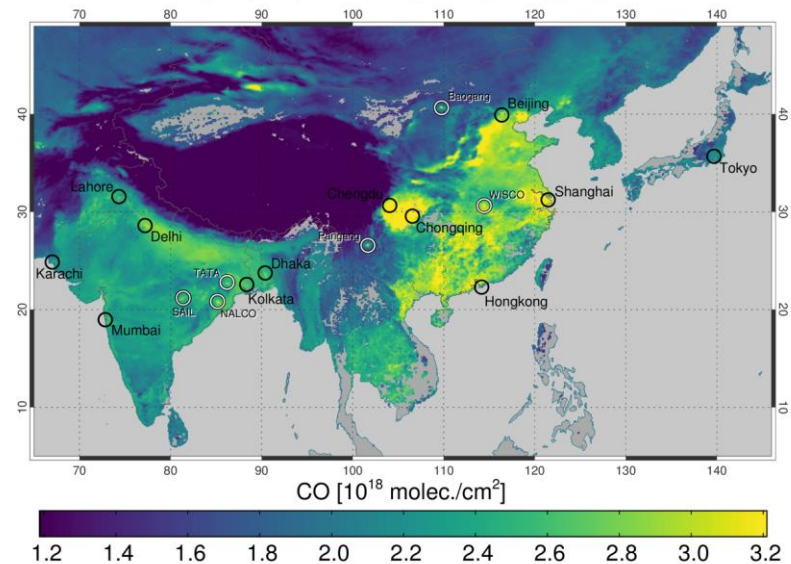


Figure 25: First CO vertical column results from the Sentinel-5-Precursor (SSP) satellite as retrieved using University of Bremen's WFMD algorithm. Clearly visible are enhanced CO concentrations over highly populated areas and areas with significant industrial activity (Figure: O. Schneising, IUP).

The IUP of the University of Bremen is also strongly involved in the specification of improved future satellites in particular for anthropogenic CO₂ monitoring. In this context the IUP is providing expertise to the European Space Agency (ESA) and the European Commission (EC) for the planned Copernicus candidate CO₂ monitoring (CO2M) mission and IUP member Dr. M. Buchwitz has been selected to be a member of the ESA/EU CO2M Mission Advisory Group (MAG). The CO2M mission evolves from the IUP lead CarbonSat initiative.

References

Buchwitz, M., Schneising, O., Reuter, M., Heymann, J., Krautwurst, S., Bovensmann, H., Burrows, J. P., Boesch, H., Parker, R. J., Somkuti, P., Detmers, R. G., Hasekamp, O. P., Aben, I., Butz, A., Frankenberg, C., Turner, A. J.: Satellite-derived methane hotspot emission estimates using a fast data-driven method, *Amos. Chem. Phys.*, 17, 5751-5774, doi:10.5194/acp-17-5751-2017, 2017.

Heymann, J., M. Reuter, M. Buchwitz, O. Schneising, H. Bovensmann, J. P. Burrows, S. Massart, J. W. Kaiser, D. Crisp: CO₂ emission of Indonesian fires in 2015 estimated from satellite-derived atmospheric CO₂ concentrations, *Geophys. Res. Lett.*, DOI: 10.1002/2016GL072042, pp. 18, 2017.

Reuter, M., M. Buchwitz, M. Hilker, J. Heymann, H. Bovensmann, J. Burrows, S. Houweling, Y. Liu, R. Nassar, F. Chevallier, P. Ciais, J. Marshall, and M. Reichstein: How much CO₂ is taken up by the European terrestrial biosphere? *Bull. Amer. Meteor. Soc.* doi:10.1175/BAMS-D-15-00310.1, 24 April 2017, 665-671, 2017.

Reuter, M., M. Buchwitz, O. Schneising, S. Noel, H. Bovensmann, J. P. Burrows: A Fast Atmospheric Trace Gas Retrieval for Hyperspectral Instruments Approximating Multiple Scattering - Part 2: Application to XCO₂ Retrievals from OCO-2, *Remote Sens.*, 9, 1102, doi:10.3390/rs9111102, 2017.

Links

IUP Carbon-GHG-Group website: http://www.iup.uni-bremen.de/carbon_ghg/

IUP Image of the Month (<http://www.iup.uni-bremen.de/eng/about/image-of-the-month/index.html>):

- May 2018: Atmospheric CO₂ reaches new high-water mark
- February 2017: CO₂ emissions from Indonesian Fires in 2015

Press releases:

- [25-September-2018: Umweltforscher analysieren mit Satellitendaten die Moorbrand-Abgase \(in German\)](#)
- [Euronews \(14 Dezember 2018\): IUP satellite data show undeminished increase of CO₂ concentrations also in 2018](#)

Interviews:

- Wissenschaft Persönlich: Dr. Michael Buchwitz (<https://www.bremen.de/wissenschaft/wissenschaft-persoendlich/wissenschaft-persoendlich-michael-buchwitz>)

First high resolution BrO column retrievals from TROPOMI

Sora Seo, Andreas Richter, Anne-Marlene Blechschmidt, Ilias Bougoudis and John P. Burrows

In spite of their low atmospheric concentrations, halogens and their oxides play important roles in both the troposphere and the stratosphere. They are highly reactive, can act as efficient catalysts in ozone depletion and in the case of iodine, they are involved in particle formation in particular in remote regions. Stratospheric halogen loading has a large anthropogenic component with CFCs and halons released by human activity contributing significantly to observed levels, and leading to the annual formation of the springtime ozone hole over the Antarctic. In the troposphere, halogens are mostly released from natural sources such as sea salt, volcanic emissions and biogenic activities.

Bromine monoxide (BrO) has structured absorption spectra in the UV part of the spectrum and can therefore be detected by absorption spectroscopy. With the launch of the GOME instrument in 1995, such measurements have become possible from space, and it were GOME observations which for the first time documented the extent and intensity of bromine chemistry over sea ice covered areas in spring in both hemispheres. Since then, BrO retrievals have been applied to data from the follow-up missions SCIAMACHY, OMI, and the GOME-2 series of instruments, successively improving spatial resolution and coverage. In October 2017, the TROPOMI instrument on Sentinel-5 Precursor was successfully launched into an early afternoon orbit, and this instrument also provides the spectral coverage and resolution for BrO retrievals. Compared to its predecessors, TROPOMI has much improved spatial resolution ($3.5 \times 7 \text{ km}^2$ at nadir, to be reduced to $3.5 \times 5.5 \text{ km}^2$ in 2019) with nearly global coverage each day and at a signal to noise ratio which is comparable to that of earlier instruments on a per pixel basis.

In a first demonstration, Seo et al., 2018 have tested the applicability of existing BrO retrievals to measurements of TROPOMI, applied it to a limited set of measurements and compared the results to those obtained by OMI and GOME-2B.

A detailed analysis of the impact of choosing different wavelength regions for the retrieval showed, that the results are very sensitive to this choice, depending on the measurement scenario analysed. At low sun, absorption by ozone can interfere with the BrO retrieval, limiting the usable spectral range at shorter wavelengths where ozone absorption becomes large. At larger wavelengths, spectral interference by Raman scattering in the atmosphere (Ring effect) becomes a problem, in particular at high sun and in the presence of clouds. As the absorption cross-sections of BrO and formaldehyde (HCHO) are similar for some bands, care must be taken to avoid regions with high correlation between these two absorbers. Based on the analysis of several TROPOMI test cases, a fitting range of 334.6-358 nm was selected as the optimal wavelength range for TROPOMI BrO retrievals for most of the possible measurement situations.

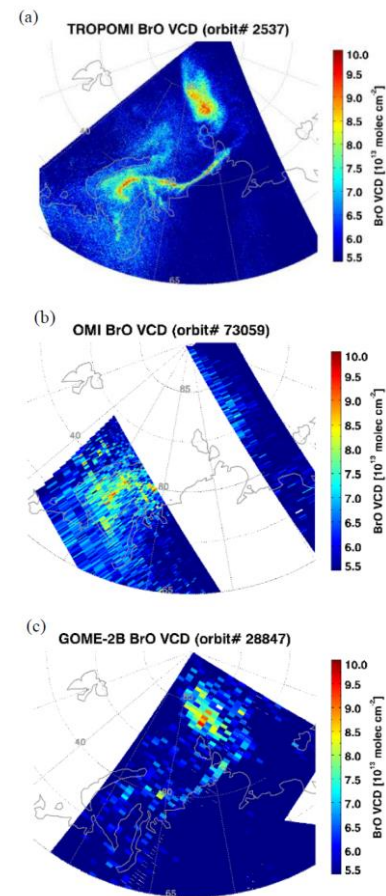


Figure 26: Comparison of BrO observations over part of the Arctic on April 10, 2018 from TROPOMI (top), OMI (middle) and GOME-2B (bottom). While TROPOMI and OMI are in early afternoon orbits having similar overpass times, GOME-2B is in an early morning orbit.

With these settings, a consistent BrO retrieval could be performed on TROPOMI spectra, and one example is shown in Figure 26 for parts of a single orbit over the Arctic. For comparison, also the simultaneous measurements from OMI and GOME-2B are shown. Two regions of enhanced BrO can be distinguished, one narrow band extending from Nowaja Semlja along the coast, and a second, larger region further North on the Kara Sea. The same pattern can be seen in the GOME-2B data, albeit with much less detail and slightly displaced as the observational time was not identical. OMI measurements only show part of the BrO enhancement as spatial coverage of the instrument is reduced because of the so called row anomaly. This example demonstrates the level of detail that is provided by TROPOMI BrO retrievals and that the signal to noise of these data is excellent. What the origin for the narrow BrO plume is, and whether its peculiar shape is the result of local meteorology or of bromine release along the coast will be the subject of further analysis.

Another well-known BrO source is the Rann of Kutch salt marsh. GOME-2 and OMI data have been used to investigate the spatial and temporal variation of BrO levels in this region based on monthly and seasonal averages in Hörmann et al., 2013. Here, it is shown that TROPOMI data has sufficient spatial resolution and signal to noise ratio to provide images of the distribution of BrO on a daily basis (Figure 27). Comparison with matching OMI data shows that the enhancement is also present in OMI retrievals, due to the higher noise it is however difficult to identify and interpret. With the enhanced resolution of TROPOMI, it will be possible to study the spatial distribution of BrO over the marsh in much more detail, enabling separation of the effects of transport and local emissions.

In addition to the case studies shown here, also a longer time series of BrO columns from the three instruments TROPOMI, OMI, and GOME-2B is compared in Seo et al., 2018, showing

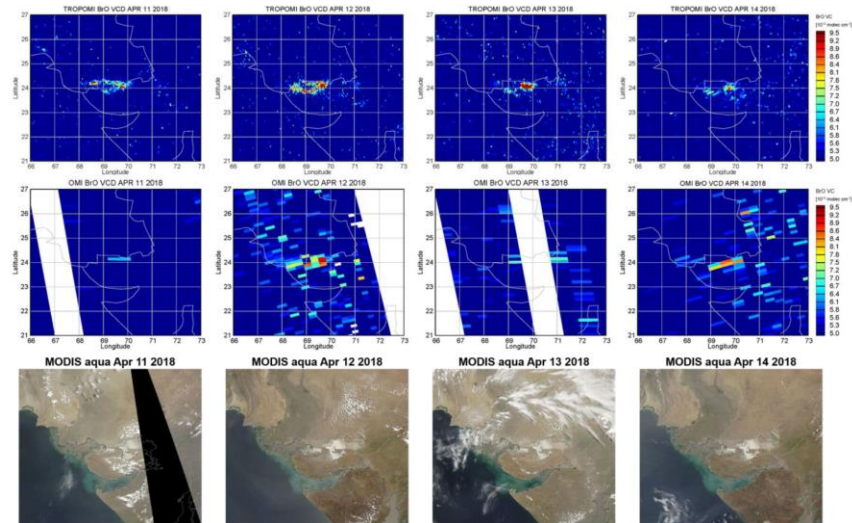


Figure 27: Daily BrO geometric vertical columns [10^{13} molec cm^{-2}] over the Rann of Kutch salt marsh on 11, 12, 13, and 14 April 2018 from TROPOMI (top) and OMI (middle) measurements as well as MODIS Aqua true colour images over the study region for the same days (bottom).

good but not perfect consistency between the results of the sensors. Future studies will have to improve on the treatment of light path (geometric assumptions were used here) and investigate the reasons for remaining differences between the data sets. The main focus however will be on the atmospheric interpretation of this unique new data set of atmospheric BrO columns.

References:

- Seo, S., Richter, A., Blechschmidt, A.-M., Bougoudis, I., and Burrows, J. P.: First high resolution BrO column retrievals from TROPOMI, Atmos. Meas. Tech. Discuss., <https://doi.org/10.5194/amt-2018-365>, in review, 2018.
- Hörmann, C., Sihler, H., Beirle, S., de Vries, M. J. M., Platt, U. and Wagner, T.: Seasonal variation of tropospheric bromine monoxide over the Rann of Kutch salt marsh seen from space, Atmos. Chem. Phys. Discuss., 2016, 1–32, doi:10.5194/acp-2016-90, 2016.

Long-term changes in stratospheric ozone from satellite observations

Carlo Arosio, Alexei Rozanov, Mark Weber, Evgenia Galytska, Elizaveta Malinina and John P. Burrows

Absorbing the UV radiation from the sun, ozone plays a crucial role in the Earth's stratosphere, which extends from about 15 to 50 km above the surface. Thereby it acts as a protective shield for living organisms at the Earth surface and heats the stratosphere, driving dynamic processes. Total ozone is an important factor that determines how much of the harmful UV radiation reaches the surface. In order to disentangle dynamical and chemical processes in the atmosphere, the vertical distribution of ozone (profiles) have to be measured. Since ozone depleting substances (ODS), which were phased out under the Montreal Protocol agreement in 1986, are declining in the stratosphere, it is expected that ozone will slowly recover. First signs of ozone recovery were indeed identified in the upper stratosphere. Spaceborne observations are highly important for stratospheric studies as they are capable of providing long-term data sets with a global coverage allowing us to study the temporal evolution of the atmospheric composition. Continued observations of ozone with satellites are paramount to monitor the success of the Montreal Protocol and to study the interaction between ozone and changing climate. The Institute of Environmental Physics (IUP) of the University of Bremen was actively involved in the preparation of the WMO/UNEP Scientific Assessment on Stratospheric Depletion 2018.

Long-term changes in ozone profiles

Satellite instruments measuring in limb-viewing geometry observe the atmosphere tangentially to the Earth's surface and, thus, provide a capability to derive vertically resolved information

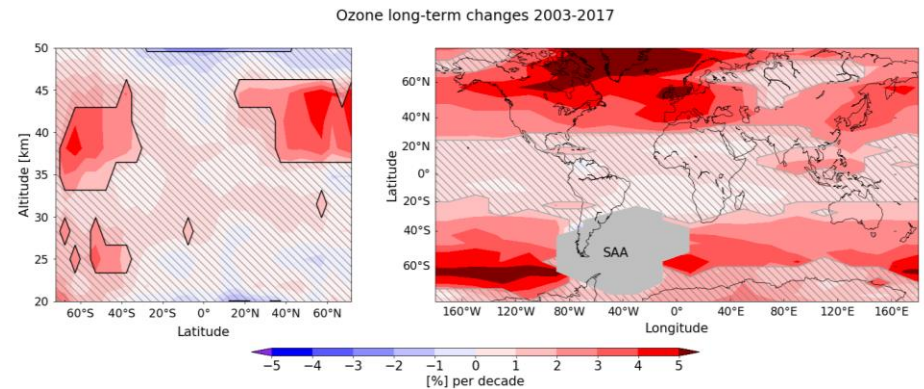


Figure 28: Ozone long-term changes over the 2003-2017 period in % per decade. Left panel: zonally averaged values as a function of the altitude and latitude. Right panel: longitudinally resolved linear changes of ozone at the altitude of 42 km. Hatched areas indicate non-significant trends. Grey area marks the South Atlantic Anomaly (SAA), where the detectors of the instruments might be affected by the high energy particles flux.

on atmospheric species. In this study, measurements in the UV and visible spectral ranges from two limb-viewing instruments, SCIAMACHY/Envisat and OMPS-LP/Suomi-NPP, were used. The former instrument operated from August 2002 to April 2012 and the latter one has been performing observations since the beginning of 2012. As time series obtained from single sensors are generally too short to obtain reliable estimations of the long-term changes in the stratospheric ozone, a lot of effort has been put by the scientific community into merging of data sets from different space-borne instruments.

Ozone profiles from SCIAMACHY and OMPS-LP satellite instruments have been retrieved at IUP Bremen using similar approaches in order to ensure the best consistency between both data sets. The description of the retrieved time series and their validation using independent observations from space-borne and ground-based instruments are presented by Jia et al. (2015) and Arosio et al. (2018). The time series from the two instruments have been merged together to analyse stratospheric ozone changes over the past 15 years. Since the overlap period between the two missions is very short, a so-called transfer function, i.e., a

reliable independent data set which has sufficient overlaps with each of the data sets, was used to remove possible offsets between SCIAMACHY and OMPS-LP. Owing to the high spatial and temporal resolution of the satellite measurements, it was possible to analyse vertically, latitudinally and longitudinally resolved long-term changes in stratospheric ozone considering monthly averaged profiles. Linear ozone changes were computed using a multi-linear regression (MLR) model accounting for the influence of relevant atmospheric processes related to the Quasi-Biennial Oscillation (QBO), solar activity, and El Niño–Southern Oscillation (ENSO).

Figure 28 shows the derived linear changes in stratospheric ozone over the 2003-2017 period in percent per decade. In the left panel, zonally averaged linear changes as a function of altitude are displayed, hatched areas depict statistically non-significant (at 2σ level) values. A prominent feature observed in this plot is a clear increase of ozone concentrations in the mid-latitude upper stratosphere. The ozone linear change values reach 4% per decade especially in the northern hemisphere. The observed positive ozone changes follow the dramatic loss of the stratospheric ozone observed until the end of 90s and are partially attributed to the implementation of the Montreal protocol and its amendments. In the right panel of Figure 28, the longitudinally resolved linear changes of ozone are shown at 42 km altitude, where strongest ozone recovery was identified. As seen from the plot, the longitudinal distribution of the observed ozone changes is highly inhomogeneous with the largest increase observed above Canada and Greenland and almost no changes above Siberia. Possible reasons for this behaviour are currently under investigation.

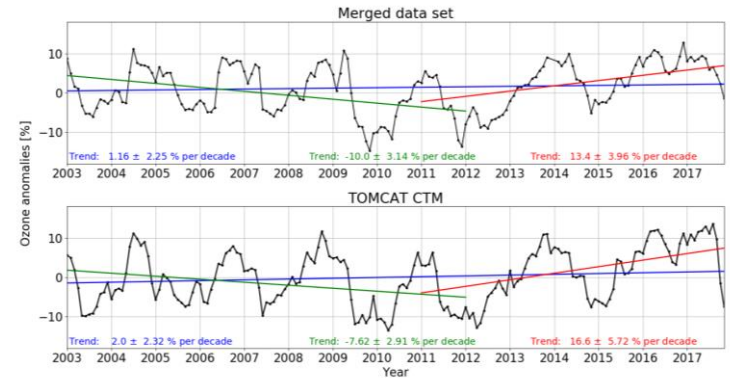


Figure 29: Linear changes of ozone anomalies (after subtracting seasonal means) at 32 km altitude in the tropics. Upper panel: merged SCIAMACHY+OMPS-LP data set. Lower panel: TOMCAT model data.

Total ozone trends

As a contribution to the 2018 WMO/UNEP Scientific Assessment on Stratospheric Ozone Depletion, long-term trends of five merged long-term total ozone data sets were investigated. One of the datasets is our own in-house processed GSG merged dataset that combines satellite total ozone data from GOME, SCIAMACHY, and GOME-2 (1995-present). Full recovery of total ozone to 1980 levels is not expected to occur before the middle of this century, nevertheless some first signs of ozone recovery are evident from long-term ozone observations. The five merged total data records (four based upon satellite data, one upon ground-based observations) show that for most latitudes total ozone has slightly increased (<1%/decade) but the trends derived using multivariate linear regression (MLR) are mostly statistically insignificant (Weber et al., 2018). Looking at the global mean (60°S-60°N), see Figure 30, three out of the five data records (including ours) show statistically significant increases of about +0.5 to +0.7 % per decade since 1997, however, the maximum difference in the trends between any pair of datasets is 0.5%/decade as well.

The trend detection is difficult as ozone in the lower stratosphere (major contribution to the total column ozone) shows large interannual variability in the extra tropics. The interannual variability (solar, QBO, ENSO) is accounted for in the MLR but it contributes to larger uncertainties in the derived linear trends. Total ozone above Antarctica, where the spring ozone hole is regularly occurring, shows some early signs of recovery (Weber et al., 2018, Chipperfield et al. 2017, Steinbrecht et al., 2018). The total ozone time series agree well with chemistry transport-model calculations demonstrating that the current evolution of ozone is consistent and compliant with the Montreal Protocol (Chipperfield et al., 2017, 2018).

Acknowledgements

We thank Prof. Martyn Chipperfield and Dr. Sandip Dhomse (School of Earth and Environment, University of Leeds, Leeds, UK) for supporting modelling studies. The work on the ozone data sets and model data was done within several projects: DLR SA-DOS, DFG research group SHARP, ESA Ozone-CCI, ESA SCIOLOV-15, ESA SQWG. We thank HLRN for the opportunity to use their facilities for computation.

References

Arosio, C., Rozanov, A., Malinina, E., Eichmann, K. U., Clarmann, T. V., and Burrows, J. P.: Retrieval of ozone profiles from OMPS limb scattering observations. *Atmos. Meas. Tech.*, 11, 2135–2149, 2018.

Chipperfield, M. P.: New version of the TOMCAT/SLIMCAT off-line chemical transport model: Intercomparison of stratospheric tracer experiments, *Quarterly Journal of the Royal Meteorological Society*, 132, 1179–1203, <https://doi.org/10.1256/qj.05.51>, 2006.

Chipperfield, M. P., Bekki, S., Dhomse, S., Harris, N. R. P., Hassler, B., Hossaini, R., Steinbrecht, W., Thiéblemont, R. and Weber, M.: Detecting

recovery of the stratospheric ozone layer, *Nature*, 549, 211–218, doi:10.1038/nature23681, 2017.

Chipperfield, M. P., Dhomse, S., Hossaini, R., Feng, W., Santee, M. L., Weber, M., Burrows, J. P., Wild, J. D., Loyola, D., Coldewey-Egbers, M.: On the Cause of Recent Variations in Lower Stratospheric Ozone. *Geophys. Res. Lett.*, 45, 5718–5726, doi:10.1029/2018GL078071, 2018.

Galytska, E., Rozanov, A., Chipperfield, M. P., Dhomse, S. S., Weber, M., Arosio, C., Feng, W., and Burrows, J. P.: Dynamically controlled ozone decline in the tropical mid-stratosphere observed by SCIAMACHY, *Atmos. Chem. Phys. Discuss.*, <https://doi.org/10.5194/acp-2018-746>, in review, 2018.

Jia, J., Rozanov, A., Ladstätter-Weißenmayer, A., and Burrows, J. P.: Global validation of SCIAMACHY limb ozone data (versions 2.9 and 3.0, IUP Bremen) using ozonesonde measurements, *Atmos. Meas. Tech.*, 8, 3369–3383, 2015.

Steinbrecht, W., Hegglin, M.I., Harris, N., and Weber, M.: Is global ozone recovering?, *C. R. Geosci.*, 368–375, doi:10.1016/j.crte.2018.07.012, 2018.

Weber, M., Coldewey-Egbers, M., Fioletov, V. E., Frith, S. M., Wild, J. D., Burrows, J. P., Long, C. S., and Loyola, D.: Total ozone trends from 1979 to 2016 derived from five merged observational datasets – the emergence into ozone recovery, *Atmos. Chem. Phys.*, 18, 2097–2117, doi:10.5194/acp-18-2097-2018, 2018.

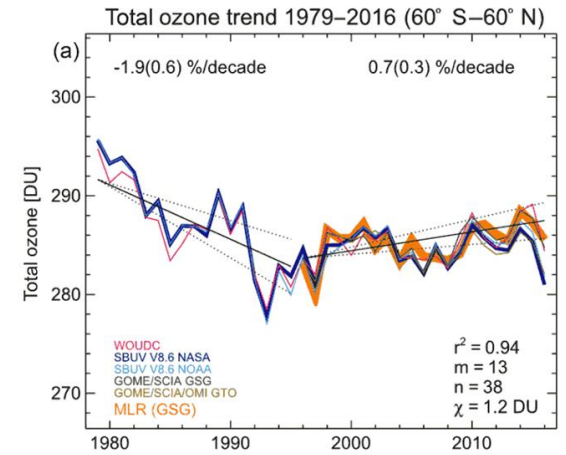


Figure 30: Near-global annual mean total ozone time series from five merged data records. The MLR regression applied to the GSG data is shown by the thick orange line. The linear trend after 1996 and the 2σ uncertainties from the MLR are shown by the solid line and the dotted line, respectively.

Solar variability

Mark Weber, Tina Hilbig, Klaus Bramstedt, Stefan Noël and John P. Burrows

Space-borne UV spectrometer dedicated for atmospheric measurements usually observe regularly the sun. The daily solar spectral irradiance (SSI), itself, are also of large scientific interest as they allow us to investigate irradiance variability due to solar magnetic activity on daily to decadal time scales. Daily SSI irradiance data from space are now available going back to the late 1970s from several atmospheric sounders in combination with dedicated solar missions.

A big challenge for space UV spectral measurements are the optical degradation due to harmful UV radiation and polymerisation of optical surfaces that lead to blinding of the instrument. Complex degradation corrections have to be applied to obtain reliable time series. In the DFG project SCIASOL, we attempt to re-calibrate SCIAMACHY solar irradiance data using an optical bench simulator and a mirror model that accounts for contamination of the external mirror surface. Particularly in the visible spectral range large uncertainties still exist. An improved solar reference spectrum from SCIAMACHY was established (Figure 31). The main improvement was the characterisation of calibration changes from pre-flight ground calibration campaign to post-launch conditions. The agreement of SCIAMACHY with other solar SSI data is usually within 5% or better (Hilbig et al., 2018). Larger differences are observed at lowest wavelengths (below 270 nm) and in the NIR (above 1600 nm). The NIR is currently matter of a scientific debate as more recent solar data including SCIAMACHY show systematically lower SSI than the Atlas-3 composite that is widely considered the

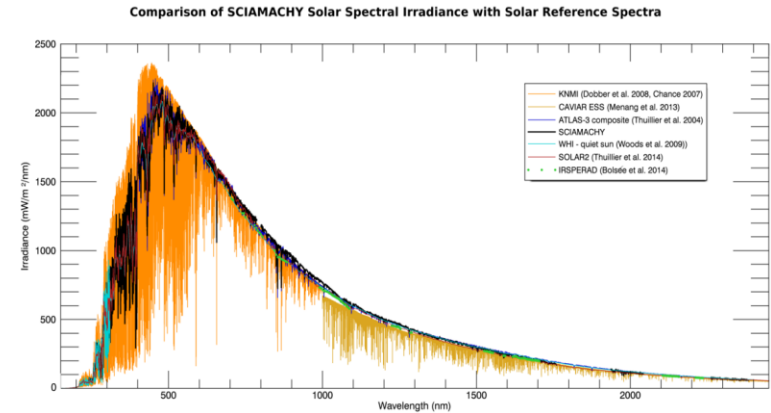


Figure 31: SCIAMACHY reference spectrum and other solar data used for comparisons at their native spectral resolution (Hilbig et al., 2018).

standard for the visible and NIR spectral range (e. g. Meftah et al., 2018). The revised calibration of SCIAMACHY SSI time series has been completed and studies on the variability and trends during solar cycle 23 are underway.

From the solar data of UV atmospheric sounders like GOME, GOME-2, and SCIAMACHY as well as other satellite missions solar proxies can be derived that are largely insensitive to instrument degradation. A popular solar proxy is the Mg II core-to-wing ratio (Mg II index) which can be derived from the Mg II doublet observed at 280 nm. The narrow emission cores of the doublet varies with solar activity and highly correlates with SSI variations in the UV spectral region, thus, it is often used for SSI reconstruction in solar or climate models to investigate the atmospheric effects from direct solar radiation.

We derive the Mg II indices from GOME, SCIAMACHY, and GOME-2 observations and combine them with other available datasets to create the Bremen Composite Mg II index (Snow et al., 2014). This index shows the changes with the

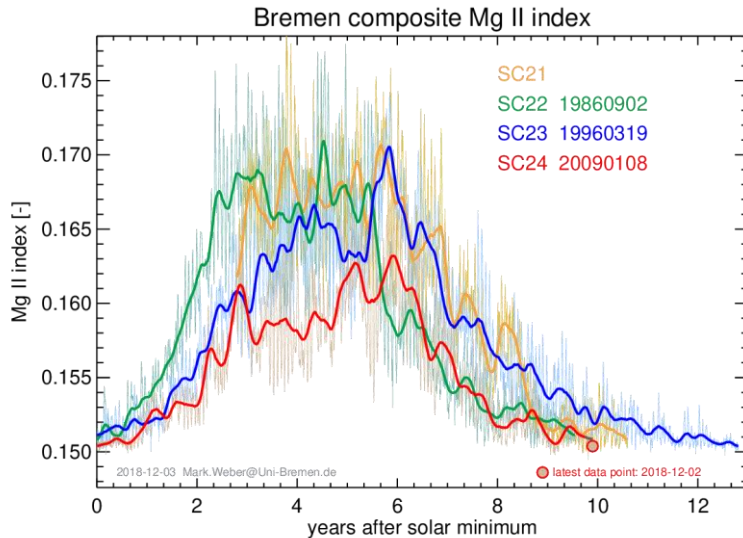


Figure 32: Comparisons of solar activity in solar cycles 21 to 24 using the Bremen Mg II Composite Index. The thick curves show the Mg II index time series twice smoothed with a 55-day boxcar. Dates of minima of solar cycles (YYYYMMDD) were determined from the smoothed Mg II index. UV solar activity was lower in solar cycle 24 compared to the three previous cycles (Daily updates available from <http://www.iup.uni-bremen.de/UVSAT/Datasets/mgii>).

Schwabe (11-year magnetic activity) and Carrington (27-day solar rotation) cycles and now spans 40 years. The solar minimum following solar cycle 23 (in 2009) was one of the quietest periods (with virtual no solar modulation) compared to the previous ones. The most recent solar cycle 24 had a much lower activity maximum (~ 2009) than cycles 22 and 23. The length and amplitude of the various solar cycles are very variable as shown in Figure 32.

References:

- Hilbig, T., Weber, M., Bramstedt, K., Noël, S., Burrows, J. P., Krijger, J. M., Snel, R., Meftah, M., Damé, L., Bekki, S., Bolsée, D., Pereira, N. and Sluse, D.: The New SCIAMACHY Reference Solar Spectral Irradiance and Its Validation, *Sol. Phys.*, 293, 121, doi:10.1007/s11207-018-1339-9, 2018.
- Meftah, M., Damé, L., Bolsée, D., Hauchecorne, A., Pereira, N., Sluse, D., Cessateur, G., Irbah, A., Bureau, J., Weber, M., Bramstedt, K., Hilbig, T., Thiéblemont, R., Marchand, M., Lefèvre, F., Sarkissian, A. and Bekki, S.: SOLAR-ISS: A new reference spectrum based on SOLAR/SOLSPEC observations, *Astron. Astrophys.*, 611, A1, doi:10.1051/0004-6361/201731316, 2018.
- Snow, M., M. Weber, J. Machol, R. Viereck, and E. Richard: Comparison of Magnesium II core-to-wing ratio observations during solar minimum 23/24, *J. Space Weather Space Clim.*, 4, A04, doi:10.1051/swsc/2014001, 2014.

Tropospheric ozone trends

Mark Weber, Elpida Leventidou, K.-U. Eichmann and John P. Burrows

Tropospheric ozone (O_3) is an important greenhouse gas and plays an important role in the tropospheric chemistry of CO , CH_4 , NO_x , radicals, halogen compounds, and hydrocarbons and is thus a common pollutant in the urban environment. Enhanced levels of tropospheric ozone impact human health and reduce crop productivity. Due to its lifetime of about 22 days, it can be transported into remote regions and across continents. Over the last century, tropospheric ozone levels were increasing, however, very recent observations from satellites and ground show contradicting trends. The measurement of tropospheric ozone from space is quite challenging as the ozone signal observed is generally dominated by ozone in the stratosphere, which is on average a factor of nine higher in abundance there than in the below lying troposphere.

We apply a residual method, called the Convective-Cloud-Differential (CCD), to determine tropospheric ozone columns from UV nadir satellite measurements. This method subtracts the measured ozone columns above high convective clouds (over the Western Pacific) from measured total ozone columns under clear-sky conditions (at all longitudes) to obtain the tropospheric column. One assumption here is that stratospheric ozone remains invariant which limits the application to the tropical region. The tropospheric column is usually determined as an ensemble average in a grid box and covering one month. The CCD method was successfully applied to GOME, SCIAMACHY, and GOME-2A satellite data (Leventidou et al., 2016). Tropospheric ozone columns from all satellites were validated by comparisons with ozone sondes yielding generally good agreement. For the first time

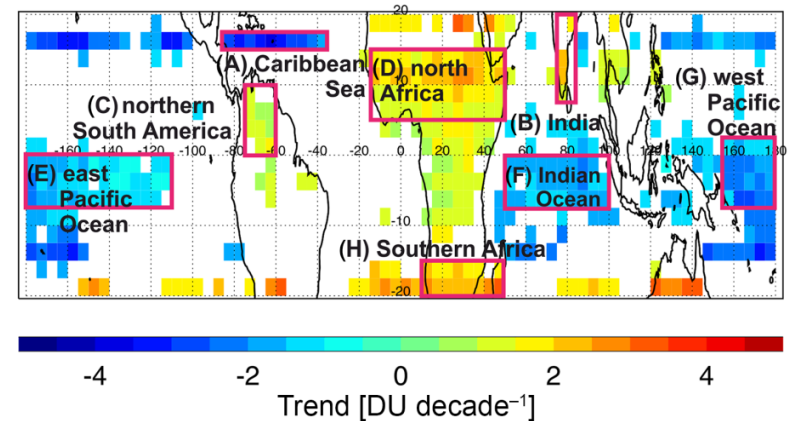


Figure 33: Significant tropospheric ozone trends observed from the merged CCD_IUP data (1995-2015). The narrow band with negative trends in the northern tropical region may be an artefact due to the very low numbers of clouds in the Pacific reference regions (used to determine the above cloud column ozone). From Leventidou et al. (2018)

a detailed uncertainty budget was established for this type of retrieval (Leventidou et al., 2016).

The three satellite datasets were combined into one merged dataset by removing biases between pairs of satellite measurements. As a reference (to match all other data to) the intermediate SCIAMACHY time series was selected. The merged tropospheric ozone data covers 20 years of observations and are well suited to establish long-term trends (Leventidou et al., 2018). Some sensitivity studies were done to check how the harmonization approaches to merge the data impact the trends. It was demonstrated that this can change the established trend beyond the uncertainty levels obtained from the multivariate linear regression applied to the data. The optimal merging approach was the one which only applied bias corrections for GOME and GOME-2 to match the SCIAMACHY data. Although some drifts between datasets were apparent, the overlap periods were generally

too short to obtain reliable drift estimates (Leventidou et al. 2018).

Figure 33 shows tropical regions where statistical significant trends were observed during the period 1995-2016. Over the African continent, trends are positive (+1 to +3 DU/decade), over large parts of the Pacific Ocean and Indian Ocean, trends are negative (up to about -4 DU/decade). Overall the mean of tropospheric ozone over the entire tropical region shows near zero trend over the twenty year period. The variability of tropospheric ozone with changes in the Quasi-biennial Oscillation (QBO) and El Nino were studied as well. The response of El Nino and QBO on tropospheric ozone is shown in Figure 34. During El Nino phases (e.g. in 2015) enhanced biomass burning contributes to higher tropospheric ozone in the Indonesian region and western Pacific. Both El Nino and QBO have a strong influence on tropical meteorology and long-range transport of tropospheric ozone.

In support of the new Sentinel 5P satellite mission (since 2017), IUP developed a prototype algorithm for determining free tropospheric ozone using the cloud slicing method. The extension of the CCD time series by including S5P data into our merged time series is in preparation.

References

Leventidou, E., Eichmann, K.-U., Weber, M., and Burrows, J. P.: Tropical tropospheric ozone columns from nadir retrievals of GOME-1/ERS-2, SCIAMACHY/Envisat, and GOME-2/MetOp-A (1996–2012), *Atmos. Meas. Tech.*, 9, 3407-3427, doi:10.5194/amt-9-3407-2016, 2016.

Leventidou, E., Weber, M., Eichmann, K.-U., Burrows, J. P., Heue, K.-P., Thompson, A. M., and Johnson, B. J.: Harmonisation and trends of 20-year tropical tropospheric ozone data, *Atmos. Chem. Phys.*, 18, 9189-9205, doi:10.5194/acp-18-9189-2018, 2018.

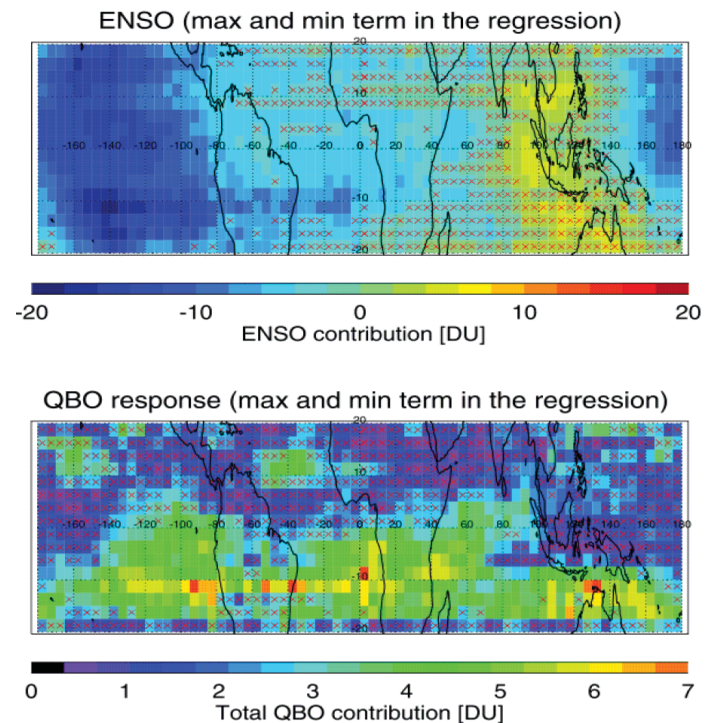


Figure 34: El Nino-Southern Oscillation and QBO Response to tropical tropospheric ozone during the period 1995 to 2015 (Leventidou, PhD Thesis, University of Bremen, 2018).

Analysis of stratospheric water vapour and methane profiles from SCIAMACHY solar occultation

Stefan Noël, Katja Weigel, Klaus Bramstedt, Alexei Rozanov, Mark Weber, Heinrich Bovensmann and John P. Burrows

Water vapour (H_2O) and methane (CH_4) in the stratosphere are not only important for stratospheric chemistry, for example in the context of ozone depletion and generation of polar stratospheric clouds (PSCs), they can also be used as tracers to investigate dynamical processes of the atmosphere.

Recently, an updated stratospheric water vapour data set has been derived from solar occultation measurements of the SCanning Imaging Absorption spectroMeter for Atmospheric CHartography (SCIAMACHY) which operated between 2002 and 2012 on Envisat.

The retrieval is based on the Onion Peeling DOAS (ONPD) method, which combines an onion peeling approach with a weighting function DOAS fit (see Noël et al., 2018, and references therein). The same retrieval method has already been successfully applied to methane and carbon dioxide (CO_2), see Noël et al. (2016), such that now a consistent data set for all three major greenhouse gases is available.

The SCIAMACHY solar occultation profile data cover the latitudinal range between about 50°N and 70°N with a specific temporal sampling pattern due to the sun-fixed orbit of Envisat. Data are available for the complete SCIAMACHY time interval (August 2002 to April 2012) and altitudes between 17 km and 45 km.

The new SCIAMACHY water vapour profiles have been compared with different independent data sets showing agreement

within about 5%. Earlier studies revealed an accuracy of the corresponding methane data in the order of 5-10%.

From the combination of methane and water vapour data it is possible to derive information about sources and transport of water vapour in the stratosphere.

Figure 35 shows time series of monthly anomalies derived from the SCIAMACHY methane and water vapour data.

As can be seen from this figure, there is a clear anti-correlation between water vapour and methane for altitudes above about 20 km. This is expected, because water vapour in the stratosphere is mainly produced by oxidation of methane, such that the sum of volume mixing ratios $[\text{H}_2\text{O}] + 2[\text{CH}_4]$, sometimes referred to as potential water (PW), is conserved.

Furthermore, the observed variations show a clear signature of the Quasi-Biennial Oscillation (QBO); see also Figure 37. This

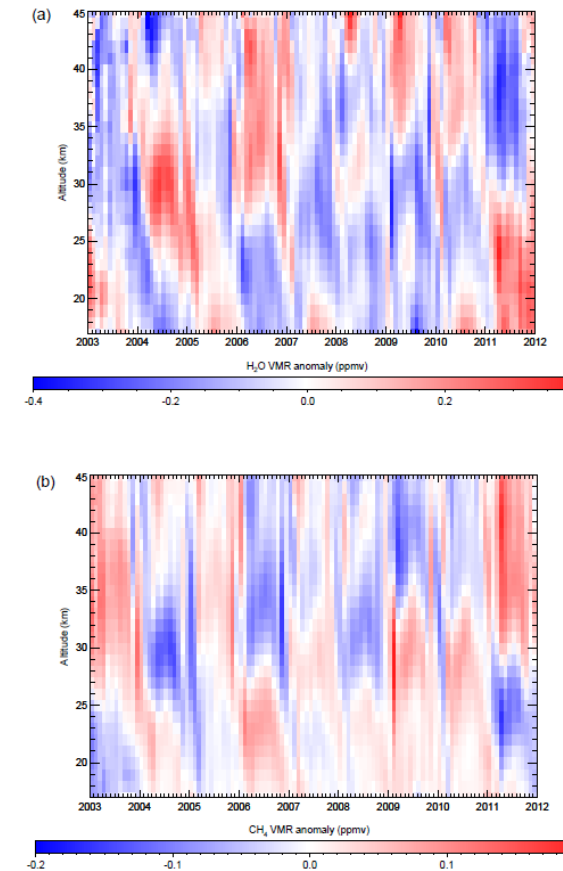


Figure 35: Time series of water vapour (top) and methane (bottom) monthly anomalies (from Noël et al., 2018).

indicates that this altitude range (at higher mid-latitudes) is affected by transport from the tropics.

At altitudes below about 20 km the QBO signature is only visible in the water vapour but not the methane data. This indicates, that at these altitudes water vapour is not produced by methane oxidation but is directly transported from the tropics.

These findings confirm our understanding of the different pathways of the Brewer-Dobson circulation (see Figure 36). Altitudes above about 20 km are fed via the so-called deep (upper) branch of the Brewer-Dobson circulation, where air is transported upwards in the tropics and then horizontally to higher latitudes where it sinks down again. Along this transport (which usually takes several years), methane is effectively converted into water vapour, resulting in a strong correlation between both species. The observed QBO signal originates from QBO-related changes of vertical transport in the tropics. Below

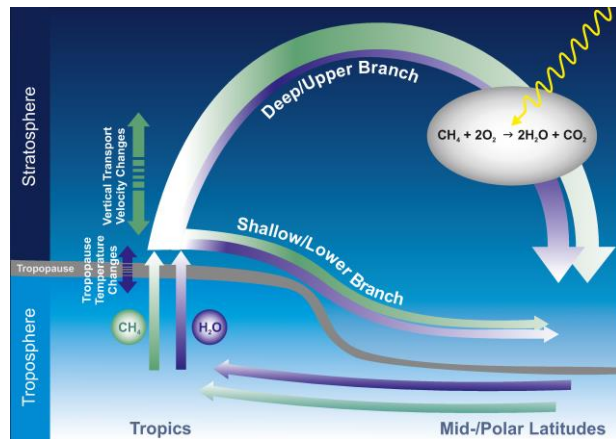


Figure 36: Simplified schematic view showing different transport pathways within the Brewer–Dobson circulation (from Noël et al., 2018).

20 km, part of the water vapour and methane entering the stratosphere in the tropics is transported to higher latitudes via the shallow (or lower) branch of the Brewer-Dobson circulation. This transport pathway is much faster. Furthermore, less UV radiation (required for the oxidation of methane) reaches these altitudes. Therefore, the conversion of methane to water vapour is less effective, which explains the missing (anti-)correlation at lower altitudes. The QBO signal in the water vapour data below 20 km can be explained by tropical tropopause temperature changes related to QBO. These temperature variations affect the entry of water vapour into the stratosphere, but not methane.

References

- Noël, S., K. Bramstedt, M. Hilker, P. Liebing, J. Plieninger, M. Reuter, A. Rozanov, C. E. Sioris, H. Bovensmann and J. P. Burrows: Stratospheric CH4 and CO2 profiles derived from SCIAMACHY solar occultation measurements, *Atmos. Meas. Tech.*, 9(4), 1485-1503, doi: 10.5194/amt-9-1485-2016, 2016.
- Noël, S., K. Weigel, K. Bramstedt, A. Rozanov, M. Weber, H. Bovensmann and J. P. Burrows: Water vapour and methane coupling in the stratosphere observed using SCIAMACHY solar occultation measurements, *Atmos. Chem. Phys.*, 18(7), 4463-4476, doi: 10.5194/acp-18-4463-2018, 2018.

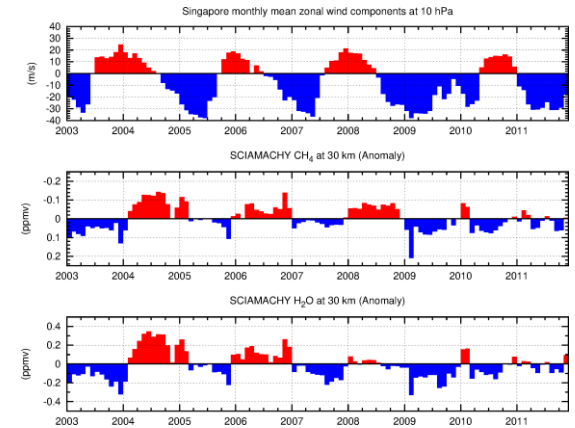


Figure 37: Time series of water vapour and methane anomalies at 30 km and Singapore zonal wind (indicator for QBO) at 10 hPa (from Noël et al., 2018).

Top-of-Atmosphere studies over a changing Arctic

Marco Vountas Marco, Narges Khosravi, Luca Lelli, Linlu Mei and John P. Burrows

Arctic near-surface temperatures during the last decades have increased twice as much as observed on a global scale. This observation is commonly referred to as Arctic Amplification.

In order to get insights in to the origins and evolution of Arctic Amplification, we examine the Top-of-Atmosphere Reflectance (RTOA) to assess the assumption whether long-term changes (>20 years) of spectral RTOA can identify Arctic climate change through changes of the surface and atmospheric constituents.

The primary measured quantity in all vis/NIR satellite remote sensing products is the RTOA which is defined as the solar zenith angle-normalized ratio of upwelling radiance to the extra-terrestrial solar irradiance. RTOA values were prepared at different wavelengths and evaluated at 0.5° grid resolution for the whole Arctic and topical studies. In Figure 39, ten years of RTOA at 620 nm derived from the Global Ozone Monitoring Experiment-2 mission (GOME-2) were gridded and depicted.

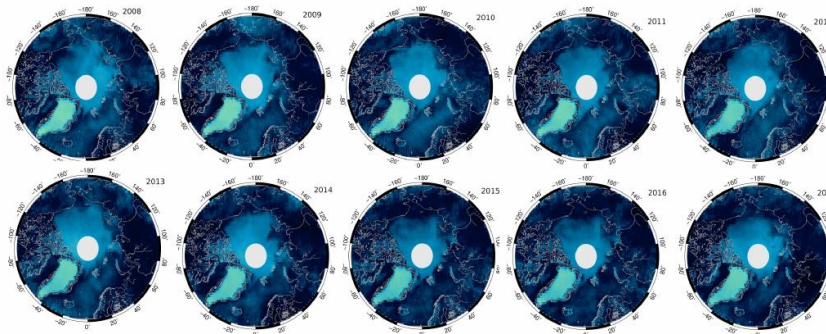


Figure 39: RTOA (at 620 nm) for 10 years of GOME-2 (METOP-A) measurements.

A prominent feature in the Arctic Circle is the reported change in surface brightness over the Greenland Ice Shield (GrIS) which can be well reproduced by using RTOA values over a time span of 15 years from GOME-2 and from the Scanning Imaging Absorption Spectrometer for Atmospheric Chartography (SCIAMACHY) instrument. Both datasets have been gridded at 620 nm for the GRIS for all months of July from 2003 until 2018, temporally concatenated and the monthly average for all (July) values has been subtracted, i.e. anomalies have been created (de-seasonalization). Figure 38 shows the anomalies of the RTOA at 620 nm for the GRIS compared to surface reflectance retrievals using surface albedo retrievals based on the Global Land Surface Satellite (GLASS) project utilizing MODIS data during this period (He et al., 2012). The overall agreement in the decreasing trend, i.e. the darkening of the GRIS, is obvious in the RTOA even though no attempt was made to remove clouds. Both trends, despite their different lengths show -2.9%/decade indicating the potential of the use of RTOA as an indicator for Arctic Amplification.

References:

He, T., Liang, S., Yu, Y., Wang, D., Gao, F., and Liu, Q.: Greenland surface albedo changes in July 1981-2012 from satellite observations, *Environ. Res. Lett.*, 8, 044043, <https://doi.org/10.1088/1748-9326/8/4/044043>, 2013.

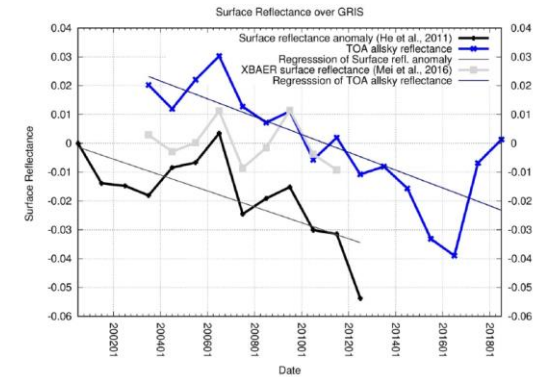


Figure 38: Anomalies of the RTOA at 620 nm for the GrIS compared to the anomalies of surface reflectance retrievals using surface albedo retrievals based on the Global Land Surface Satellite (GLASS) project utilizing MODIS data during this period (He et al., 2012).

Retrieval of cloud optical properties in presence of increased aerosols loading

Linlu Mei, Marco Vountas, Luca Lelli, Vladimir Rozanov and John P. Burrows

The crucial influence of atmospheric aerosols, i.e. suspended solid particles or liquid droplets in air, on cloud formation and their role in changing the precipitation efficiency is well-known. However, only rarely aerosol and cloud properties are retrieved simultaneously from space-borne instrumentation – thus limiting our knowledge on a larger scale. For instance, Aerosol Optical Thickness (AOT) retrievals based on global measurements from single-view, multi-spectral imagers are mostly limited to clear sky scenes. However, large regions over the south-eastern Atlantic Ocean are affected by frequent dust and/or biomass burning events while overcast is present. For example, smoke often covers low stratocumulus liquid water clouds during episodes from July to September across parts of the south-eastern Atlantic at synoptic scales.

Similarly, Saharan desert dust plumes overlay low-level water clouds from June to August over the tropical Atlantic Ocean. Accordingly, proper knowledge of both aerosol and cloud optical properties is needed in such regions. This study aims to close the gap of information by introducing a novel method for the retrieval of aerosol and cloud properties, such as Cloud Optical Thickness, Cloud Effective Radius and AOT, for aerosol contaminated clouds. In Figure 40, a desert dust outbreak over the tropical Atlantic Ocean is shown for July 2007. Desert dust is advected over and into a field of clouds. While in the majority of the cases operational cloud and aerosol algorithms mutually exclude the other property to be retrieved as can be seen in Figure 40 (left column) the novel

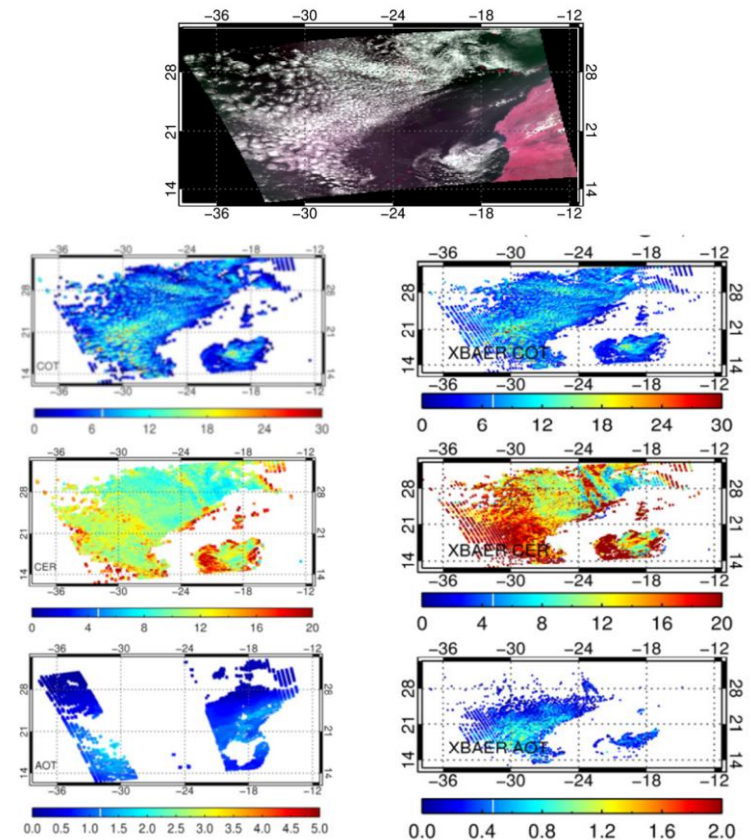


Figure 40: An RGB composite image for the study region located near southern Africa on July 12, 2007. The left column shows corresponding MODIS operational cloud and AOT products. The right hand column shows the results from this study.

approach enables simultaneous retrieval over larger regions of the scene (see Figure 40, right column) with very promising results (and validation).

Covariations of aerosol properties and cloud bottom altitude from multi-sensor space borne measurements

Luca Lelli and Marco Vountas

Interactions of small-sized aerosol particles, described by their ability to extinguish sunlight (aerosol optical depth - AOD) with the bottom altitude of clouds provides insight on the thermodynamical and microphysical controls of the development of tropospheric clouds. For this study, aerosol and cloud records are derived from coincident measurements of the Advanced Along-Track Scanning Radiometer (AATSR) and the SCanning Imaging Absorption spectroMeter for Atmospheric CHartographY (SCIAMACHY), both being part of the sensor payload of the European Environmental Satellite (EnviSaT), for the period 2003 - 2009. Upon long-term validation of the space borne cloud bottom height (CBH) with lidar measurements at three ground-based Atmospheric Radiation Measurement (ARM) facilities, we selected six regions above water masses that are characterized by seasonal variations between winter and summer months of both quantities. Sea surface temperature is seen to consistently determine variations of absolute CBH values, whereas CBH anomalies are mostly seen to be negatively correlated with AOD_{fm} (AOD fine mode). In particular, this relationship holds for those regions close to natural and anthropogenic aerosol source emissions.

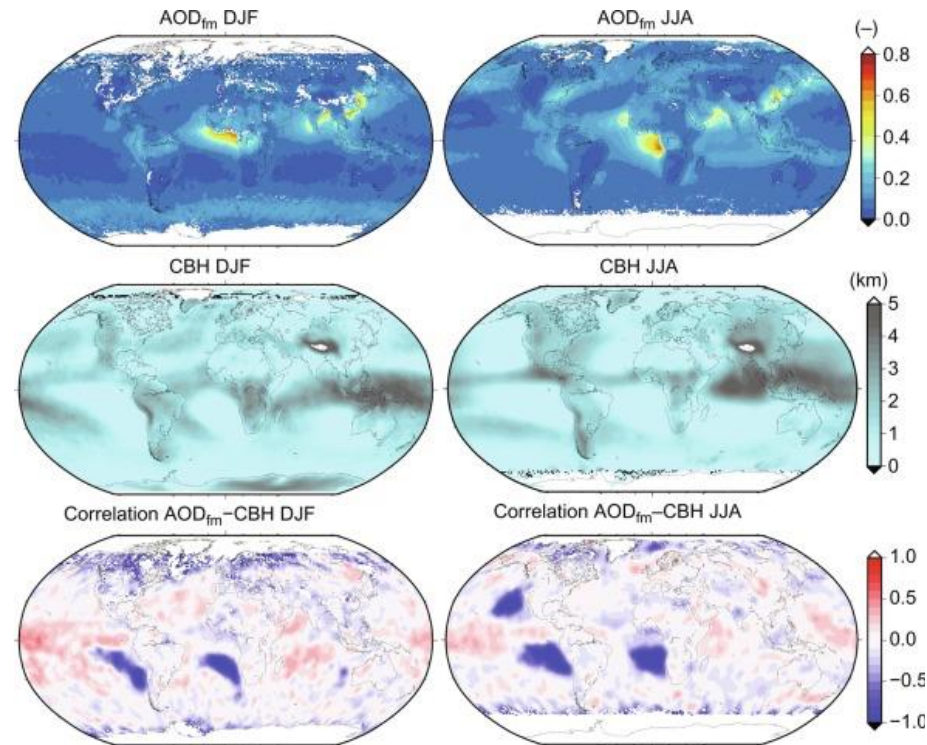


Figure 41: AATSR fine mode aerosol optical thickness (AOD_{fm}) at 550 nm (top), SCIAMACHY cloud bottom height (middle), and their correlation (bottom) for winter (left) and summer (right) months. Data spans years 2003 - 2009.

Reference:

Lelli, L. and Vountas, M.: Chapter 5 – Aerosol and Cloud Bottom Altitude Covariations From Multisensor Spaceborne Measurements, In Remote Sensing of Aerosols, Clouds, and Precipitation, edited by Tanvir Islam, Yongxiang Hu, Alexander Kokhanovsky and Jun Wang, Elsevier, pp 109-127, ISBN 9780128104378, <https://doi.org/10.1016/B978-0-12-810437-8.00005-0>, 2018.

Greenhouse gas observations from aircraft: Methane Airborne Mapper (MAMAP) and Europe's largest source of the greenhouse gas Methane

Konstantin Gerilowski, Sven Krautwurst, Jakob Borchardt, Michael Buchwitz, John P. Burrows and Heinrich Bovensmann

The two most important greenhouse gases (GHG) carbon dioxide (CO₂) and methane (CH₄) have strong sources on small spatial scales (100 m to a few km). These are for example CO₂ from power plants, volcanoes and cities, or CH₄ from fossil fuel production (coal, gas, oil), landfills and geological seeps. Often the strength and/or the position of these sources are not well known and an independent verification of the emissions from remote sensing is needed. Airborne remote sensing of atmospheric GHG distributions, so-called greenhouse gas imaging, could close an important information gap on small spatial scales. At IUP Bremen the development and application of the airborne spectrometer system called MAMAP (Methane Airborne MAPper) demonstrated that imaging the spatial distribution of atmospheric GHG concentrations in the vicinity of strong sources can be used to infer the emission strength of the source. The spectrometer uses solar absorption spectroscopy in the near and short-wave infrared, similar as the satellite sensors SCIAMACHY, GOSAT, or Sentinel-5P to derive very accurate (preci-

sion better < 0.3%) gradients in atmospheric CO₂ and CH₄ with a spatial resolution of approx. 50 m over spatial scales of several km.

During the years 2017 - 2018 the main focus of the MAMAP group at IUP Bremen was the preparation of a measurement campaign in Upper Silesian Basin (Poland) and the development of the successor of MAMAP the MAMAP2D system.

The coal mining area in the Upper Silesian Basin around the city of Katowice, Poland, is the largest sources of methane gas emissions in Europe and the focus of the COMET (Carbon dioxide and Methane Mission) measurement campaign in May/June 2018. This campaign is part of a larger research activity being coordinated by the German Space Agency (DLR – Deutsches Zentrum für Luft- und Raumfahrt) to determine the distribution of methane gas emissions. COMET is a collaboration between the DLR the University of Bremen and Berlin, the Cracow University of Technology and the Max-Planck-Institute of Chemistry in Jena. The IUP-UB instrument MAMAP was flown on board the Cessna aircraft owned by the Free University of Berlin, and research flights took place in May/June 2018. The research team was able to achieve a precise and unique set of coordinated overflights involving four participating aircraft during 4 days, as well as coordinated measurements with the mobile ground based teams.



Figure 43: MAMAP team and FUB Cessna team (left aircraft) as well as DLR team (right aircraft) at Katowice airport.

A global reduction of greenhouse gas emissions necessitates an effective monitoring of greenhouse gases. One of the scientific objectives of project COMET is to test novel methods for determining regional methane emissions. Data gathered by different systems, whether ground-based sensors, airborne instruments or on satellites, are needed to obtain a more detailed picture of the region's methane emissions. Polish research partners were responsible for gathering the ground-based measurements and also establishing contacts with the coal mining companies.

The MAMAP is a worldwide one-of-a kind methane and CO₂ sensor developed by the University of Bremen. In order to have successful flights, piloting skills and forecasting expertise are essential. These are provided by the team from the Free University of Berlin. The flight weather forecasts play an important role in coordinating ground-based and airborne measurements. Initial results were presented and discussed in a workshop in October 2018 in Bremen and will be further presented at international conferences in 2019.

Beside preparation and execution of the COMET campaign, the team at IUP Bremen also further developed the concept of 2-dimensional imaging of CH₄ and CO₂ distributions. That will allow performing similar measurements as with MAMAP (1D), but on time scales of approx. 10 minutes instead to several hours, which will increase the detection limit of small sources by nearly an order of magnitude and will minimise systematic errors during measurement time due to changing meteorological conditions. The activities of the IUP-UB MAMAP team are funded by the DFG (COMET), the BMBF (via DLR-PT, AIRSPACE project) and the University of Bremen.

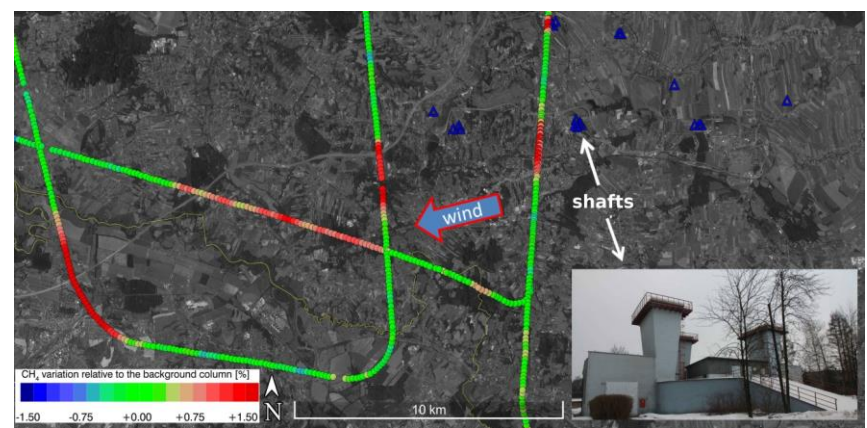


Figure 44: CH₄ plume as measured by MAMAP during the COMET campaign. The plume is originating from a cluster of coal mine ventilations shafts (blue triangles), where the air from inside the coal mine is vented into the atmosphere.

References:

Krings, T., Leifer, I., Krautwurst, S., Gerilowski, K., Horstjann, M., Bovensmann, H., Buchwitz, M., Burrows, J.P., Kolyer, R.W., Jonsson, H.H., Fladeland, M.M.: Reduced Methane Emissions from Santa Barbara Marine Seeps. *Remote Sens.*, 9, 1162, 2017.

Krautwurst, S., Gerilowski, K., Jonsson, H. H., Thompson, D. R., Kolyer, R. W., Iraci, L. T., Thorpe, A. K., Horstjann, M., Eastwood, M., Leifer, I., Vigil, S. A., Krings, T., Borchardt, J., Buchwitz, M., Fladeland, M. M., Burrows, J. P., and Bovensmann, H.: Methane emissions from a Californian landfill, determined from airborne remote sensing and in situ measurements, *Atmos. Meas. Tech.*, 10, 3429-3452, <https://doi.org/10.5194/amt-10-3429-2017>, 2017.

Krings, T., Neisinger, B., Gerilowski, K., Krautwurst, S., Buchwitz, M., Burrows, J. P., Lindemann, C., Ruhtz, T., Schüttemeyer, D., and Bovensmann, H.: Airborne remote sensing and in situ measurements of atmospheric CO₂ to quantify point source emissions, *Atmos. Meas. Tech.*, 11, 721-739, <https://doi.org/10.5194/amt-11-721-2018>, 2018.

Airborne observations in selected outflows from European and Asian megacities

Maria Dolores Andrés Hernández, Vladyslav Nenakhov, Midhun George, Yangzhuoran Liu and John P. Burrows

The first megacities, defined most frequently as conurbations having over 8-10 million people, evolved at the beginning of the 19th century. Since then, the number and size of what is generally called major population centres (MPC) have increased worldwide and have brought the attention of the scientific community to their effect on global air pollution and climatic change.

The specific impact of pollution plumes from MPCs depends not only on the type of emissions (e.g. industry, traffic, domestic heating, generation of electricity etc.) but also on the regional topography, geography and meteorology determining transport and transformation processes. These are still poorly understood in MPC outflows and airborne measurements of suitable resolution are required for further characterisation (Zhu et al., 2012).

In this context, the project EMeRGe (Effect of Megacities on the Transport and Transformation of Pollutants on the Regional to Global scales) started in 2016 as a German consortium of five universities and five research centres under the scientific coordination of IUP Bremen. Europe and East Asia were selected for the investigation as to be suitable points of comparison of pollution outflows from urban agglomerations of different size, emission and transport patterns, as well as for the study of potential MPC synergies.

Two complementary intensive airborne field experiments using an optimised instrumental payload for aerosol and trace gas measurements on board of the research aircraft HALO (www.halo.dlr.de) and comprising a total of 180 flight hours were carried out in July 2017 and March-April 2018.

Apart from the scientific and logistical coordination of the EMeRGe project, the TROLAS group at IUP-UB participated in the HALO campaigns with the airborne measurement of peroxy radicals by using the PeRCEAS (Peroxy Radical Chemical Enhancement and Absorption Spectrometer) instrument, which provides essential information about oxidation processes in the pollution outflows.

Seven flights were carried out over Europe (Figure 45) targeting the outflows of London, Paris, Rome, Po Valley, Benelux/Ruhr, Southern France, Madrid, Barcelona, and the transport patterns over the Alps, Apennines, Central Europe, in the English Channel and the Mediterranean Sea.

Over Asia, 12 HALO flights were carried out for the in-

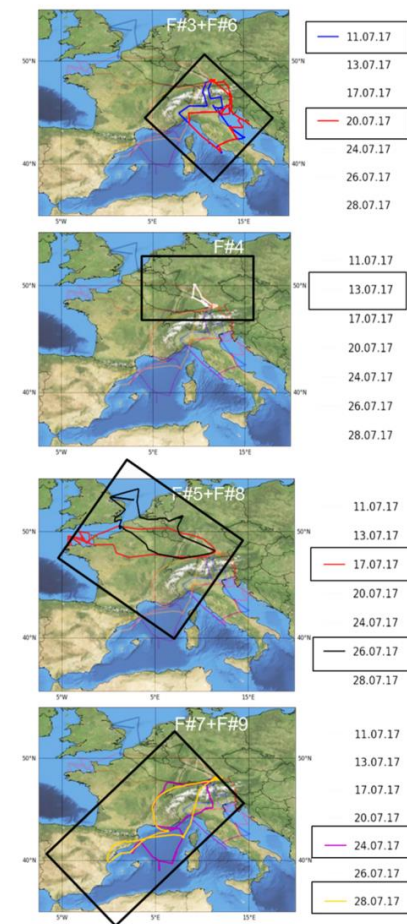


Figure 45: HALO flight tracks during the EMeRGe campaign in Europe. Different MPC targets and transport paths were investigated: Rome, Po Valley and the transport over the Alps and Apennines (F#3 and F#6); central Europe (F#4); Paris, London, Benelux/Ruhr and the transport over the English Channel (F#5 and F#8); South France, Madrid, Barcelona and the transport in the western Mediterranean (F#7 and F#9).

investigation of the Taipei and Manila outflows as well as the transport of Chinese, Japanese and Korean megacity outflows in the East China Sea, and of Bangkok in the Gulf of Thailand (Figure 46).

The current understanding of the impact of MPC outflows will be tested by the ongoing comprehensive integrated analysis of observational data from aircraft campaigns, satellites, tracer releases and ground measurements obtained within a large best effort EMERGE international community.

www.iup.uni-bremen.de/emerge/

References:

Zhu, T., Melamed, M.L., Parrish, D., Gauss, M., Gallardo Klenner, L., Lawrence, M., Konare, A., and C. Liousse, 2012: Impacts of megacities on air pollution and climate. WMO/IGAC/ GAW report N° 205 (http://library.wmo.int/pmb_ged/gaw_205.pdf)

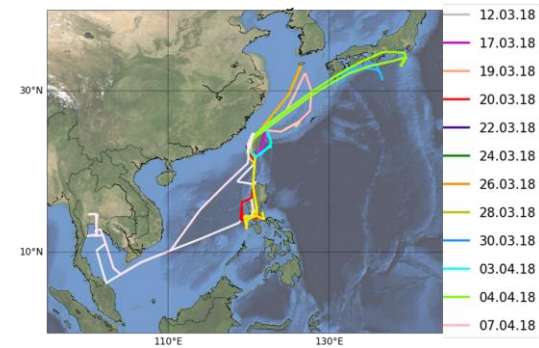


Figure 46: HALO flight tracks during the EMERGE campaign in Asia in March-April 2018.

Imaging DOAS NO₂ measurements during the AQABA ship campaign

Lisa K. Behrens, Andreas Hilboll, Andreas Richter, Enno Peters, John P. Burrows and Mihalis Vrekoussis

In 2017, the IUP Bremen LAMOS and DOAS groups jointly participated in the campaign Air Quality and Climate Change in the Arabian Basin (AQABA), conducted from June to September. For this cruise, a new imaging DOAS instrument was installed on board of the research vessel “Kommandor Iona” for ship-based air quality measurements. The imaging DOAS instrument is called Imaging MaPper for Atmospheric observations (IMPACT).

For the AQABA campaign, the instrument which was previously operated from the ground was installed on a ship for the first time. The cruise went from Toulon (France) to Kuwait City (Kuwait) and back, passing the Mediterranean Sea, the Red Sea, the Arabian Sea, and the Arabian Gulf (Figure 47). Thus, the cruise allowed observations of different pollution regimes, e.g., pollution due to the presence of oil/gas rigs and ships in the Arabian Gulf, and partly clean marine air in the Mediterranean Sea.

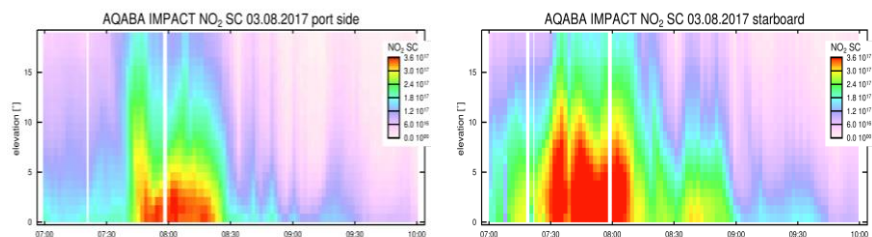


Figure 48: NO₂ measurements in different elevation angles during the departure from Kuwait (beginning of 2nd leg), when the port side (left) was facing the Arabian Gulf and the starboard side (right) was facing the Kuwaiti land.

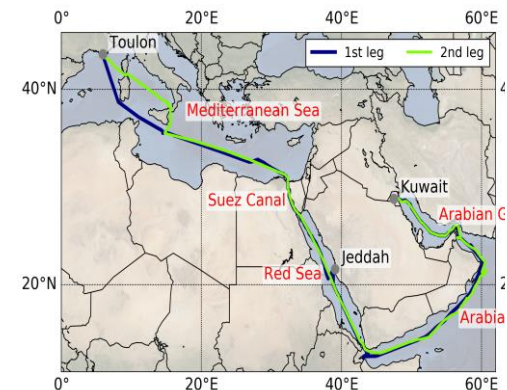


Figure 47: Cruise track of AQABA.

The telescope of the instrument has a 45° field of view which is covered by 50 sorted single quartz fibres observing in different elevation angles. Due to the same order at both sides of the fibre optics and the use of an imaging spectrometer, the spatial information is preserved. Therefore, the different elevation angles can be measured simultaneously. During the campaign, the instrument was continuously scanning a vertical plane of three azimuth angles: starboard, port side, and bow direction.

The instrument operated successfully on the research vessel and polluted areas were detected. For example during the departure in Kuwait, large NO₂ slant columns (SCs) were observed. The SCs are smaller on the port side than on starboard where the city was located (Figure 48). Generally, the largest NO₂ SCs are observed close to the ground. Similar results were found for the arrival at the Suez Canal. Also here the highest values are observed for lowest elevation angles, implying that the NO₂ was located close to the surface. For the Suez Canal, similar results were also observed during the 1st leg.

References

Behrens, L.K., Hilboll, A., Richter, A., Peters, E., Dörner, S., Burrows, J.P., Vrekoussis, M., Imaging DOAS NO₂ measurements during the AQABA ship campaign, EGU General Assembly, Vienna, Austria, April 2018. (www.doas-bremen.de/posters/egu_2018_behrens.pdf)

Molecular spectroscopy laboratory

Victor Gorshchev, Mark Weber and John P. Burrows

Algorithms that retrieve trace gas amounts from remotely sensed spectral data rely, among others, on spectroscopic data characterizing the molecular absorption. Errors and uncertainties in spectroscopic data often limit the accuracy of the retrieval results.

Although numerous spectroscopic datasets based on laboratory measurements and theoretical considerations are already available, in many cases they are not of sufficient quality and there is still room for improvements that benefit the retrieval accuracy.

Advances in experimental instrumentation and setups allow us to produce spectroscopic parameters with lower uncertainties.

Acquisition of high-quality spectroscopic data for remote sensing applications is an essential part of the experimental activity at our Molecular Spectroscopy Laboratory.

In our laboratory, we perform spectroscopic measurements using an Echelle spectrometer covering the UV spectral region and a Fourier transform spectrometer (FTS) encompassing the near UV, visible, and near IR. Several absorption cell setups with extended cooling capacities allow us to measure molecular absorption cross-sections at atmospherically relevant temperatures ranging from -80°C to room temperature.

MERLIN (**M**ethane **R**emote Sensing **L**IDAR **M**ission) is a joint French - German mission dedicated to methane observations in the Earth atmosphere. Destined to launch in 2024, MERLIN will use a LIDAR-Instrument (**L**ight **D**etection and **R**anging) to track and observe the greenhouse gas from an orbit at 500 km altitude. The goal of the mission is generation of global maps of methane concentration distribution. In addition, MERLIN will allow to determine which regions Act as methane sources and sinks (Figure 49).

Within the SMERLIN (Spectroscopy for MERLIN) project, laboratory measurements and corresponding data analysis involving advanced absorption line shape profiles are being performed in order to improve spectroscopic line parameters for CH_4 in the spectral region used by MERLIN ($6074\text{--}6078\text{ cm}^{-1}$, focus on the vicinity of $R(6)$ manifold at 6077 cm^{-1} , or $1.64\text{ }\mu\text{m}$) (Figure 50).

Other recent measurement campaigns of the Molecular Spectroscopy Laboratory include the acquisition of ozone absorption cross-sections in the UV-VIS-IR spectral range from 210 to 1100 nm at an unprecedented high number of temperatures and selected methane absorption lines and bands in the short-wave infrared (SWIR).

The Molecular Spectroscopy Laboratory is also involved in several educational projects, introducing the basic practical concepts of absorption spectroscopy to high school students and participating in the international postgraduate programme in Environmental Physics.



Figure 49: Artist's conception of the MERLIN satellite which will monitor atmospheric methane using a lidar instrument. (CNES/Illustration D. Ducros)

References

Gorshchev V., Serdyuchenko A., Weber M., and Burrows J.P.: High spectral resolution ozone absorption cross-sections: Part I. Measurements, data analysis and comparison around 293 K, *Atmos. Meas. Tech.*, 7, 609–624, 2014.

Serdyuchenko A., Gorshchev V., Weber M., Chehade W., and Burrows J.P.: New high-resolution ozone absorption cross-sections in UV, visible and near infrared: Part II. Temperature dependence, *Atmos. Meas. Tech.*, 7, 625–636, 2014.

Weber, M., Gorshchev, V., and Serdyuchenko, A.: Uncertainty budgets of major ozone absorption cross-sections used in UV remote sensing applications, *Atmos. Meas. Tech.*, 9, 4459–4470, doi:10.5194/amt-9-4459-2016, 2016.

Delahaye, T., S. E. Maxwell, Z. D. Reed, H. Lin, J. T. Hodges, K. Sung, V. M. Devi, T. Warneke, P. Spietz, and H. Tran: Precise methane absorption measurements in the 1.64 μm spectral region for the MERLIN mission, *J. Geophys. Res. Atmos.*, 121, 7360–7370, doi:10.1002/2016JD025024, 2016.

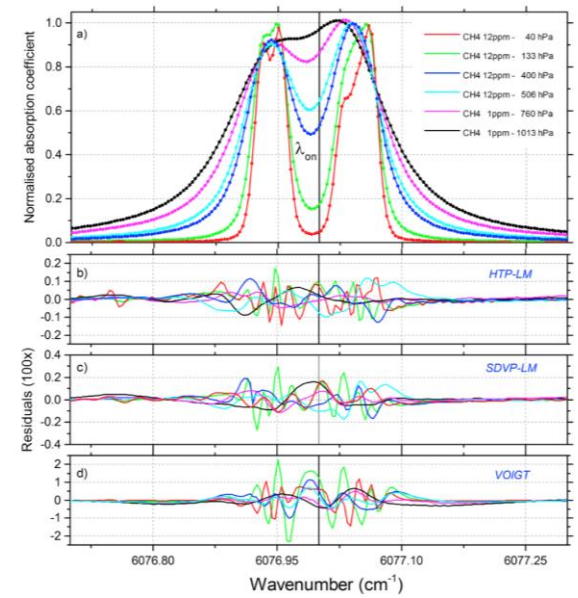


Figure 50: Multispectrum fit results of the six air-broadened spectra in the $2\nu_3 R(6) {}^{12}\text{CH}_4$ manifold region. (a) All the spectra (normalized to their peak absorption) considered: measurements are represented using dots while lines are for the modelled absorptions. (b) The fit residuals (observed minus calculated) using the first-order line-mixing HTP (expanded scale $\times 100$); (c) those obtained using the first-order line-mixing speed-dependent Voigt profile; (d) the fit residuals obtained with the VP. The wavenumber position of the MERLIN online is also indicated as a thick black line. (Source: Delahaye et al, 2016)

Outflow of formaldehyde and glyoxal from the African continent to the Atlantic Ocean

Lisa K. Behrens, Andreas Hilboll, Andreas Richter, Enno Peters, Leonardo M. A. Alvarado, Anna B. Kalisz Hedegaard, Folkard Wittrock, John P. Burrows and Mihalis Vrekoussis

In October 2016, the IUP Bremen LAMOS and DOAS groups jointly conducted the Continental Outflow of Pollutants towards the MARine Troposphere (COPMAR) project on board of the German research vessel (RV) Maria S. Merian as part of the cruise MSM58/2.

The aim of this project was to measure Formaldehyde (HCHO) and Glyoxal (CHOCHO) concentrations over the open ocean. Satellite observations frequently show enhanced values of both species over remote ocean areas, e.g., westerly from the African continent close to the Equator. However, due to the absence of local sources for these species, such enhanced values are not expected in this area, as they have only short atmospheric lifetimes of a few hours.

Thus, the measurements were conducted to validate the satellite measurements and thus confirm or contradict the presence of these species over the remote ocean areas.

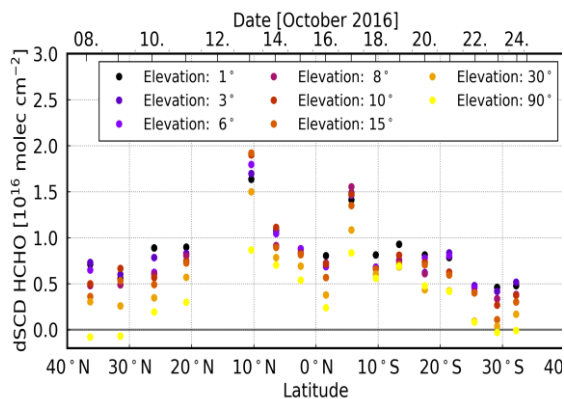


Figure 52: Latitudinal dependency of daily mean HCHO dSCDs along the cruise track. On three days (13th, 14th, and 17th), a slightly different elevation angle dependency can be observed, suggesting an elevated HCHO layer. On the 13th and 14th, similar results can be found for CHOCHO.

The cruise started in Ponta Delgada (Azores) on 8th October 2016, passed between Cape Verde and the African Continent, and ended on 25th October 2016 in Cape Town (South Africa; Figure 51). On the research vessel, a Multi-AXis Differential Absorption Spectrometer (MAX-DOAS) was installed with the telescope unit oriented perpendicularly to the heading, pointing towards the African continent. These instruments are able to take measurements at different elevation angles and azimuthal viewing directions, facilitating conclusions about both horizontal and vertical distribution of the observed species.

On three/two days during the cruise, enhanced levels of HCHO/CHOCHO respectively were observed with an elevation angle dependency different from that observed on the remaining days, indicating the presence of these gases in an elevated layer, most likely above the marine boundary layer (Figure 52). For the northern Hemisphere, these enhanced levels were found in exactly those areas where satellite observations suggest their presence (Figure 53). Also in the southern Hemisphere, clearly enhanced values of HCHO could be observed. These HCHO enhancements are not visible in the monthly

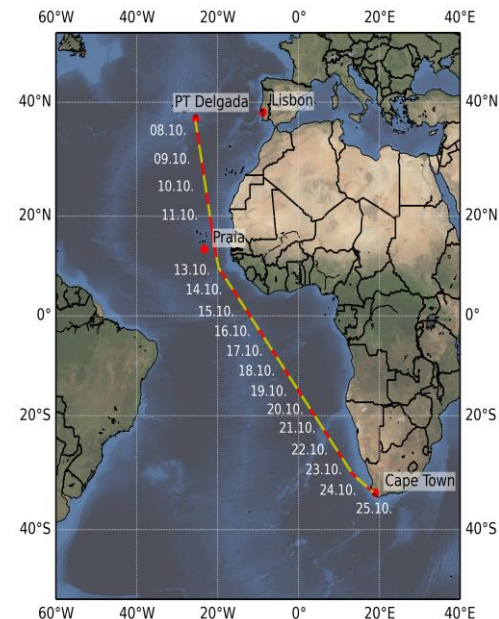


Figure 51: Cruise track of MSM58/2. The times when the instrument was measuring are marked in yellow.

averaged satellite and model data, suggesting an isolated outflow event on that specific day. Generally, the HCHO MAX-DOAS data are higher than the satellite and model data, whereas for CHOCHO, it is the other way around.

Backward simulations using the FLEXPART Lagrangian particle dispersion model suggest that the observed air masses were transported up to four days following contact with the surface (Figure 54, exemplarily shown for one day). The simulations put these air masses in altitudes between 1 and 5 km, depending on the day. They originate from the African continent which provides biogenic and biomass burning sources. These sources emit HCHO, CHOCHO, or their precursors. Because of the short lifetime of the HCHO and CHOCHO (only a few hours), precursors of these species or aerosol-gas combination have to be transported over such long distances.

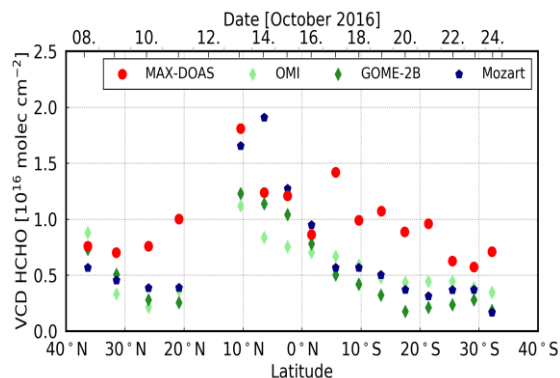


Figure 53: Latitudinal dependency of daily mean HCHO VCDs along the cruise for MAX-DOAS, OMI satellite measurements (monthly mean), and model data (monthly mean). Correlation coefficients between the datasets are all above 0.70. Similar results can be observed for CHOCHO although the correlation is slightly lower.

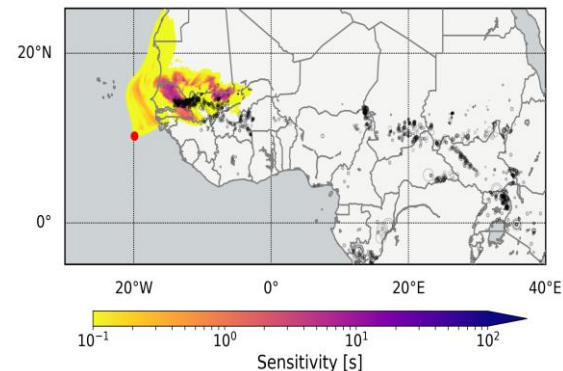


Figure 54: The emission sensitivity response function in the lowest 500m layer for particles arriving in the receptor positioned at different altitudes above the RV Maria S. Merian on the 13th October 2016, calculated with FLEXPART. The red dot indicates the ship's mid-day position. The emission sensitivities were integrated over 2 days backward, starting 2.5 km above the ship. The black circles are fires which were detected between 10th and 12th October, taken from the FINN database.

References

Behrens, L.K., Hilboll, A., Peters, E., Richter, A., Alvarado, L.M.A., Wittrock, F., Burrows, J.P., Vrekoussis, M.: MAXDOAS measurements of African continental pollution outflow over the Atlantic Ocean, DPG Spring Meeting, Erlangen, Germany, March 2018.

Behrens, L. K., Hilboll, A., Richter, A., Peters, E., Alvarado, Leonardo M. A., Kalisz Hedegaard, A. B., Wittrock, F., Burrows, J. P., and Vrekoussis, M.: Detection of outflow of Formaldehyde and Glyoxal from the African continent to the Atlantic Ocean with a MAX-DOAS instrument, *Atmos. Chem. Phys. Discuss.*, 2019:1–32, doi:10.5194/acp-2018-1286, in review, 2019.

Vrekoussis, M., Wittrock, F., Richter, A., and Burrows, J.P.: GOME-2 observations of oxygenated VOCs: What can we learn from the ratio glyoxal to formaldehyde on a global scale? *Atmos. Chem. Phys.*, 10(21):10145–10160, 2010.

Air quality simulation over the Netherlands at high spatial resolution

Andreas Hilboll and Mihalis Vrekoussis

Air pollution is a major concern for human health and, more generally, well-being. In industrialized countries, anthropogenic emissions of air pollutants are usually the largest contributor to reduced air quality. Being able to accurately simulate the transport and transformation of air pollution is highly relevant because it allows to estimate the impact of different future changes to anthropogenic emissions, which can be controlled by legislation. Another application of air quality modelling is so-called chemical weather forecasts, i.e., the prediction of air pollutant concentrations for the next days. Especially in highly polluted places, such air quality forecasts can be an important tool to improve human well-being.

Given the high spatial variability of pollutant emissions and the non-linear nature of their chemical transformation, it is important to use high spatial resolution, if one aims to capture local effects. The Weather Research and Forecast model with Chemistry (WRF-Chem) is able to perform such simulations using several nested modelling domains. In a case study, we use three such nested domains of 15x15, 3x3, and 1x1 km² horizontal resolution to simulate the dispersion and transformation of air pollutants over the Netherlands in late summer 2016. For this period, anthropogenic emission estimates at matching horizontal resolution of 1 km² are available, and the simulated pollutant concentrations can be compared with the numerous measurements taken during the 2nd Cabauw Intercomparison of Nitrogen Dioxide Measuring Instruments (CINDI-2, <http://www.tropomi.eu/data-products/cindi-2>).

Using individual seasonal, weekly, and diurnal cycles for each of the different anthropogenic source sectors, the chemical reaction scheme from the Common Representative Intermediate Mechanism

11 Sep 2016 00:00

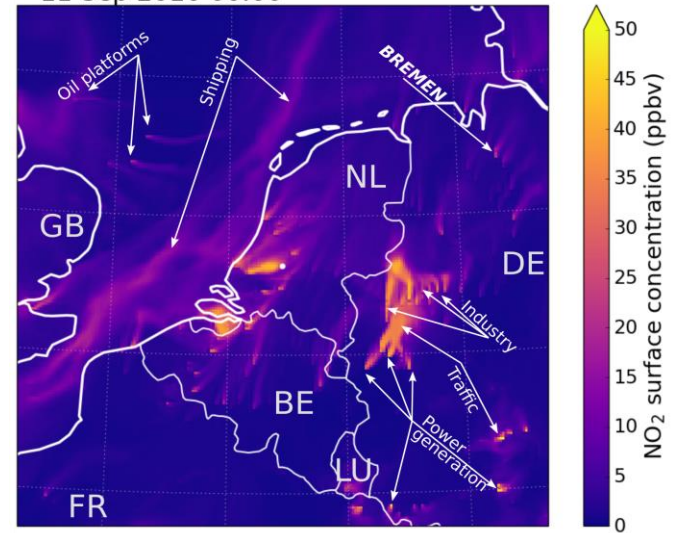


Figure 57: Simulated NO₂ surface concentrations on 11 September 2016, 00:00 UTC. Individual pollution sources are clearly visible.

(CRI mech), and the Model for Simulating Aerosol Interactions and Chemistry (MOSAIC), concentrations of the most common air pollutants like ozone, nitrogen dioxide, and formaldehyde were simulated. Figure 57 shows surface concentrations of NO₂, simulated in the intermediate modelling domain (3x3 km₂) at night-time. Due to the short lifetime of NO₂, the locations of strong emitters are clearly visible in the results.

References

Hilboll, A., Lowe, D., Kuenen, J. J.P., Denier van der Gon, H., and Vrekoussis, M.: Validation of WRF-Chem air quality simulations in the Netherlands at high resolution, AGU Fall Meeting, New Orleans, USA, December 2017.

Contribution of biomass burning to the atmospheric composition of the remote Pacific as registered in Easter Island

Nikos Daskalakis, Rasmus Nüß, and Mihalis Vrekoussis
in collaboration with

Laura Gallardo Klenner (University of Chile), Maria Kanakidou (University of Crete), Zoe Fleming (University of Leicester), and Stelios Myriokefalitakis (Utrecht University)

Modelling of ozone is a difficult task, since there are no direct ozone emissions. It is a purely secondary pollutant, chemically produced in the atmosphere. The main removal processes consist of chemical transformation and dry deposition. To simulate the vertical distribution of ozone in the troposphere, we need to properly account for both precursor species amounts (CO, NO_x etc) and production/removal processes.

For this work, we used the highly documented TM4-ECPL model. TM4-ECPL is a Chemistry and Transport Model (CTM) with an analytical chemical scheme consisting of ~280 reactions involving 120 tracers. The model is driven by the ERA-Interim reanalysis meteorology from ECMWF and uses a variety of emissions covering all different sources (anthropogenic, biomass burning, biogenic, marine and soil).

Here we compare the simulated TM4-ECPL ozone concentrations over the Easter Island (Rapa Nui) to the collocated time series of ozonesondes. Easter Island is chosen as a representative background site of the Southern Pacific region, making such a comparison extremely important for the understanding of the modelled processes. Such a remote location has minimal local anthropogenic impact on ozone precursor levels. This is supported by back trajectories of the region,

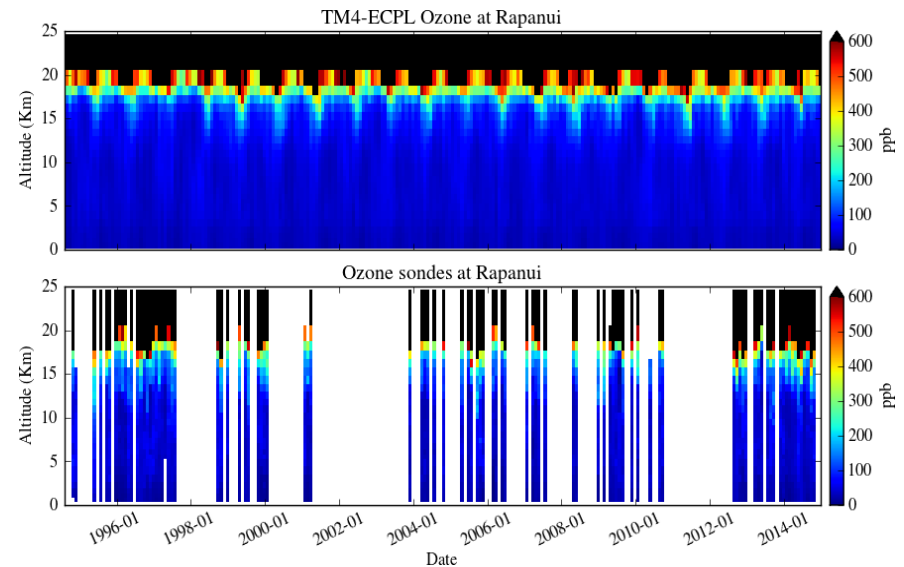


Figure 58: Simulated (top) and measured (bottom) ozone vertical profiles over Rapa Nui (Easter Island) for the years 1995–2014.

which show that the air masses reaching the island come mainly from the west, being influenced mostly by the vast ocean.

The model-measurements comparison revealed that the model simulates correctly the seasonality of ozone levels. However, at the same time the comparison also pointed to the model's inability to simulate the tropopause height (see Figure 58). The model simulates a higher tropopause, thereby affecting the mixing of the atmosphere. It manages to capture stratospheric ozone intrusions events that we see from the measurements with higher ozone values well below the tropopause, down to almost 10 km altitude (13 km altitude in the model). To further explain the ozone levels, the impact of long-range transport, wildfires and the El Niño-Southern Oscillation (ENSO) needs to be addressed.

References

Daskalakis, N., Tsigaridis, K., Myriokefalitakis, S., Fanourgakis, G. S., and Kanakidou, M.: Large gain in air quality compared to an alternative anthropogenic emissions scenario, *Atmos. Chem. Phys.*, 16, 9771-9784, <https://doi.org/10.5194/acp-16-9771-2016>, 2016.

Daskalakis, N., Kanakidou, M., Myriokefalitakis, S., Gallardo L., Vrekoussis, M. and Nüß, J.R.: Interannual assessment of ozone vertical distribution: A modeling study. AGU Fall Meeting, Washington D.C., U.S.A., December 2018.

Daskalakis, N., Kanakidou, M., Myriokefalitakis, S., Gallardo Klenner, L., Nüß, J.R., and Vrekoussis, M.: Ozone trend analysis from 1980–2015: Models vs observations. IGAC Science Conference, Takamatsu, Japan, September 2018.

Gallardo Klenner, L., Henríquez, A., Thompson, A.M., Rondanelli, R., Carrasco, J., Orfanos-Cheuquelaf, A., and Velásquez, P.: The first twenty years (1994–2014) of ozone soundings from Rapa Nui (27°S, 109°W, 51 m a.s.l.), *Tellus B: Chemical and Physical Meteorology*, 68:1, DOI: 10.3402/tellusb.v68.29484, 2016.

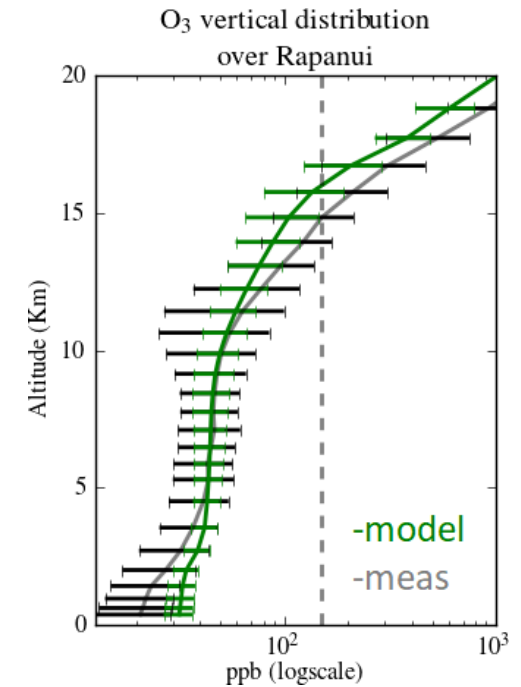


Figure 59: Simulated (green) vs. measured (gray) average vertical profiles of ozone concentrations.

Transport climatology of black carbon emissions from European megacities

Anna B. Kalisz-Hedegaard, Andreas Hilboll and Mihalis Vrekoussis

Black carbon (BC) is a component of particulate matter, consisting of pure carbon in several linked forms. It is formed by incomplete combustion of both fossil fuels and biomass and is thus a product of both anthropogenic and natural processes. Black carbon plays a significant role as a positive radiative forcer and notably impacts human health and well-being.

During the past decades, human economic activity and thus combustion of fossil fuels has continued to experience large growth rates. At the same time, more and more of this economic activity is concentrated in large urban agglomerations. It is therefore interesting and important to evaluate the impact of these large urban agglomerations on air quality, and how it has changed over the past decades.

To answer this question, the offline Lagrangian transport and dispersion model FLEXPART is applied to describe the climatological dispersion characteristics of black carbon emissions from major population centres (MPCs) in the Northern Hemisphere for the period 1980-2018. The modelled black carbon is subject to removal processes by dry and wet deposition. The simulations are forced by the ECMWF ERA-Interim meteorological reanalysis and the emission strengths are taken from the MACCity inventory.

Using these simulations, the impact of the emissions from selected urban agglomerations on air pollution levels at local, regional, and hemispheric scales can be evaluated. Emissions are treated on a monthly basis, to identify seasonal differences in the dispersion patterns. In most cases, there is a clear difference during different parts of the year.

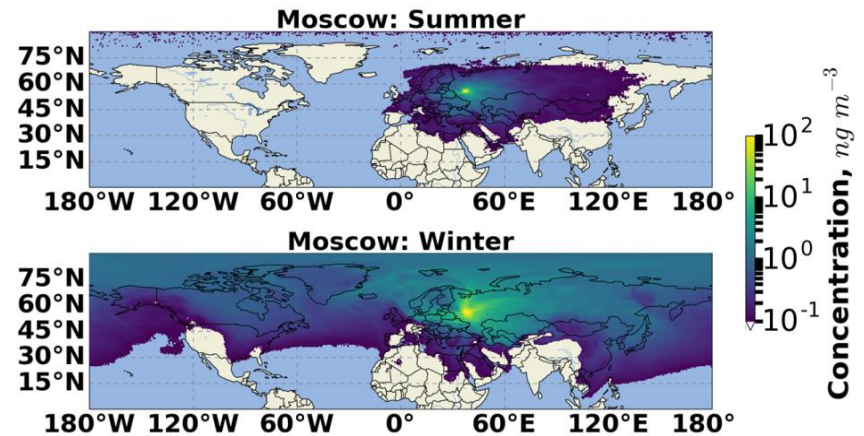


Figure 60: Simulated surface concentrations of black carbon emissions from Moscow for summer 2014 (top) and winter 2014 (bottom).

For example, the black carbon emissions from Moscow during winter spread to continental scales, whereas in spring and summer, the impact covers only a relatively small region (Figure 60). This difference is caused both by seasonal patterns in predominant wind directions and precipitation patterns, and by the generally lower emissions in summer time.

Using this multi-decade dataset, it is now possible to address questions like the decadal changes in the health impact of individual major population centres and individual source sectors, or the impact of individual MPCs on black carbon deposition on Arctic sea ice.

References

- Kalsiz Hedegaard, A. B., Hilboll, A., Schlager, H., and Vrekoussis, M.: Climatological Impact of Black Carbon Transport from European Major Population Centers, IGAC Science Conference, Takamatsu, Japan, September 2018.
- Kalsiz Hedegaard, A. B., Hilboll, A., Schlager, H., and Vrekoussis, M.: Climatological Impact of Black Carbon Transport from European Major Population Centers on the Arctic, (AC)³ Science Conference on Arctic Amplification, Bremerhaven, Germany, November 2018.

Introduction to new IUP department on climate modelling

Veronika Eyring, Bettina K. Gier and Katja Weigel

In July 2017, a new IUP department on *Climate Modelling* was established under the lead of Prof. Veronika Eyring. In collaboration with the department on *Earth System Model Evaluation and Analysis* of the German Aerospace Center's Institute of Atmospheric Physics (DLR-IPA), the new department focuses on analysing Earth system model (ESM) simulations in combination with observations to better understand and project the climate system and anthropogenic climate change. The evaluation of ESMs with observations is crucial for an improved process understanding of the climate system and is also a vital prerequisite for more trustworthy climate projections of the 21st century needed as basis for guidelines in climate policy.

The department provides major contributions to the Coupled Model Intercomparison Project (CMIP), currently in its 6th phase (CMIP6, Eyring et al., 2016a), by contributing to the development of the Earth System Model Evaluation Tool (ESMValTool, Eyring et al., 2016b) and by running the tool on model output submitted to the CMIP archive for a more systematic, open and rapid performance assessment of the large and diverse number of models (Eyring et al., 2016c). This will also expose whether long-standing model errors remain evident in newer models and will assist modelling groups in improving their models.

One focus of the department's work is to develop emergent constraints with the goal to narrow uncertainties in key climate feedbacks and in climate projections with observations. Emergent constraints are relationships across an ensemble of models between an unobservable Earth system sensitivity and an observable trend or variation in the contemporary climate (Wenzel et al., 2016). As an example towards the development of emergent constraints for the carbon cycle, Figure 61 shows the mean seasonal cycle amplitude of column-averaged dry-

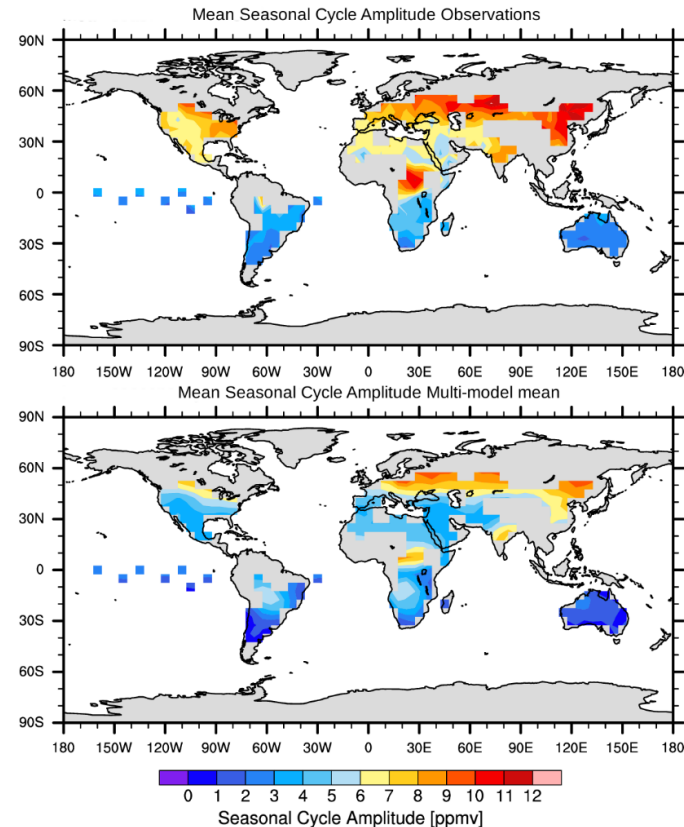


Figure 61: Map of the XCO₂ seasonal cycle amplitude [ppmv] from satellite observations (upper panel) and the multi-model mean sampled as the observation data (lower panel).

air mole fraction of CO₂ (XCO₂) for satellite observations and the multi-model mean calculated from 10 ESMs participating in the CMIP Phase 5 (CMIP5) for the years 2003-2016. The models are sampled the same way as the observations. The observations (Buchwitz et al., 2018) combine measurements of SCIAMACHY (SCanning Imaging Absorption Spectrometer for Atmospheric CHartography) on Envisat and TANSO-

FTS (Thermal And Near infrared Sensor for carbon Observation - Fourier Transform Spectrometer) on GOSAT (Greenhouse gases Observing SATellite). The seasonal cycle amplitude is defined as the peak-to-trough amplitude in a calendar year of the detrended time series. Both models and observations show characteristic seasonal cycles in CO₂, with lower values in the summer when strong photosynthesis causes plants to absorb CO₂, and higher values in the winter when photosynthesis stops. The peak-to-trough amplitude of the seasonal cycle therefore depends on the strength of the summer photosynthesis and the duration of the growing season and is larger in the Northern than in the Southern Hemisphere. A study in the journal Nature shows that doubling of the CO₂ concentration in the atmosphere will cause global plant photosynthesis to further increase by approximately one third (Wenzel et al., 2016).

In Figure 62, following Schneising et al. (2014), the influence of the growing season temperature anomaly on the seasonal cycle amplitude for the northern mid-latitudes (30-60°N) is shown for the observations and the multi-model mean. The growing season temperature anomaly is defined as the temperature anomaly with respect to the monthly climatology averaged over the growing season (April to September for the Northern Hemisphere). Only vegetated areas are used, identified by the MODIS (MODerate resolution Imaging Spectroradiometer) Land Cover Classification. The multi-model mean is able to reproduce the observed correlation and negative trend of the seasonal cycle amplitude with increasing growing season temperature.

The data are analysed as part of the Advanced Earth System Model Evaluation for CMIP (EVal4CMIP) project funded by the Helmholtz Society. All data are processed and combined using the ESMValTool (Eyring et al., 2016b), an open-source community-developed diagnostics and performance metrics tool for the systematic evaluation of ESMs with observations.

The *Climate Modelling* department maintains close collaboration in particular with the *Greenhouse Gas Group* at IUP as well as with the

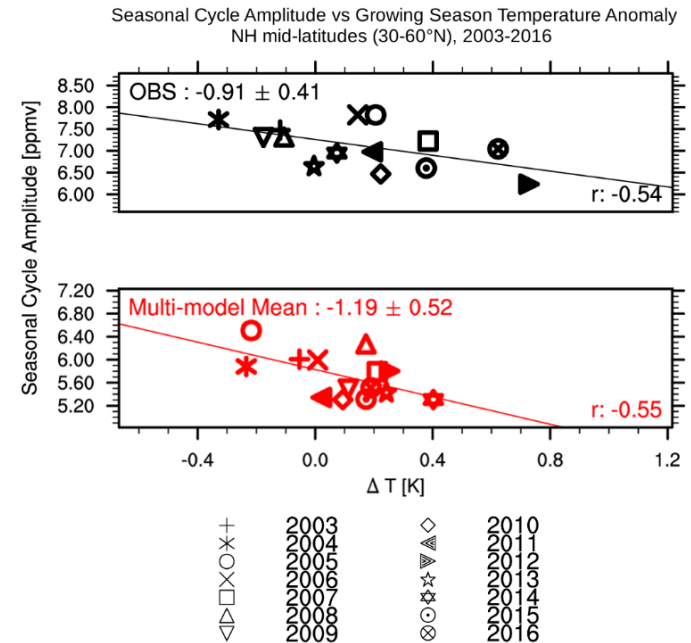


Figure 62: Seasonal cycle amplitude of XCO₂ [ppmv] versus the growing season temperature [K] for the years 2003 to 2016 for satellite observations (upper panel) and their multi-model mean (lower panel) in the Northern mid-latitudes.

Climate Informatics Group of the DLR Institute of Data Sciences and its external collaboration partners from the Friedrich-Schiller-University and the Max-Planck-Institute for Biogeochemistry in Jena. It is strongly linked to international research activities within the World Climate Research Programme (WCRP) and contributes to international climate assessments of the Intergovernmental Panel on Climate Change (IPCC).

References

Buchwitz, M., Reuter, M., Schneising, O., Noël, S., Gier, B., Bovensmann, H., Burrows, J.P., Boesch, H., Anand, J., Parker, R.J., Somkuti, P., Detmers, R.G., Hasekamp, O.P., Aben, I., Butz, A., Kuze, A., Suto, H., Yoshida, Y., Crosp, D., O'Dell, C.: Computation and analysis of atmospheric carbon dioxide annual mean growth rates from satellite observations during 2003-2016, *Atmos. Chem. Phys.*, 18, 17355-17370, <https://doi.org/10.5194/acp-18-17355-2018>, 2018.

Eyring, V., Bony, S., Meehl, G. A., Senior, C. A., Stevens, B., Stouffer, R. J., and Taylor, K. E.: Overview of the Coupled Model Intercomparison Project Phase 6 (CMIP6) experimental design and organization, *Geosci. Model Dev.*, 9, 1937-1958, doi:10.5194/gmd-9-1937-2016, 2016a.

Eyring, V., Righi, M., Lauer, A., Ewaldsson, M., Wenzel, S., Jones, C., Anav, A., Andrews, O., Cionni, I., Davin, E. L., Deser, C., Ehbrecht, C., Friedlingstein, P., Gleckler, P., Gottschaldt, K.-D., Hagemann, S., Juckes, M., Kindermann, S., Krasting, J., Kunert, D., Levine, R., Loew, A., Mäkelä, J., Martin, G., Mason, E., Phillips, A. S., Read, S., Rio, C., Roehrig, R., Senftleben, D., Sterl, A., van Ulft, L. H., Walton, J., Wang, S., and Williams, K. D.: ESMValTool (v1.0) – a community diagnostic and performance metrics tool for routine evaluation of Earth system models in CMIP, *Geosci. Model Dev.*, 9, 1747-1802, doi:10.5194/gmd-9-1747-2016, 2016b.

Eyring, V., Gleckler, P. J., Heinze, C., Stouffer, R. J., Taylor, K. E., Balaji, V., Guillard, E., Joussaume, S., Kindermann, S., Lawrence, B. N., Meehl, G. A., Righi,

M., and Williams, D. N.: Towards improved and more routine Earth system model evaluation in CMIP, *Earth Syst. Dynam.*, 7, 813-830, doi:10.5194/esd-7-813-2016, 2016c.

Schneising, O., Reuter, M., Buchwitz, M., Heymann, J., Bovensmann, H., and Burrows, J. P.: Terrestrial carbon sink observed from space: variation of growth rates and seasonal cycle amplitudes in response to interannual surface temperature variability, *Atmospheric Chemistry and Physics*, 14(1), 133-141, doi:10.5194/acp-14-133-2014, 2014.

Wenzel, S., Cox, P. M., Eyring, V., and Friedlingstein, P.: Projected land photosynthesis constrained by changes in the seasonal cycle of atmospheric CO₂, *Nature*, doi: 10.1038/nature19772, 2016.

Links

[ESMValTool: http://www.esmvaltool.org/](http://www.esmvaltool.org/)

CMIP video: (shorter version): <https://youtu.be/wTBkq9nWNEE>

CMIP6 video (longer version): <https://youtu.be/WdRiYPJLt4o>

WCRP website News: <https://www.wcrp-climate.org/wgcm-cmip/cmip-video>

EGU Highlight Article: <http://www.egu.eu/news/highlight-articles/586/wcrps-coupled-model-intercomparison-project-a-remarkable-contribution-to-climate-science/>

How well is the North Atlantic circulation simulated in models?

Tilia Breckenfelder, Monika Rhein, Achim Roessler and Christian Mertens

The North Atlantic Current (NAC) transports warm and saline water from the subtropical Atlantic to the high latitudes, and thereby significantly influences the climate and sea level in western and northern Europe. Despite its importance, continuous observations of the strength of that circulation are only available on some locations, and none of those time series is longer than 25 years. This is much too short to analyse variability on multiannual to decadal time scales and their linkage to the atmosphere and climate. These topics have to be studied with models, but for that they need to simulate a realistic circulation.

To find out whether this is the case, observed transport time series in the subpolar North Atlantic are compared with the modelled circulation (Breckenfelder et al., 2017), and this was a joint effort of the observational group at the IUP and the model group of C. Böning at GEOMAR, Kiel.

The simulated NAC transport across the Mid-Atlantic Ridge from the western into the eastern Atlantic (27 Sv) was only slightly lower than observed, but the NAC pathways were shifted further northward. In the eastern Atlantic, the western branch of the NAC carries the bulk of the transport, while episodic observations point to a preference of the eastern branch. In short, the model is able to simulate the

main features of the flow, giving confidence to analyse multiannual and their linkages to

atmospheric modes in the model. It turned out that the modelled NAC transports were significantly larger during high NAO phases (+6.7 Sv) by mainly enhancing the transport of the eastern NAC branch.

This research is part of the BMBF funded program **RACE** (Regional Atlantic Circulation and Global Change).

Reference:

Breckenfelder, T., M. Rhein, A. Roessler, C. W. Böning, A. Biastoch, E. Behrens, and C. Mertens: Flow paths and variability of the North Atlantic Current: A comparison of observations and a high-resolution model. *J. Geophys. Res.*, 122, 2686-2708, doi:10.1002/2016JC012444, 2017.

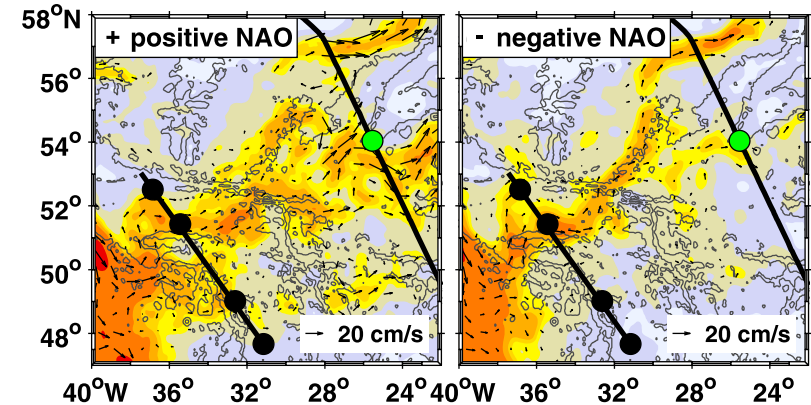


Figure 63: Modelled integrated flow field, 0-1000m depth for time periods with high positive NAO (left) and high negative NAO (right). From Breckenfelder et al., 2017

Where is the Greenland melt water?

Monika Rhein, Reiner Steinfeldt, Oliver Huhn and Tilia Breckenfelder

Global warming will lead to significant changes in the Atlantic circulation, with enormous impact on the European climate and the sea level in Europe and North America in the next decades. However, the projected changes in the circulation are still uncertain. When we continue to burn fossil fuels as we do now, the AMOC is thought to decline till 2100 by 10 % to 50 %, depending on the climate model. One open question is the response of the large-scale Atlantic circulation to increasing Greenland melt. Greenland's mass loss has quadrupled over the last two decades, by surface melt and by contact of the warm water of subtropical origin with glaciers terminating in the ocean fjords. When the additional freshwater invades the central Labrador Sea that links the northward subtropical warm water with the southward transport of cold water in the abyss, then this link could be weakened or interrupted leading to a decline in the northward warm water transport. While in typical climate models the Greenland melt water reaches the key region quickly, it takes much longer in a high resolution ocean-ice model, where most of the freshwater first sticks to the Greenland boundary current and only part makes it into the central Labrador Sea.

What about observations? In the presence of various freshwater sources and saline water masses, salinity measurements alone are not sufficient to identify Greenland melt, and other parameters are needed. The noble gases helium and neon are trapped in air bubbles in the ice, and when ice

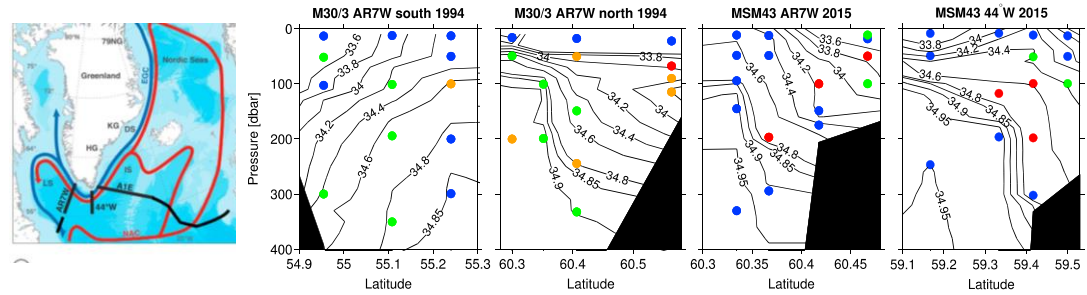


Figure 64: Distribution of SMW fraction (%) in the upper 400 m at the Greenland and Canadian Shelf (location see map). Blue: SMW not detected, dark red: >0.23%, green between 0.075% and 0.2%. From Rhein et al., 2018.

melts below the mixed layer, these noble gases are dissolved in ocean water. By measuring the distribution of He and Ne, fractions of submarine Greenland meltwater (SMW) down to less than 1 per mill are identified. We used this method for the first time to quantify the distribution of Greenland melt. SMW fractions >0.2% (maximum 0.62%) are confined in the upper 400 m of the Greenland and Canadian boundary current, but is not detectable in the central Labrador Sea yet. Occasionally, He and Ne signals are also found in the deep water masses, but they enter the abyss by a different process. We hypothesize that SMW bearing water leaves the Greenland shelf in the northern Irminger Sea with the so-called East Greenland Current spill jets.

This research is part of the BMBF funded program **RACE** (Regional Atlantic Circulation and Global Change) and of the DFG funded priority program **SPP 1889** Regional Sea Level and Society

Reference:

Rhein, M., Steinfeldt, R., Huhn, O., Sültenfuss, J., and Breckenfelder, T.: Greenland submarine melt water observed in the Labrador and Irminger Sea. *Geophysical Research Letters*, 45, 10,570–10,578. <https://doi.org/10.1029/2018GL079110>, 2018.

Internal waves generated by remote tropical cyclones

Janna Köhler, Georg S. Völker and Maren Walter

Internal waves radiate energy and momentum horizontally and vertically through the interior of the ocean, thereby changing the density field as they distort (i.e. vertically displace) the background density interfaces. These vertical displacements can reach up to some hundred meters, depending on the internal wave energy and the local stratification whereas horizontal scales of internal waves range in the order of 100 –1000m. They span the frequency range from the local Coriolis frequency f to the buoyancy frequency N that is set by the stratification (Figure 65). Internal waves have a variety of energy sources and generation processes. Major generation mechanisms are e.g. the interaction of the barotropic tides with the seafloor topography inducing internal waves with tidal frequencies or large scale currents interacting with the seafloor topography. A fluctuating wind stress at the ocean surface induces downward propagating low frequency, near inertial (near the Coriolis frequency f) internal waves. This can induce a seasonal cycle in near-inertial internal wave energy that is largely in phase with storm intensity. Once the internal waves are generated, they undergo a multitude of propagation and interaction processes which induce a propagation of energy towards smaller scales until the internal waves finally break and cause diapycnal mixing and energy dissipation.

To address the question of how far hurricane-generated near-inertial waves propagate before their energy is dissipated, we studied the temporal variability of near-inertial internal wave energy south of the main hurricane track. For this we used a 5-yr mooring time series in the interior of the tropical North Atlantic at 16°N. The distinctly calm oceanographic and meteorological conditions in the mooring area are characterized by weak and constant trade winds. This allows the clear identification of near-inertial waves that were

remotely generated by hurricanes and propagate southward towards the mooring area.

During all deployment periods, hurricanes passed over or to the North of the mooring, with the strongest winds occurring in 2003 and 2004 (Figure 66). In the 2003 hurricane season, two very strong hurricanes (Isabel and Fabian) passed over the tropical Atlantic within several days of each other (Figure 67 panel a). With a time lag of approximately 2 to 3 weeks after the passage of the two hurricanes, an increase in depth-mean near-inertial energy by a factor of 3.8 is observed in the mooring area (Figure 67 panel b). Weaker hurricanes in 2001, 2002, and 2004 correspond to smaller increases in energy (factors of 1.1, 1.8, and 2.4 times the background, respectively). It was shown that near-inertial waves with frequencies corresponding to generation sites of up to approximately 1000 km north of the mooring contribute to the amplifications in 2003 and 2004 (Figure 67 panel c).

The energy flux measured at the mooring location during the strongest hurricanes in 2003, shows a matching strong (up to 5 kW m^{-1}) southward energy flux from mid-September to mid-

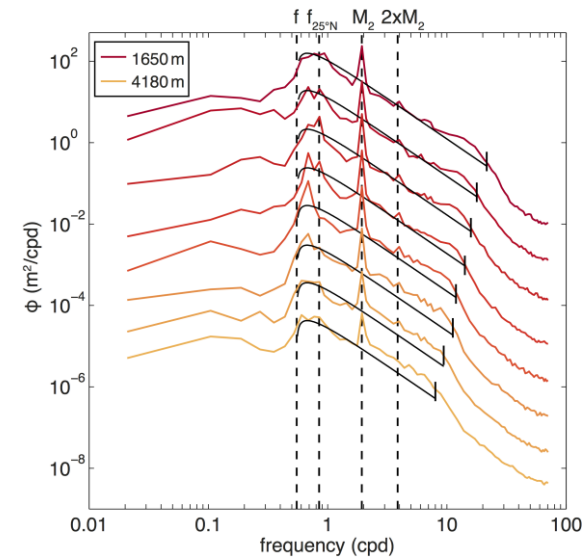


Figure 65: Mean spectra of vertical displacements of isopycnals during the fourth deployment period with corresponding Garrett Munk spectra (black). Vertical black dashed lines denote the inertial frequency at the mooring site (f), at 25°N ($f_{25^\circ N}$), the M_2 tidal frequency, and $2M_2$, respectively. The small vertical black bars show the buoyancy frequency at the individual depths. Spectra have been vertically offset by 10^{-1} for clarity (with zero offset for the uppermost instrument).

October 2003. During the rest of the year, only a weak flux lacking a dominant direction is observed, making the hurricane-induced energy flux the dominating contribution to the time-integrated horizontal energy flux over the entire year. In the zonal flux component, individual flux estimates are enhanced during September and October, but as no direction prevails, the time-integrated en-

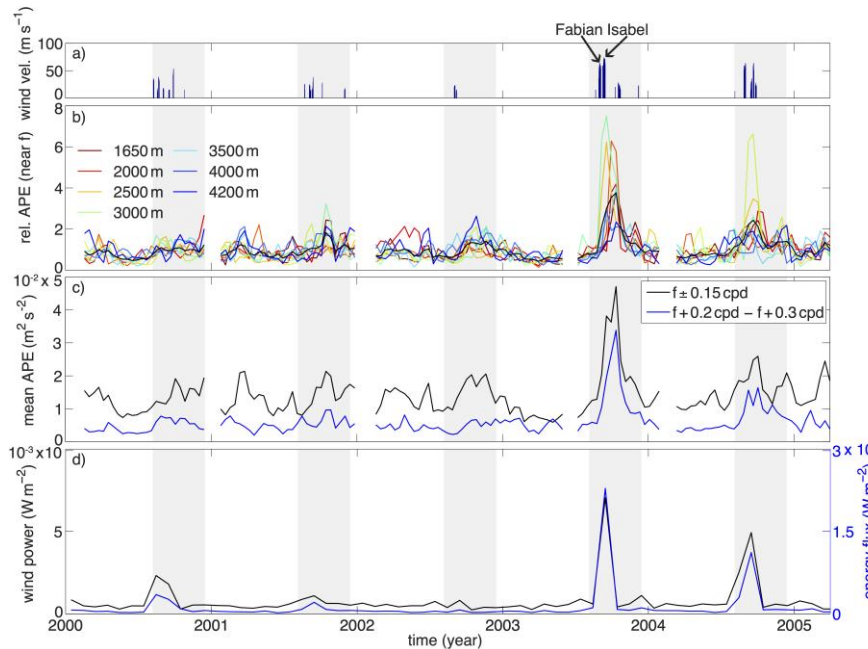


Figure 67: Wind speeds of hurricanes at times when they pass the area $15^{\circ}\text{N} < \text{lat} < 25^{\circ}\text{N}$ and $45^{\circ}\text{W} < \text{lon} < 70^{\circ}\text{W}$ (data from HURDAT2). (b) Time series of near-inertial ($f - 0.15$ to $f + 0.3$ cpd) energy divided by its mean over the entire 5 years at the individual depths along with the mean (over depth) value (black). (c) Mean (over depth) of potential energy in the frequency ranges $f \pm 0.15$ cpd (black) and $f + 0.2$ to $f + 0.3$ cpd (blue). (d) Energy flux (normalized by area) from the wind field into the mixed layer (blue) and into the internal wave field (black) from the extended slab model in the area $15^{\circ}\text{--}25^{\circ}\text{N}$, $45^{\circ}\text{--}70^{\circ}\text{W}$.

ergy flux is much lower than in the meridional component (approx. 1×10^9 to $5 \times 10^9 \text{ J m}^{-1}$).

For a qualitative comparison, the energy imparted to the internal gravity wave field by the wind was estimated using an extended slab model. With the exception of hurricanes, the wind-induced inertial energy flux into the internal wave field has little variability around an average value below $4 \times 10^{-5} \text{ W m}^{-2}$ (Figure 67 panel d). Compared to other regions, this is relatively small and reflects the generally calm weather regime at the mooring location. Superimposed on these background conditions are sporadic peaks (up to at least 5 times higher than background) in the energy fluxes into the internal gravity wave field, which can be linked to the strong winds of passing hurricanes. These peaks precede observed increases in the APE at the mooring location by approximately 1 month. This also suggests that the internal gravity waves associated with the increase in APE are not generated on site, but at some distance, and propagate toward the mooring location.

These results show that hurricanes centred up to several hundred kilometres north of the mooring are the dominant energy source of near-inertial waves in the central part of the western tropical Atlantic and thus contribute to the energy available for diapycnal mixing in regions far to the South of the storm track.

References

Köhler, J., G. S. Völker, and M. Walter: Response of the internal wave field to remote wind forcing by tropical cyclones. *J. Phys. Oceanogr.*, 48(2), 317-328, 2018.

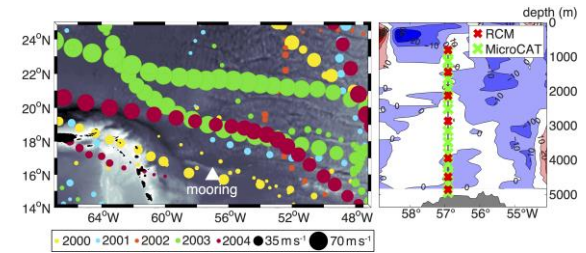


Figure 66: Location of the central mooring of the MOVE array along with hurricane tracks (from the Atlantic hurricane database, HURDAT2) during 2000-2004 (left). Distribution of temperature and conductivity sensors and current meters (RCMs) shown as an example for the deployment period 2003-04 with current measurements from a cruise in June 2000 in the background (right).

Basal melt and freezing rates from first noble gas samples beneath an ice shelf

Oliver Huhn, Monika Rhein and Jürgen Sültenfuß

In austral summer 2015/16 and 2016/17 we obtained with a new constructed gas-tight in-situ water sampler the worldwide first noble-gas samples from below an ice shelf, the Filchner Ice Shelf in the southern Weddell Sea, Antarctica (Huhn et al., 2018).

Quantifying the amount of glacial meltwater (GMW) that is released from the large floating ice shelves surrounding Antarctica into the ocean is crucial to understand the complex ocean-ice shelf interaction under warming climate conditions. Direct observations of basal melt rates are rare, due to the remote and hardly accessible areas. The Filchner-Ronne Ice Shelf (FRIS) is the largest by volume in Antarctica, and models suggest an accelerated basal melting to the end of this century. However, actual estimates of its basal melt rate are usually based on indirect methods, i.e. model simulations and remote sensing techniques.

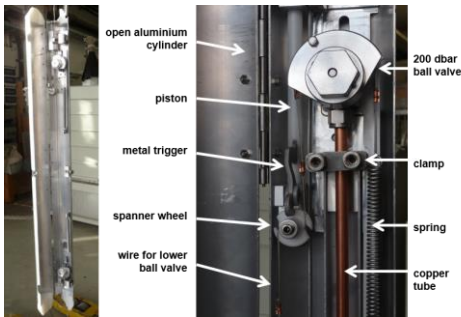


Figure 69: In-situ sub-ice-shelf water sampler. Left: photo of the entire in-situ water sampler in the machine shop. Right: details of the upper closing mechanism inside the in-situ water sampler showing red release piston, metal trigger, spanner wheel, spring, and valve with connected copper tube.

When the meteoric ice melts at the base of an ice shelf, the enhanced hydrostatic

The stable noble gases helium and neon are useful tracers to quantify GMW. They are weakly soluble in seawater, and therefore are present in low concentrations. But glacial ice traps atmospheric air. When the meteoric ice melts at the base of an ice shelf, the enhanced hydrostatic

pressure at several hundred meter depth causes the trapped noble gasses to dissolve fully in the water. This leads to a He excess of 1280% and a Ne excess of 890% in pure GMW. This large excess provides an excellent tool to detect and quantify GMW fractions as low as 0.05%.

To quantify the fraction and the spatial distribution of GMW below the Filchner Ice Shelf (FIS), we collected the first sub-ice shelf helium and neon samples from six boreholes (Figure 68) located on FIS, hot-water drilled by a team from the British Antarctic Survey (BAS) and the Alfred-Wegener-Institute (AWI) in the framework of the "Filchner Ice Shelf Project" (FISP) and the "Filchner Ice Shelf System" (FISS).

To obtain noble gas samples from the water column below an ice shelf, we have constructed a new gas-tight in-situ water sampler. The major challenge was to protect the water samples from the sub-glacial cavity from gas-fractionation and degassing due to freezing and expansion while the sample is recovered through the

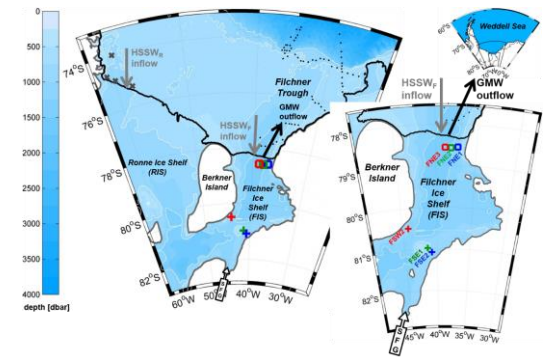


Figure 68: Map of the FRIS showing ice drill sites with noble gas data. Bold black line: ice shelf front, thick grey line: approximate grounding line. Blue shading: isobaths in 250 m steps, thin white lines: 500 m and 1000 m isobaths. Berkner Island separates Ronne Ice Shelf (RIS) to the west from FIS. In the southeast, Support Force Glacier (SFG) drains into FIS. Red, green, and blue crosses are the locations of the southern sites with noble gas data from 2015/16. Red, green, and blue squares are the northern sites from 2016/17. Black dots north of FIS are noble gas stations from 2014, grey crosses in front of RIS are noble gas stations from 1995. Grey and black arrows indicate the inflow of High Salinity Shelf Water (HSSW, subscript F and R denoting FIS and RIS inflow) and the outflow of glacial meltwater (GMW).

air-filled portion of the up to 800 m long and 25 cm narrow bore-hole at -20°C.

The instrument (Figure 69) contains a copper tube allowing a sea-water sample of ~44 g to be collected, with high pressure ball valves connected to a gas-tight connector at both ends. Additional inflow and outflow funnels extend the tube at both ends of the sampling device to increase the flux of water for flushing and rinsing the copper tube. The instrument is mounted in an aluminium

cylinder (diameter 10 cm, length 150 cm, weight 8 kg) to protect it while passing through the bore hole.

The instrument is lowered into the ice shelf cavity on a wire together with a CTD profiler continuously measuring temperature, salinity and pressure. During lowering the valves are held open with a steel spring and connecting wires. A messenger weight deployed along the wire then strikes a piston, releasing a spanner wheel held back by a metal trigger arm and closing the valves at each end of the sample tube.

Three sites at around

81°S between Berkner Island and the mainland were occupied in 2015/16, and are representative of the part of the ice shelf cavity, where inflow from the Ronne Ice Shelf (RIS) in the west determines the water column structure. Three sites around 78.5°S were sampled in 2016/17. They are located ~60 km south of the FIS ice front and could potentially be influenced by water masses formed north of the ice shelf. The FIS cavity samples are supplemented by oceanic noble gas samples in front of FIS and RIS to determine the properties of inflowing and outflowing water.

Basal meltwater fractions (Figure 70B) calculated from helium and neon (Figure 70A) range from 3.6% near the ice shelf base to 0.5% near the sea floor, with distinct regional differences. We estimate an average basal melt rate for the FRIS of 177 ± 95 Gt/year, independently confirming previous results. We calculate that up to 2.7% of the meltwater has been refrozen. Furthermore, we identified a local source of crustal ^4He (at the south-eastern-most location, fed by Support Forth Glacier), that contributes up to 13 % subglacial runoff (accumulated α -particles from the underlying bedrock into the overlaying ice stream before the glacier starts floating) to the total meltwater.

Our results provide a benchmark against which ice shelf cavity conditions in models investigating the interaction between the ocean and ice shelves can be compared.

Reference:

Huhn, O., T. Hattermann, P. E. D. Davis, E. Dunker, H. H. Hellmer, K. W. Nicholls, S. Østerhus, M. Rhein, M. Schröder, J. Sültenfuß: Basal melt and freezing rates from first noble gas samples beneath an ice shelf. *Geophysical Research Letters*, 45, doi:10.1029/2018GL079706, 2018.

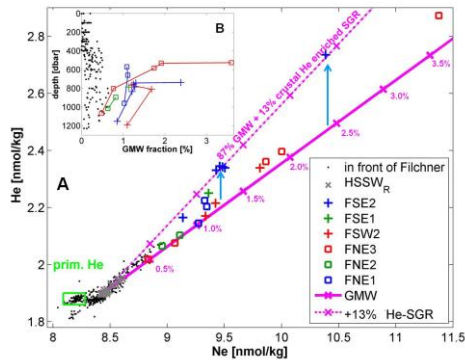


Figure 70 (A) Ne vs. He and (B) calculated GMW fractions below FIS and in front of FIS. Data colours and symbols as in the map above. A) shows the correlation between He and Ne. Solid magenta line indicates mixing of inflowing High Salinity Shelf Water into the RIS cavity and pure GMW (Ne +890 ‰; He +1280 ‰). The magenta marks on the GMW line indicate GMW fraction every 0.5%. He concentrations above the GMW mixing line indicate addition of crustal He accumulated in the ice from α -decay from the underlying bedrock. The dashed magenta line represents mixing between HSSW and a combination of 87% GMW plus 13% crustal He enriched subglacial runoff (SGR). B) shows the calculated GMW fractions based on Ne.

Temperature flux carried by individual eddies across 47°N in the Atlantic Ocean

Vasco Müller, Dagmar Kieke and Christian Mertens

The North Atlantic between 40°–55°N is influenced by two vastly different regimes of currents and water masses: the subpolar gyre, a large-scale cyclonic circulation cell, and the anticyclonic circulation cell of the subtropical gyre. In the Newfoundland Basin, the Western Boundary Current (WBC) and the North Atlantic Current (NAC), the northward continuation of the Gulf Stream, flow in different directions along the boundary of the two gyres. The deep reaching WBC originating in the north transports cold and fresh water of subpolar origin southward. The NAC, on the other hand, carries warmer and saline surface and subsurface waters of subtropical origin into the North Atlantic.

In a recent study (Müller et al., 2017) done in collaboration with scientists from the University of Alberta, Edmonton, Canada, we investigated the western subpolar North Atlantic between 45°N and 50°N, which is a highly dynamic region. On its way along the western continental margin, the Gulf Stream/NAC has to cross several topographic obstacles causing it to experience disruptions, forming meanders, and shedding individual eddies, i.e. small whirling bodies of water rotating either in clockwise or anti-clockwise direction. This creates regions of increased eddy kinetic energy (EKE) along the pathway of the NAC and in the Newfoundland Basin (Figure 71).

Over a period spanning about two decades, we identified, tracked, and analyzed these eddies while crossing the latitude of 47°N. The purpose of our study was to contribute to a better understanding of the role of individual eddies for

the spatial exchange of waters and heat and horizontal mixing of water masses from different origin and of different

properties. We centred our analysis on surface temperature fluxes of individual eddies, detected in satellite altimetry and sea surface temperature (SST) observations based on an algorithm provided by Nencioli et al. (2010). Both data sets have the advantage of high temporal and spatial coverage and thus provide a long-term time series spanning over more than two decades (1993–2014) at a high temporal and spatial resolution (1 day and 1/4°). As a comparison, the analysis was subsequently applied to the output from two Canadian model simulations with different horizontal resolution (1/4° and 1/12°).

For the eddy detection and the calculation of the respective temperature fluxes, the two independent data sets (observations and the model simulations) all showed coherent patterns. The highest numbers of eddies in the subpolar North Atlantic were detected along the pathway of the NAC and in the observations also on the Grand Banks of Newfoundland. Furthermore, the study illustrated the importance of individual eddies, carrying a notably large tem-

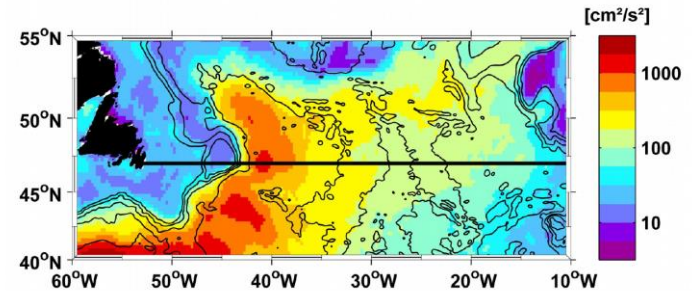


Figure 71: Mean eddy kinetic energy (EKE) relative to the annual cycle derived from geostrophic surface velocity anomalies of the years 1993 to 2014. EKE [cm^2/s^2] is shown with a logarithmic scale. Highest EKE values are typically found along the pathway of the North Atlantic Current (NAC). The black bold line denotes the 47°N section.

perature anomaly (so-called strong eddies), for the temperature flux by eddies across 47°N. About 25% of the absolute temperature flux by eddies crossing 47°N originated from these strong eddies. Strong eddies occurred most often in the Newfoundland Basin. The number of both strong and regular eddies in the region and their respective direction of translation was clearly connected to the spatial pattern and strength of the background oceanic velocity field (Figure 72). The western part of the Newfoundland Basin with the fastest and most pronounced current branches was the major pathway for eddies and their associated temperature flux across 47°N. Among the investigated eddies northward moving cold-core cyclones carrying subpolar water from the WBC made a considerable contribution to the overall temperature flux by eddies in the Newfoundland Basin.

Even though we found the largest temperature fluxes in either direction in the western boundary region, the mean flux in the western basin was practically zero, because the large northward flux (especially in the NAC region) was compensated by large southward fluxes in the Newfoundland Basin Recirculation (NBR) region around 40°W and in the WBC. The eddies, first detected in the region between WBC and NAC, provided a means for the local exchange between the boundary and the interior of the North Atlantic. Contrary to the western basin, the eastern basin of the North Atlantic showed a rather low temperature flux carried by eddies across 47°N, the main reason being the NAC running mainly in a zonal direction northward of the section.

This study was carried out in the framework of the German-Canadian international research training group *ArcTrain*, funded by the German Research Foundation (DFG).

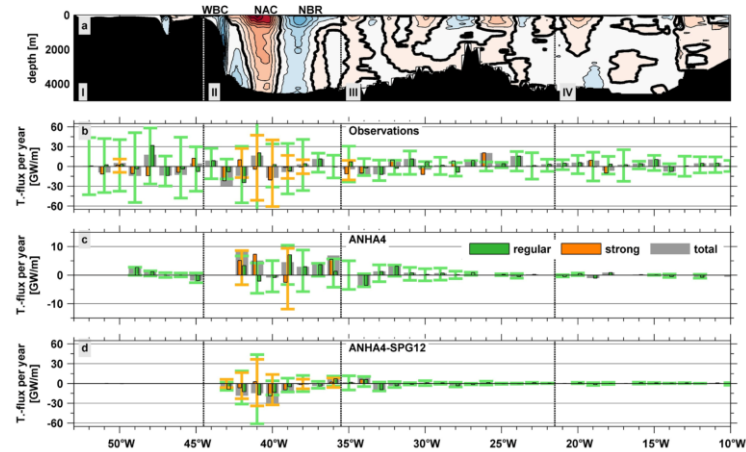


Figure 72: (a) Meridional background velocity from the observations and the (b) sum of the temperature flux by eddies per 1° bin along 47°N (normalized by the number of years) in the observations (January 1993 to April 2014), (c) 1/4° ANHA4 simulation (2002 to 2013), and (d) 1/12° ANHA4-SPG12 simulation (2002 to 2013). The net flux (grey) is separated into fluxes carried by regular (green) and by strong (orange) eddies. Vertical bars show the sum of the temperature flux by eddies of regular (green) and strong (orange) eddies in either direction. The vertical whiskers represent the standard deviation of the respective flux in either direction. NAC: North Atlantic Current; NBR: Newfoundland Basin Recirculation.

References:

- Müller, V., D. Kieke, P. G. Myers, C. Pennelly, and C. Mertens: Temperature flux carried by individual eddies across 47°N in the Atlantic Ocean, *J. Geophys. Res.*, 122, 2441-2464, doi:10.1002/2016JC012175, 2017.
- Nencioli, F., C. Dong, T. Dickey, L. Washburn, and J. C. McWilliams: A vector geometry-based eddy detection algorithm and its application to a high-resolution numerical model product and high-frequency radar surface velocities in the Southern California Bight, *J. Atmos. Oceanic Technol.*, 27(3), 564–579, doi:10.1175/2009JTECHO725.1, 2010.

Sources and fate of man-made radionuclides in the tropical western Pacific Ocean

Daniela Pittauer and Helmut W. Fischer

Radioactivity of the northwest Pacific Ocean moved to the centre of great public and scientific attention after the accidental releases from the Japanese nuclear power plant Fukushima Daiichi in the aftermath of the catastrophic Tohoku earthquake and tsunami in March 2011. Less public interest is paid to the radioactive legacy connected with nuclear weapons testing that took place during 1940's and 1950's at remote atolls Bikini (Figure 73) and Enewetak in the tropical northern Pacific, which until these days continues having high regional impact in the Pacific Ocean environment.

At the IUP Bremen, we studied plutonium isotopes in sediments from the Pacific Ocean floor in cooperation with MARUM at University of Bremen, Alfred Wegener Institute in Bremerhaven and international partners from Australian

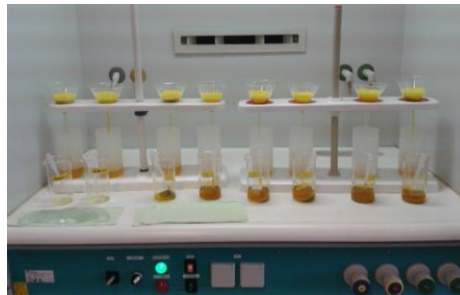


Figure 74: Chemical separation of plutonium from sediment is time consuming: for a single batch of samples it takes several days and requires dozens of steps.)

National University in Canberra and Technical University of Denmark in Roskilde. The sediment cores were sampled during sea-going expeditions on the German research vessel "Sonne".

We took samples from the upper sediment layers,

covering approximately the last century of sediment deposition in special areas with high sedimentation accumulation rate due to rich nutrients supply and high biological productivity. The studied sites were located along the pathway of major ocean currents thousands of kilometres downstream the nuclear test sites, in the Philippine Sea east of Mindanao and in the Lombok Basin near Indonesian island of Sumba, where Pacific water enters the Indian Ocean. Another sediment core was collected in Bismarck Sea, off Papua New Guinea (Figure 75). We investigated plutonium isotopes by a combination of radiochemical (Figure 74), radiometric and mass spectrometric techniques, which allow to distinguish different sources of radioactive materials based on their isotopic fingerprints.

By comparison of observed plutonium composition over the past decades with known sources, we inferred that the portion of plutonium originating from the Pacific test sites in Philippine Sea and Lombok Basin was as high as 60% until these days. The rest is attributed to the global stratospheric

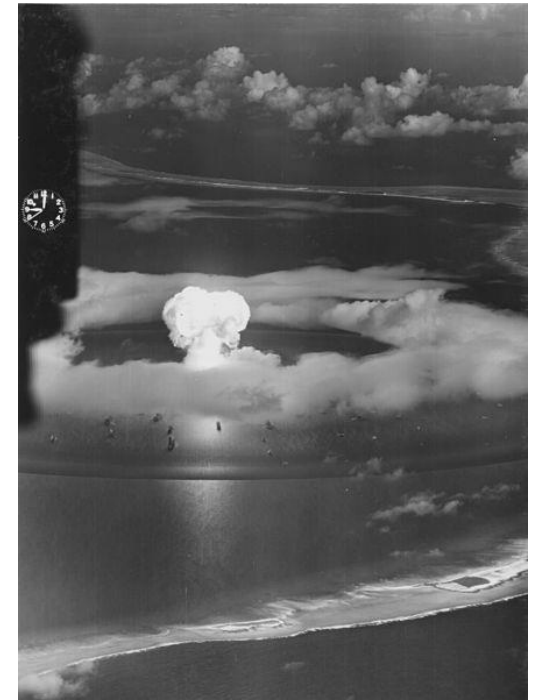


Figure 73: Mushroom cloud during the first nuclear weapons test on Bikini Atoll on July 1946, operation Crossroads, ABE. (Credit: United States Army Air Forces)

fallout from the 1960's high yield atmospheric nuclear tests. In Lombok Basin core our research newly documents the ongoing transport of Pacific-derived plutonium towards the Indian Ocean.

In Bismarck Sea, in contrary, plutonium fingerprint points to the global fallout origin. At this site, we additionally registered a contribution of another plutonium source, radionuclide thermoelectric generator from the SNAP-9A satellite that burnt up in the atmosphere in 1964. This contribution is much more prominent in the southern hemisphere. However, a small portion of plutonium in the Bismarck Sea can be also attributed to the Bikini and Enewetak tests, and this north Pacific contribution appears simultaneously with decreased contribution from the typically south Pacific-derived SNAP-9A plutonium.

Plutonium, although being particle reactive, is not deposited to sediment immediately, but due to lack of particles in the open ocean stays in deeper ocean layers and is gradually removed by settling particles mainly along the continental margin.

References

D. Pittauer, S. Tims, P. Roos, M. Froelich, J. Qiao, H.W. Fischer: Pacific Proving grounds radioisotope imprint in sediments from equatorial Western Pacific and Indonesian throughflow, In: B. R. Persson, E. Holm, R. Garcia-Tenorio, G. Manjón (Eds). II International Conference on Radioecological Concentration Processes (50

years later), 2016.

http://portal.research.lu.se/portal/files/31656693/Libro_Final_version_con_ISBN.pdf

D. Pittauer, S.G. Tims, M.B. Froehlich, L.K. Fifield, A. Wallner, S.D. McNeil, H.W. Fischer: Continuous transport of Pacific-derived anthropogenic radionuclides towards the Indian Ocean, Scientific Reports 7, 44679, DOI: 10.1038/srep44679, 2017.

D. Pittauer, P. Roos, J. Qiao, W. Geibert, M. Elvert, H. W. Fischer: Pacific Proving Grounds radioisotope imprint in the Philippine Sea sediments. Journal of Environmental Radioactivity, 186, 131-141, DOI: 10.1016/j.jenvrad.2017.06.021, 2018.

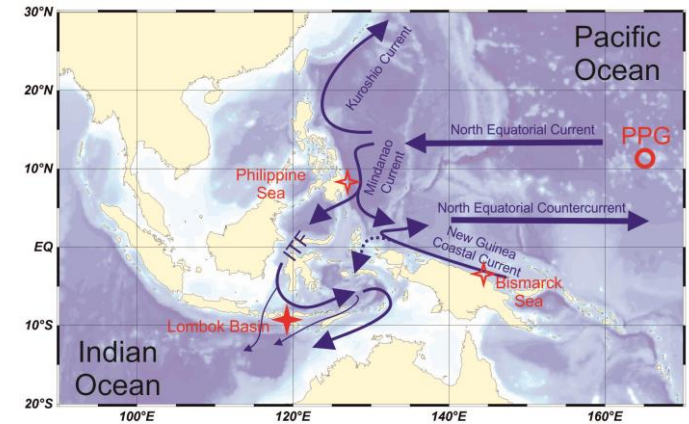


Figure 75: Location of sediment cores investigated for traces of plutonium: Philippine Sea, Lombok Basin and Bismarck Sea. The 1940's-1950's nuclear tests were conducted at Bikini and Enewetak atolls, marked as PPG.

Search for the origin of atmospheric radioactive iodine in 2017

Helmut W. Fischer

Early in 2017, members of the informal “Ring of Five” (Ro5) network of state laboratories for atmospheric radioactivity informed their respective authorities and each other about almost simultaneous detections of the radioactive isotope of iodine ^{131}I in many European countries (Figure 76). ^{131}I is known as major component of nuclear weapons fallout and nuclear power plant (NPP) accident emissions and is responsible for excess children’s thyroid cancer in Belarus from Chernobyl NPP emissions. It could be detected in regional cow’s milk by IUP Bremen in April 2011, originating from Fukushima NPP (Pit-tauerová et al., 2011). The 2017 findings created considerable public and media interest. Luckily, concentrations were very low, so no health hazard was involved. No source event or location could be identified to date.

^{131}I is also used as therapeutic agent for thyroid diseases in nuclear medicine, and can therefore be found in hospital wastewater and sewerage from homes of patients treated with ^{131}I , after their release from the hospital. At IUP Bremen, ^{131}I from medical origin is detected in wastewater and sewage sludge on a regular basis, and the continuous small ^{131}I releases from a local sewage plant have been used to study river and sediment transport processes (Souti, 2018). ^{131}I therapy is a rather common procedure with, for example, ca. 50,000 yearly applications of up to 5 Gigabecquerel (1 GBq = 10^9 Bq) per patient in Germany. Factories for radiopharmaceuticals produce the required large quantities of ^{131}I in specialized nuclear reactors. Factories exist in western and eastern Europe.

In a joint effort, members of more than 20 Ro5 laboratories attempted to identify the geographical origin of the emissions and the possible releasing event or process (Masson et al., 2018). They combined their

pool of measured data with modelling of atmospheric transport and chemistry and comparison of possible emission sources, scenarios and source strengths. Additional data from the network of CTBTO (www.ctbto.org) atmospheric radioactivity stations (operating for the detection of nuclear weapon tests) could be used.

First concerns about nuclear weapon test fallout or nuclear power plant emissions could be ruled out easily, as no other isotopes, which should in such cases accompany ^{131}I , could be detected. Therefore, only technical (NPP routine releases, isotope production), medical or natural (from spontaneous fission of ^{238}U in soils) origin was plausible.

IUP’s contribution consisted in the numerical evaluation of the effect of incineration of sewage sludge containing ^{131}I , based on its experience with this isotope in medical application and environmental monitoring. A mean ^{131}I concentration in sewage sludge from routine monitoring was combined with data on incinerated amounts per year, and a homogeneous distribution within the atmospheric boundary layer was assumed. The effective atmospheric lifetime of ^{131}I could be deduced from 2011 Fukushima data (BfS, 2011). The resulting atmospheric concentration just reached the detection threshold of the most sensitive

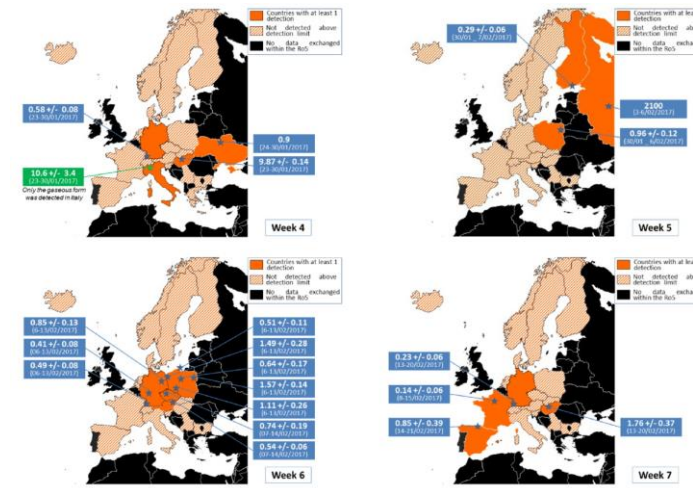


Figure 76: Detections of ^{131}I in Europe during four weeks in early 2017 (Masson et al., 2018)

instruments contributing data to this study, so a significant contribution of this emission pathway to the encountered data could be ruled out (Figure 77). However, the process was identified as possible source of regional concentration peaks during meteorological conditions impeding fast dilution.

Other processes included spontaneous fission of natural ^{238}U , routine emissions from NPP, routine emissions from radiopharmaceutical production facilities (within the range of the respective authorized values) and accident releases from such factories (as encountered several times in the past).

From these, also ^{238}U fission and NPP routine emissions gave far too low possible air concentrations (Figure 77). So, routine and accidental releases from isotope production sites remained as possible origin.

Atmospheric transport modelling performed at IRSN/France pointed towards a source in western Russia, where a radiopharmaceutical factory is operating at Obninsk (Figure 78). An emission of 70 GBq would explain most of the detections and would fall within the author-

ized release levels of this plant. However, several clear detections in Western Europe could only be explained by a second, minor emission from another, smaller and unknown source.

Whilst (fortunately) not dealing with harmful concentrations, the event demonstrated the capabilities of the Ro5 network to, in a collective effort, identify an unknown source of radioisotopes in terms of location, time and magnitude of the release – a situation similar to what would be encountered in case of a major emission of radioactive material.

References

- D. Pittauerová et al., Fukushima fallout in Northwest German environmental media, *J. Environ. Radioact.* 102 (2011) 877-880, doi:10.1016/j.jenvrad.2011.06.003
- M.E. Souti, Natural and artificial radionuclides as tracers in fluvial systems, Ph.D. Thesis, IUP Bremen 2018
- O. Masson et al., Potential Source Apportionment and Meteorological Conditions Involved in Airborne ^{131}I Detections in January/February 2017 in Europe, *Environ. Sci. Technol.* 52 (2018) 8488-8500, DOI:10.1021/acs.est.8b01810
- Federal Office of Radiation Protection (BfS): Report on atmospheric radioisotope trace measurements in Germany following the Fukushima accident, 2011. (<http://www.bfs.de/SharedDocs/Bilder/BfS/DE/ion/umwelt/fukushima-spurenmessstellen-jod.jpg>)

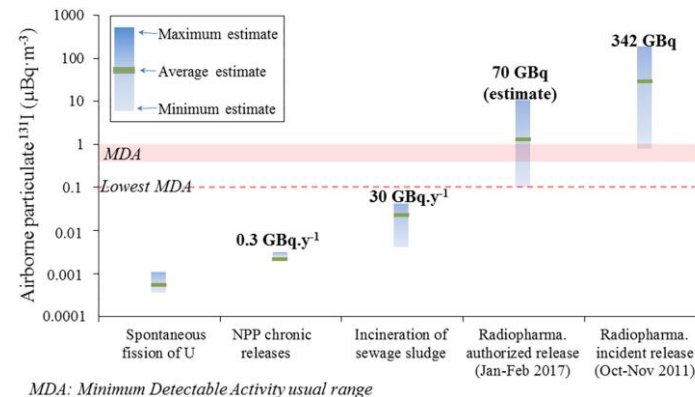


Figure 77: Possible ^{131}I mean atmospheric concentrations from different sources (Masson et al., 2018)

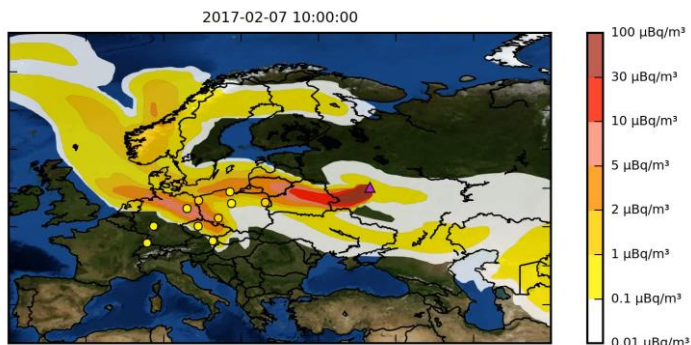


Figure 78: Map of Europe with modeled ^{131}I distribution (coloured area) for an emission from Western Russia (triangle), and ^{131}I detections (dots) at that time (3). The whole movie, covering 8 weeks, can be downloaded here: https://pubs.acs.org/doi/suppl/10.1021/acs.est.8b01810/suppl_file/es8b01810_si_001.avi

Teaching activities

Annette Ladstätter-Weißmayer, Harry Küllmann and Anja Gatzka

Today's graduate and postgraduate education in the field of Earth System and Environmental Science is a highly interdisciplinary and inter-institutional challenge. The existing research infrastructure at the University of Bremen (UB) and the Alfred Wegener Institute, Helmholtz Centre for Polar and Marine Research, Bremerhaven (AWI) offers a unique research environment in north-western Germany to study past, present and future changes of the Earth system. The education and qualification of Master and PhD students is carried out on an internationally competitive level.

Since 2000, the international Master program "Postgraduate Program Environmental Physics" (PEP) accredited by the German Accreditation Council is running in collaboration with the AWI, Bremerhaven. Since its start, 119 students successfully finished this program with a Master degree, 14 with a Certificate. The foci of this program are on the atmosphere, ocean, land and climate as well as on remote sensing and dynamics.

In the winter semesters 2017/18 until 2018/19, 46 students started this study-program at the University of Bremen. The students came from Bangladesh, Brazil, China, Colombia, Egypt, Gambia, Germany, Georgia, Ghana, India, Iran, Italy, Mexico, Morocco, Nepal, Nigeria, Pakistan, South Korea and Spain.

In 2006 a very successful collaboration between the University of Bremen and the Ocean University of China (OUC) in Qingdao/China started with the aim to offer Master double degrees of both universities. In this program, Chinese students start their studies in China, participate one year in the PEP program in Bremen and then complete their studies at

the OUC. The German students start with one year of the PEP program and then study one year at the OUC in Qingdao.

In addition to this number of students, 1 ERASMUS student from UK and 23 so called Wahlfachstudenten from Physics, 14 from Space Sciences and Technologies, and 10 from Space Engineering are participating every year in the PEP program.

In the last 18 years, 56% from our students started - after finalising their master program or their Certificate - their PhD studies at the Institute of Environmental Physics in Bremen or the AWI in Bremerhaven or somewhere else, whereas the remaining 44% applied directly for a job in industry or in climate or weather forecast related agencies.

As Bremen is one of the most important locations for aerospace in Germany, colleagues from IUP and AWI together with colleagues from the departments of Electrical Engineering, Mathematics and Production Engineering from the University of Bremen set up a curriculum for an international master program in Space Sciences and Technologies which started in winter 2017/18. 14 Students from India, Pakistan, Spain, Morocco, Russia, Federation UK, Egypt, China, Turkey and Germany came to the University of Bremen to study Space Sciences and Technologies – Sensing, Processing and Communication to get trained in experimental methods towards space applications, numerical data analysis and interpretation via sophisticated models.

In 2006 in the context of the excellence initiative the Bremen International Graduate School for Marine Sciences

GLOMAR was launched and funded by the Deutsche Forschungsgemeinschaft (DFG). This Graduate School is carried out with the following partners: University of Bremen, DFG Research Center Ocean Margin (RCOM), Center for Marine Environmental Science (MARUM), Research Center for Sustainability Studies (ARTEC), AWI, German Maritime Museum (DMS), Max Planck Institute for Marine Microbiology, Center for Tropical Marine Ecology (ZMT). For excellent PhD students GLOMAR provides an optimal student research environment and fosters excellence in education and research. In general the Graduate School's educational concept allows the PhD students to develop into excellent interdisciplinary researchers, with international contacts and a publication record in peer-reviewed international journals, skills in conducting research and in communication (on disciplinary and interdisciplinary levels to both experts and students as well as to the public), and in project management.

In 2009 the Helmholtz Graduate School POLMAR (Polar and Marine Research) started with the following partners: AWI (host institution), University of Bremen, Jacobs University Bremen, Max Planck Institute Bremen, University of Potsdam, Institute for Marine Resources (IMARE), and Hochschule Bremerhaven.

These programs enable PhD students from a variety of disciplines to cooperate and exchange views on the common theme of linking 'data and modelling', leading to a better understanding of local processes within a global context. It provides a structured framework for education and qualifi-

cation for excellent PhD students dealing with the challenging questions in Earth System Science and Polar and Marine Research. Developing all categories of skills needed for analysing complex climate and environmental systems and the development of integrated solutions in a supportive network of collaborating research institutions fosters outstanding career options. Structured training and supervision supported by a broad range of soft skill courses is indicative for the entire concept. Up to now more than 100 PhD students are within POLMAR.

The international German-Canadian graduate program ArcTrain "Processes and impacts of climate change in the North Atlantic Ocean and the Canadian Arctic", which has been funded since 2013, is a project led by scientists from the IUP (G. Spreen, M. Rhein, M. Walter (co-speaker), D. Kieke), MARUM, the AWI and colleagues from 8 Canadian institutes. In 2017, the program was successfully evaluated by the DFG and funding was assured until 2022. In 2017/18, the first cohort of 13 PhD students graduated successfully.

The IUP Bremen regularly welcomes students from high schools in Bremen carrying out practical exercises. During these internships, the students have the opportunity to work in different research groups together with scientists for a time period of 2 weeks to get a first impression of research work.

In addition the members of IUP are very active and involved in the "Day of Physics" and "Advents Physics" to give an overview about scientific work at IUP.



IUP Bremen Staff, December 2018

Visit us on http://www.iup.uni-bremen.de/index_e.html

©Institute of Environmental Physics, University of Bremen, December 2018. Edited by Andreas Richter